Max-Planck-Institut
für Meteorologie

MAX-PLANCK-GESELLSCHAFT

International Max Planck Research School
on Earth System Modelling

Warming up the atmosphere's heat engine: atmospheric energetics with higher greenhouse gas concentrations

Daniel Hernández Deckers

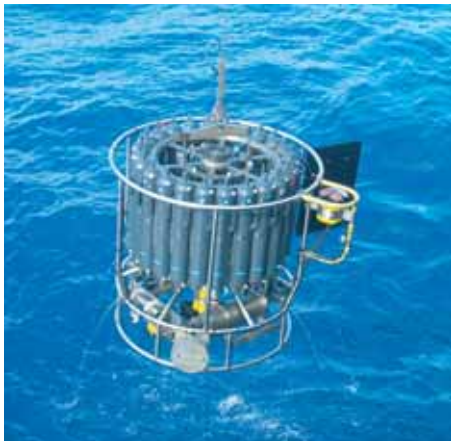

Berichte zur Erdsystemforschung 85/2011

Reports on Earth System Science

Hinweis

Die Berichte zur Erdsystemforschung werden vom Max-Planck-Institut für Meteorologie in Hamburg in unregelmäßiger Abfolge herausgegeben.

Sie enthalten wissenschaftliche und technische Beiträge, inklusive Dissertationen.

Die Beiträge geben nicht notwendigerweise die Auffassung des Instituts wieder.

Die "Berichte zur Erdsystemforschung" führen die vorherigen Reihen "Reports" und "Examensarbeiten" weiter.

Notice

The Reports on Earth System Science are published by the Max Planck Institute for Meteorology in Hamburg. They appear in irregular intervals.

They contain scientific and technical contributions, including Ph. D. theses.

The Reports do not necessarily reflect the opinion of the Institute.

The "Reports on Earth System Science" continue the former "Reports" and "Examensarbeiten" of the Max Planck Institute.

Anschrift / Address

Max-Planck-Institut für Meteorologie
Bundesstrasse 53
20146 Hamburg
Deutschland

Tel.: +49-(0)40-4 11 73-0
Fax: +49-(0)40-4 11 73-298
Web: www.mpimet.mpg.de

Layout:

Bettina Diallo, PR & Grafik

Titelfotos:
vorne:
Christian Klepp - Jochem Marotzke - Christian Klepp
hinten:
Clotilde Dubois - Christian Klepp - Katsumasa Tanaka

Berichte zur Erdsystemforschung 85/2011

Warming up the atmosphere's heat engine: atmospheric energetics with higher greenhouse gas concentrations

Daniel Hernández Deckers

aus Bogotá, Colombia

Hamburg 2010

Reports on Earth System Science 85/2011

ISSN 1614-1199

Daniel Hernández Deckers
Max-Planck-Institut für Meteorologie
Bundesstrasse 53
20146 Hamburg
Germany

Als Dissertation angenommen
vom Department Geowissenschaften der Universität Hamburg

auf Grund der Gutachten von
Prof. Dr. Jochem Marotzke
und
Dr. Jin-Song von Storch

Hamburg, den 10. Dezember 2010
Prof. Dr. Jürgen Oßenbrügge
Leiter des Departments für Geowissenschaften

ISSN 1614-1199

Warming up the atmosphere's heat engine: atmospheric energetics with higher greenhouse gas concentrations

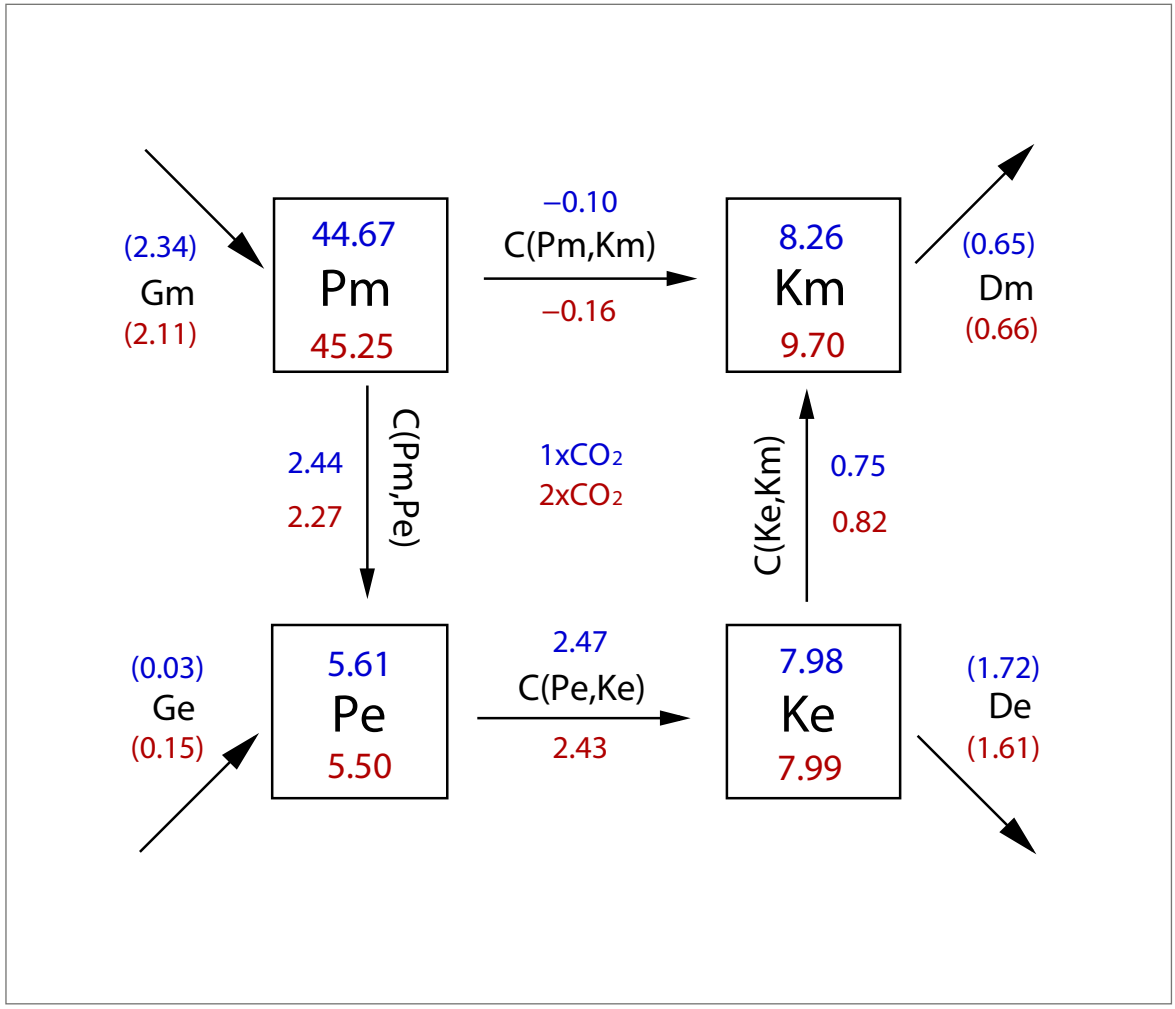

Daniel Hernández Deckers

Hamburg 2010

Abstract

Although an increase in greenhouse gas concentrations warms the troposphere, it is unclear if this changes the atmospheric energetics, i.e., the generation of available potential energy, its conversion into kinetic energy, and its further dissipation. The Lorenz Energy Cycle describes these energy processes and concisely summarizes the atmosphere's behavior as a heat engine from which other properties may be inferred. In order to study the response of the atmospheric energetics to an increase in greenhouse gas concentrations, we evaluate changes in the Lorenz Energy Cycle due to increased atmospheric CO_2 in the coupled atmosphere-ocean ECHAM5/MPI-OM model.

Globally, doubling of CO_2 results in a 4% to 7% weakening of the Lorenz Energy Cycle, since less available potential energy is converted into kinetic energy per unit of time, indicating a reduction in energetic activity. This global weakening is the result of two opposite responses: a strengthening in the upper troposphere and a weakening in the lower and middle troposphere. The latter dominates the globally-integrated response. These two responses result from the simulated $2xCO_2$ warming pattern that consists of a strong warming in the tropical upper-troposphere and in the high-latitudes near the surface. By performing additional experiments in which these two features of the $2xCO_2$ warming pattern are simulated separately, we find that the strengthening (a 4% increase) of the energetic activity is a consequence of the high-latitude surface warming, whereas the weakening (a 10% decrease) is a consequence of the tropical upper-tropospheric warming. Furthermore, both responses are accompanied by corresponding changes in baroclinicity—the main process responsible for the conversion of available potential energy into kinetic energy—as well as in extratropical storm activity, as measured by the global reservoir of eddy kinetic energy.

We show that the dominant aspect of the warming pattern that alters the global atmospheric energetics is not its horizontal temperature distribution but its mean static stability. This stands in contrast to the expectations based on Held (1993), which consider only effects of changes in the horizontal temperature distribution. We expand these expectations by pointing out that changes in the temperature stratification are more important. The response of static stability is the driving mechanism for changes in the atmospheric energetics, as well as in baroclinic activity from a global point of view. This means that the tropical upper-tropospheric warming, which increases mean static stability, causes a weakening in the energetic activity, whereas the high-latitude surface warming, which decreases mean static stability, causes a strengthening in the energetic activity. The combined response to a CO_2 doubling is dominated by the tropical upper-tropospheric warming effect, which explains the overall weakening in energetic activity. In terms of the reservoir of eddy kinetic energy, the two opposite responses—6% decrease due to the tropical upper-tropospheric warming and 5% increase due to the high-latitude surface warming—nearly cancel each other in the $2xCO_2$ case. This may explain the current lack of consensus regarding global changes in extratropical storm activity in a warmer climate.

Contents

Chapter 1

Introduction

1.1 Motivation and research questions

From a global thermodynamic point of view, the earth's atmosphere can be considered as a heat engine that converts part of the incoming solar radiation into kinetic energy. By doing so, it maintains the global circulation of the atmosphere against frictional dissipation. Based on this simple but fundamental approach, Lorenz (1955) developed a global energy cycle, currently known as the *Lorenz Energy Cycle*. It describes how available potential energy is generated due to differential heating, converted into kinetic energy by the rising of relatively warm air and sinking of relatively cold air, and further dissipated by friction. Here we use this Lorenz Energy Cycle to describe the *energetics of the atmosphere*, i.e., the operation of the atmosphere as a heat engine.

The Lorenz Energy Cycle is based on the concept of *available potential energy*. This quantity measures the fraction of the total potential energy that is actually available for conversion into kinetic energy. Lorenz (1955) derives an approximate formula for available potential energy that expresses it as the variance of temperature on constant pressure surfaces divided by the mean static stability. This formula, from which a complete set of equations describing the different terms of the Lorenz Energy Cycle can be derived, provides a good insight into the physical properties of the available potential energy, and is convenient for computations. It shows that available potential energy depends on the horizontal and vertical distribution of temperature: the larger the horizontal temperature differences and the weaker the static stability, the larger the amount of available potential energy.

The most prominent horizontal temperature difference in the earth's atmosphere is between the poles and the equator. This is illustrated by Figure 1.1, which shows the mean pre-industrial surface temperature simulated by a coupled atmosphere-ocean general circulation model. Although temperature differences induced by topography and land-sea contrasts are also important, globally the most prominent pattern in the horizontal temperature distribution is this pole to equator contrast. This feature results from the net heating at low latitudes and the net cooling at high latitudes—the largest contribution to the generation of available potential energy—and constitutes the main energy source for the atmosphere's heat engine (Lorenz, 1955, 1967; Peixoto and Oort, 1974, 1992). In particular, this temperature difference is the driver for baro-

clinic disturbances, which is the main process behind the conversion of available potential energy into kinetic energy (e.g., Peixoto and Oort, 1992; Holton, 2004).

On the other hand, the vertical distribution of temperature in the atmosphere determines static stability. Static stability is important for available potential energy because it determines how prone the atmosphere is for vertical movements. Available potential energy can only be converted into kinetic energy through vertical movements with or against the force of gravity (Lorenz, 1967). Hence, in a very stable atmosphere—in which vertical movements are suppressed—available potential energy looses its ”availability” because it cannot be converted into kinetic energy.

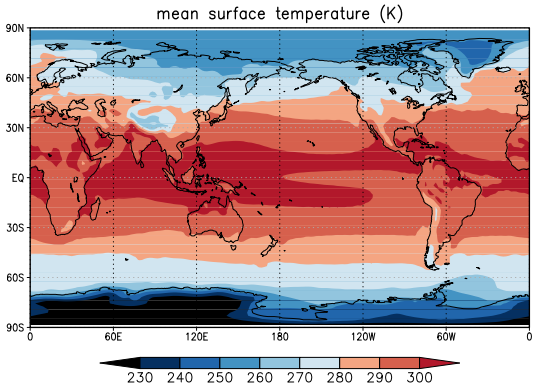

Figure 1.1: Mean surface temperature (in K) obtained from a 50-year average of a coupled atmosphere-ocean ECHAM5/MPI-OM model run with pre-industrial conditions (experiment CTRL used in Chapter 3).

In thermodynamics, the conceptual heat engine consists of a warm thermal bath from which the engine extracts heat, and a cold thermal bath to which it dumps the excess of heat after having performed work. The larger the temperature difference, the larger the efficiency of the engine, i.e., more work is done with the same amount of heat extracted per unit of time. Making a simple analogy with the climate system, one could associate the warm and cold thermal baths with the low and high latitude regions, and the performed work with the conversion of available potential energy into kinetic energy that takes place as heat is transferred from the low to the high latitudes. Of course, the complexity of the atmosphere is such that this analogy is too simple to describe the atmosphere’s behavior realistically. However, with some additional considerations, such an analogy can be carried out rigorously, and one can formally define an efficiency for the climate system (Lucarini, 2009). Although our study does not go in that direction, the idea of visualizing the atmosphere as a heat engine illustrates the fundamental nature of the energetics of the atmosphere, and in particular of the Lorenz Energy Cycle.

Initially, the Lorenz Energy Cycle was used to obtain an estimate of the energetics of the atmosphere based on the available observations. The objective was to understand and quantify the amount of energy and the rate at which it is generated, converted, and dissipated in the atmosphere. The most representative study was carried out by Peixoto and Oort (1974) and Oort and Peixoto (1974), whose results are still cited in widely used textbooks (e.g., Peixoto and Oort, 1992; Holton, 2004). With a relatively sparse observation data set they were able to characterize the main features of the energetics of the atmosphere, so that still today their results are of great value from an understanding point of view. Using better sets of observations and reanalysis data, recent studies have quantified more precisely the energetics of the atmosphere (e.g., Li et al., 2007; Boer and Lambert, 2008). This has proven to be useful in order to evaluate and compare different reanalysis data sets, and also different atmospheric

models among themselves and with observations. Furthermore, recent studies on current or future changes in storm activity use the Lorenz Energy Cycle (Boer, 1995) or specific elements from it (O'Gorman and Schneider, 2008; Wu et al., 2010) as a fundamental tool.

In this thesis we want to investigate, using the Lorenz Energy Cycle, how the energetics of the atmosphere respond when we "warm up" the atmosphere's heat engine. It is clear that higher CO_2 concentrations warm the troposphere, but it is not clear how this may affect the energetics of the atmosphere. For example, if the atmosphere warms up homogeneously, available potential energy should not change, so that probably the whole energetics would as well remain unchanged. However, the expected warming is far from being homogeneous (Meehl et al., 2007) so that changes in available potential energy and in the whole atmospheric energetics would in principle be expected. This brings us to our first research question:

1. *What is the response of the atmospheric energetics to higher CO_2 concentrations?*

We are not only interested in finding out what is the atmospheric energetics response, but also in understanding it. This leads to our second research question:

2. *What are the mechanisms that cause the atmospheric energetics response to higher CO_2 concentrations?*

Although we will study changes in all the components of the Lorenz Energy Cycle, i.e., reservoirs of energy and energy conversion rates, we are most interested in changes in the energy conversion rates. These measure the *energetic activity* of the atmosphere, i.e., the rate at which the atmosphere performs work by converting available potential energy into kinetic energy. In particular, we want to know if the energetic activity strengthens or weakens in a warmer climate. A strengthening would imply a higher rate of conversion of available potential energy into kinetic energy, which would suggest more baroclinic activity, and probably more (or stronger) extratropical storms. A weakening would indicate the opposite response.

Previous studies are related to our research questions. Boer (1995) studied the changes in the Lorenz Energy Cycle in the Northern Hemisphere winter season due to doubling of CO_2 concentrations. He found a reduction in energetic activity, while the reservoir of kinetic energy remained unchanged. He attributed this to the reduced pole-to-equator temperature difference and land-sea contrasts during winter. Using an atmospheric model with specified sea surface temperatures and a local formulation of the energy cycle, Marquet (2005, 2006) also focuses on the Northern Hemisphere winter. He obtains a similar weakening in the energetic activity, but with an additional local strengthening in the upper troposphere. In contrast to these studies, we use here a fully coupled atmosphere-ocean general circulation model (ECHAM5/MPI-OM), and we consider the global, annual mean response of the energetics. Instead of using the Lorenz Energy Cycle to study changes in the energetics of specific regions of the globe, we use it to study the global energetics response, and by doing so, we expect to achieve a better understanding of the dynamical response of the global atmosphere to higher CO_2 concentrations.

On the other hand, if the global response to higher CO_2 concentrations is a weakening in the energetic activity (Boer, 1995; Marquet, 2005, 2006), one would expect that extratropical storms should also decrease. Recent studies about extratropical storm activity do not offer yet a conclusive statement in this matter. With one atmospheric model, Geng and Sugi (2003) found that the total frequency of extratropical storms decreases, but the frequency of strong storms increases. Yin (2005) found a strengthening and poleward shift of the storm tracks in several climate models, suggesting an intensification of extratropical storms. Bengtsson et al. (2009), using a high-resolution atmospheric model, found a small reduction in the number of storms, but no significant changes in the extremes of wind and vorticity. O'Gorman and Schneider (2008) pointed out an important connection that further motivates our study: they found that eddy kinetic energy scales approximately with available potential energy. This suggests that we can expect that by studying the energetics response, we can obtain some fundamental information about the response of extratropical storms, even without studying extratropical storms in detail. At least, we may be able to understand why other detailed studies have not yet succeeded in obtaining a consensus about the response of extratropical storms to a warmer climate.

1.2 Outline of the thesis

Including this introductory chapter, this thesis comprises 4 chapters and 4 appendixes. Chapters 2 and 3 bring together the main results. The first section of Chapter 2 has already been published in the *Journal of Climate* (Hernández-Deckers and von Storch, 2010).

In Chapter 2 we answer our first research question. There we describe the response of the Lorenz Energy Cycle in several coupled model experiments. We do this with transient experiments in which CO_2 concentrations increase with time, as well as with experiments in which CO_2 is doubled and held constant for a long period of time. The $2xCO_2$ experiments are analysed with two different resolutions of the model.

In Chapter 3 we study the $2xCO_2$ response of the Lorenz Energy Cycle by carrying out experiments in which, instead of changing the CO_2 concentrations, we artificially force the model towards two different warming patterns. These patterns reflect the two main features of the $2xCO_2$ warming pattern. With these experiments we are able to isolate and track specific energetic responses of the $2xCO_2$ case, making it possible to understand the mechanisms behind these responses. Therefore, in this chapter we answer our second research question.

Appendixes A and B present the equations that describe the Lorenz Energy Cycle, which we have used for the different computations. Appendix C presents a short discussion about the quality of one of the $2xCO_2$ experiments in terms of its equilibrium conditions, and Appendix D contains figures that constitute supplementary material for Section 3.3.2.

Finally, chapter 4 presents the main conclusions and the outlook of this thesis.

Chapter 2

Energetics responses to increases in greenhouse gas concentrations

2.1 Responses obtained with the low resolution ECHAM5/MPI-OM coupled model*

2.1.1 Introduction

The study of the energetics of the atmosphere provides a fundamental approach to the understanding of the dynamics of the atmosphere. Here we use it to investigate the dynamical responses of the atmosphere to higher greenhouse gas concentrations simulated by an ocean-atmosphere coupled GCM.

It is clear that higher greenhouse gas concentrations imply an increase in global mean temperature, but it is not clear how this may affect the energetics of the atmosphere. One way of addressing this problem is through the Lorenz Energy Cycle (LEC) (Lorenz, 1955), which deals with the maintenance of the circulation in terms of the generation (G) of available potential energy (P), its conversion into kinetic energy (K), and its further frictional dissipation (D), derived using the usual Eulerian mean decomposition. Here, P depends on the spatial variance of temperature over constant pressure levels, and on γ, the inverse mean static stability. Hence, P is not affected by a homogeneous temperature increase, but by changes in horizontal or vertical temperature gradients. These could trigger changes in the whole LEC. Diagnosing these changes can provide us with fundamental clues for understanding the dynamical changes in the circulation of the atmosphere of a warmer planet.

In principle, the LEC provides a global view of the dynamics of the atmosphere from an energetic point of view. However, the decomposition of the P and K reservoirs into zonal-mean and eddy components reveals also certain relationships of the LEC-terms with specific processes. One should not pretend to obtain a complete and detailed description of these processes through the LEC, but in order to gain some understanding of the mechanisms behind the energetics of the atmosphere, it is useful to have them in mind. To begin with, zonal mean available potential energy (P_m) is generated due to net heating at low latitudes and net cooling at

* The content of this section has been published in the Journal of Climate (Hernández-Deckers and von Storch, 2010).

high latitudes (heating of warm regions and cooling of cold regions). The conversion from P_m into eddy available potential energy (P_e) and then into eddy kinetic energy (K_e) results from baroclinic instability. It is related to the meridional heat transport by the eddies. The conversion between K_e and zonal-mean kinetic energy (K_m) is related to wave-mean flow interactions. On the other hand, the direct conversion between P_m and K_m is related to the zonal-mean meridional overturnings. This involves processes like the Hadley cell, where mostly P_m is converted into K_m, but also the indirect Ferrel cells, where mostly K_m is converted into P_m. The net result of this conversion term turns out to be quite small compared to the conversions following the path $P_m \rightarrow P_e \rightarrow K_e \rightarrow K_m$. The latter is therefore considered to be the main path for the generation of K in the atmosphere, which implies that the eddies play a crucial role in the energetics (Peixoto and Oort, 1992).

Changes in energetics due to CO_2-doubling have been studied by Boer (1995). He focused on the Northern Hemisphere winter season, using output from an atmospheric GCM coupled to an interactive "slab" ocean. His results for a 2xCO_2 simulation show a reduction in strength of the LEC (measured by the total conversion from P to K), consistent with reduced equator to pole temperature gradients and land-sea contrasts during winter. The kinetic energy is found to remain unchanged. Although the winter season is when the LEC shows its strongest activity due to the larger equator to pole and land-sea temperature contrasts, here we consider the global and annual-mean conditions simulated by a coupled atmosphere-ocean GCM in order to capture the responses of both hemispheres and to have a complete view of the energetic changes due to higher CO_2 concentrations.

The next subsection describes the model we use, the analyzed experiments, the LEC equations, and their computational procedure. The third subsection presents our results, followed by the conclusions and discussion subsection. A full description of the expressions used for the computation of the different terms is presented in Appendix A.

2.1.2 Method

Model and experiments

We use integrations of the coupled ECHAM5/MPI - OM atmosphere-ocean sea-ice general circulation model developed at the MPI for Meteorology in Hamburg. The atmosphere component (ECHAM5) is described by Roeckner et al. (2003) and the ocean/sea-ice component (MPI-OM) by Marsland et al. (2003). The coupling is done without flux adjustments. We use a low resolution version (T31, $\approx 3.8^0 \times 3.8^0$, with 19 vertical levels for the atmosphere, and $\approx 3^0 \times 3^0$ with 40 vertical levels for the ocean), and daily mean outputs for the computations. Jungclaus et al. (2006) describe a higher resolution version of this coupled model, which was used to perform the scenario runs for the IPCC fourth assessment report.

As a reference climate we use a 100 year control run with a 1×CO_2 concentration of 280 ppm. In order to analyze the transient response, we consider two 50-member ensembles of climate change runs starting from different years of the control run: one from the even years

and the second from the odd years of the control run. The forcing of each run is a 3% increase in CO_2 concentration per year, and each run is 10 years long, leading to a final CO_2 factor of 1.34. A detailed description of these integrations is given by von Storch (2008). The transient ensemble is used to qualitatively assess the way of approaching the equilibrium changes. We are not aiming at a description of realistic changes that have happened in the past. For the latter purpose, one needs a sufficiently big ensemble of realistic simulations of the past climate, which was not available for the present study. For the stationary response we use the last 100 years of a stabilized $2\times CO_2$ run from Seiffert and von Storch (2008), performed with the same coupled model.

Lorenz Energy Cycle equations

The basic equations for the two-component LEC, integrated over a volume, are:

$$\begin{aligned} \frac{dP}{dt} &= -C(P,K) + G + B(P) \\ \frac{dK}{dt} &= C(P,K) - D + B(K), \end{aligned} \tag{2.1}$$

where $C(P,K)$ is the conversion rate of P into K, G is the generation rate of P, D is the dissipation rate of K, $B(X)$ is the flux of X across the boundaries of the volume (zero for global integrals), and t is time. However, as pointed out earlier in the introduction, zonal-mean and eddy decomposition provides a more detailed description of the energetics because it separates better the different processes behind the LEC. Based on this decomposition, the equations of the four-component LEC, integrated over a volume, are:

$$\begin{aligned} \frac{dP_m}{dt} &= -C(P_m,P_e) - C(P_m,K_m) + G_m + B(P_m) \\ \frac{dP_e}{dt} &= C(P_m,P_e) - C(P_e,K_e) + G_e + B(P_e) \\ \frac{dK_e}{dt} &= C(P_e,K_e) - C(K_e,K_m) - D_e + B(K_e) \\ \frac{dK_m}{dt} &= C(K_e,K_m) + C(P_m,K_m) - D_m + B(K_m), \end{aligned} \tag{2.2}$$

where the subscript m denotes the zonal mean and e the eddy component (including both transient and stationary eddies). The expressions used for the calculation of the different terms of the LEC are included in Appendix A. They are based on the formulation of Peixoto and Oort (1974), and resemble the expressions of Boer and Lambert (2008), which use the β function (described in Appendix A). Different from Boer and Lambert (2008), we calculate $C(P,K)$ from the vertical velocity and specific volume rather than from the gradient of geopotential height. However, the only mayor difference between the formulations of Peixoto and Oort (1974) and Boer and Lambert (2008) is the correction for topography achieved with the β function.

The strength of the LEC is given by the total conversion rate of P into K, i.e., $C(P,K) = C(P_m,K_m) + C(P_e,K_e)$ (see Fig. 2.1), which controls the rate of work of the atmosphere as a heat engine. For a stabilized climate, the reservoirs of P and K are assumed to remain constant so that the total conversion rate must equal the generation and dissipation rates. In this case the generation or the dissipation rate could also serve as a measure of the LEC-strength. However, these rates are difficult to calculate directly, and are usually obtained as residuals of the conversion terms. Therefore, the total conversion $C(P,K)$ is the most direct and reliable measure of the LEC-strength.

Decompositions

The formulation we use here is based on the Eulerian mean decomposition, where $X = \langle X\rangle + X'$ and $\langle X\rangle = [\langle X\rangle] + \langle X\rangle^*$, so that

$$X = [\langle X\rangle] + \langle X\rangle^* + X'. \tag{2.3}$$

Here, $\langle X\rangle$ represents the ensemble mean of the quantity X. It is the mean of X over all ensemble members for each day in the transient experiments, and is replaced by the time mean of X in the equilibrium runs (1xCO_2 and 2xCO_2) under the ergodicity assumption. Consistently, X' denotes the deviation from the ensemble (or time) mean, $\langle X\rangle$. $[\langle X\rangle]$ denotes the zonal mean of $\langle X\rangle$, and $\langle X\rangle^*$ its deviation. Additionally, the decomposition into global mean over a constant pressure level (denoted by $\widetilde{X}$) and its deviation (denoted by X'') is also used, for it appears in Lorenz's approximation equation for available potential energy (see Appendix). One has $[\langle X\rangle]'' = [\langle X\rangle] - \langle\widetilde{X}\rangle$.

LEC computations

The LEC-terms we compute here are the reservoirs P_m, P_e, K_e and K_m, the conversion rates $C(P_m,P_e)$, $C(P_e,K_e)$, $C(K_e,K_m)$ and $C(P_m,K_m)$, and, when splitting the atmosphere into upper and lower regions, the boundary flux terms $B(P_m)$, $B(P_e)$, $B(K_e)$, and $B(K_m)$. The generation and dissipation rates G_m, G_e, D_e, and D_m are estimated as residuals for the stabilized 1xCO_2 and 2xCO_2 runs, assuming constant reservoirs (see Appendix).

As mentioned before, the LEC computations of the CO_2-stabilized runs are based on time means instead of ensemble means. These time means are calculated as multi-year daily means, so that the output is one year of daily values for each LEC-term. This is reduced to single mean values by averaging over all days. The calculations in the transient runs are based on ensemble averages, so that the output of the computations consists of 10 years of daily values. This is averaged to a series of 10 yearly values for each LEC-term.

2.1.3 Results

2xCO$_2$ response

The LEC's for the equilibrium climates with 1xCO$_2$ and 2xCO$_2$ are shown in Figure 2.1. The 2-box diagram (Fig. 2.1a) shows a 7% decrease in $C(P,K)$, a 1% decrease in P, and a 10% increase in K. The decrease in $C(P,K)$ suggests that the cycle is weaker in the 2xCO$_2$ case. Nevertheless, the 2xCO$_2$-atmosphere has a larger reservoir of K. The 4-box diagram (Fig. 2.1b) reveals that the weaker LEC results from a decrease in the conversion due to both the mean and the eddy components, $C(P_m,K_m)$ and $C(P_e,K_e)$. The latter, accompanied by a weaker conversion of mean to eddy P, $C(P_m,P_e)$, indicates a reduction in baroclinic activity. On the other hand, the strong increase in K comes from an increase of 19% in K_m, while K_e has decreased by 2%. The increase in K_m is accompanied by a strengthening of the conversion term $C(K_e,K_m)$. Thus, the 4-box diagram further confirms the weakening of the LEC and the increase in K. However, the global results shown in Figure 2.1 do not give any information about the cause of these two opposite changes.

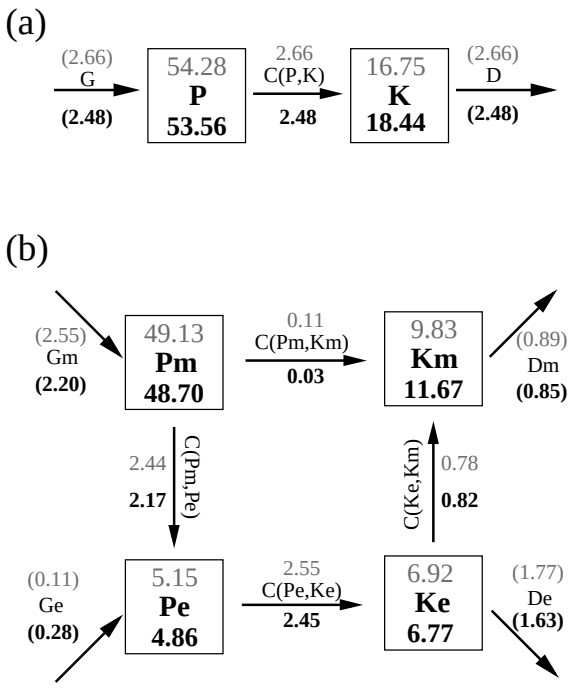

Figure 2.1: (a) 2-box diagram and (b) 4-box diagram of the LEC-terms for the 1xCO2 control run (above, gray) and the 2xCO2 equilibrium run (below, black). Generation and dissipation terms (in parenthesis) are obtained as residuals. Units are 10^5 J m^{-2} for reservoirs and W m^{-2} for conversion, generation and dissipation terms. Arrows show the direction corresponding to positive values; negative values imply opposite direction.

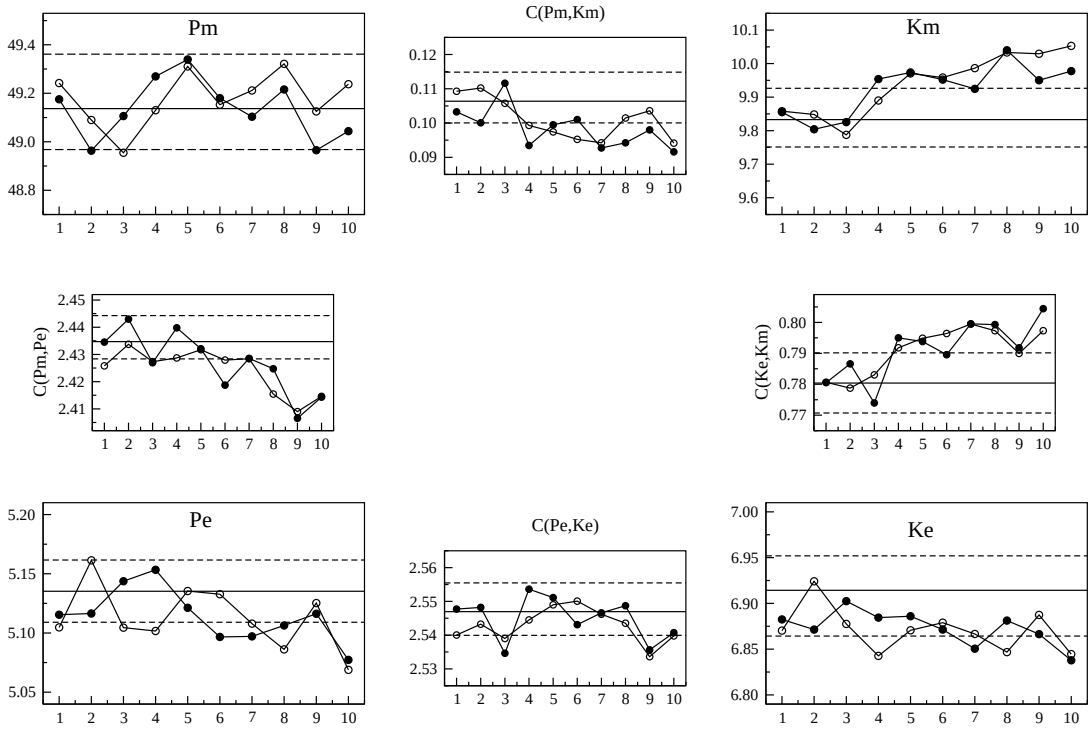

Figure 2.2: Mean LEC-terms for the 1xCO$_2$ control run (horizontal line) with an estimate of its 90% variability (dashed lines), and time series (in years) of the two transient ensembles (connected circles). Counterclockwise, starting from the upper left: P_m, $C(P_m, P_e)$, P_e, $C(P_e, K_e)$, K_e, $C(K_e, K_m)$, K_m, and $C(P_m, K_m)$. Units are 10^5 J m^{-2} for reservoirs and W m^{-2} for conversion terms.

Transient response

The transient ensembles allow us to track the changes in the different LEC-terms due to an increasing CO_2 concentration, to compare them with the 2xCO$_2$ changes, and to assess their robustness.

Figure 2.2 shows the time series of the LEC-terms obtained from the two transient ensembles (empty and filled circles), together with the mean value in the 1xCO$_2$ control run and an estimate of its 90% variability (horizontal lines), obtained by the Bootstrapping technique (von Storch and Zwiers, 1999). Using this technique, 100 random combinations of 50 years were generated from the 100 available years of the 1xCO$_2$ equilibrium run. For each combination, all the LEC-terms were computed. From this sample of 100 different 'realizations' of the LEC, we obtain an empirical distribution, which provides an estimate of the lower and upper bounds of the 90% variability of each LEC-term under the 1xCO$_2$ condition.

The changes in the transient runs are consistent with those in the equilibrium 2xCO$_2$ run. However, the magnitudes of the changes are smaller, partly because of the smaller forcing, and partly because of the non-equilibrium conditions. For P_m and $C(P_e, K_e)$, the changes in year 10 are not yet larger than the 90%-variability. On the contrary, the increase of K_m and

$C(K_e, K_m)$, and the decrease of $C(P_m, P_e)$, P_e, K_e, and $C(P_m, K_m)$, are statistically significant in year 10, or even earlier. Here, statistical significance means that the Null-hypothesis of no change can be rejected at a 10% significance level. The empirical distribution of the bootstrapped ensemble serves as the distribution of the test variable. One can conclude that the two opposing changes, the weakening in the cycle and the strengthening in K_m, are statistically significant transient responses.

Different from the equilibrium runs, which reveal only the equilibrium balances, the transient runs can provide evidence about which terms influence the increase of K_m. The terms that can directly affect K_m are the conversion terms $C(K_e, K_m)$ and $C(P_m, K_m)$. Figure 2.2 suggests that K_m increases because of the increase in the conversion from K_e to K_m, $C(K_e, K_m)$. The conversion term $C(P_m, K_m)$ is related to meridional overturnings, which work in both directions. For instance, under normal conditions, the thermally direct Hadley cell converts P_m into K_m, while K_m is generally converted into P_m in the indirect Ferrel cells at mid-latitudes. The observed decrease in $C(P_m, K_m)$ can be due to a reduced conversion from P_m to K_m in one region, to a higher conversion from K_m to P_m in another region, or to a combination that ends up with a net decrease. However, all these combinations would tend to decrease K_m, not to increase it. Therefore, the increase in K_m must be mostly driven by changes in the $P_m \rightarrow P_e \rightarrow K_e \rightarrow K_m$ side of the cycle, and not by changes in the direct P_m to K_m conversion.

The above consideration suggests also that the weakening of the LEC is not caused by a reduction in $C(P_m, K_m)$. Instead, Figure 2.2 shows that the weakening is associated with a decrease in the reservoirs of P_e and K_e, and the conversion terms $C(P_m, P_e)$ and $C(P_e, K_e)$. Although the latter does not show a statistically significant decrease in year 10, a negative trend is already visible, and the 2xCO_2 results suggest that this trend would produce statistically significant changes in a longer transient run. Overall, the transient time series suggest a decrease in eddy activity, with the strongest decrease in the conversion term $C(P_m, P_e)$, implying a reduction in baroclinicity.

The transient experiments allow us to identify two branches, which are consistent with the 2xCO_2 observed changes. One is characterized by an increase in K_m, and the other by a decrease in the eddy components. However, the connection between the two branches and the causes of each of them are not clear.

Vertical cross-sections

To understand the results shown in subsections 2.1.3 and 2.1.3, vertical cross sections of the integrands of each LEC-term are shown in Figure 2.3. Contours show the mean distribution in the 1xCO_2 control run, while color shaded are the 95%-significant changes for the 2xCO_2 run. The 95%-significance is tested using the bootstrapped empirical distribution of the 1xCO_2 LEC-terms. Only changes that are outside this 95% variability of the 1xCO_2 control run are shaded. These vertical cross sections do not give a complete description of the energetics

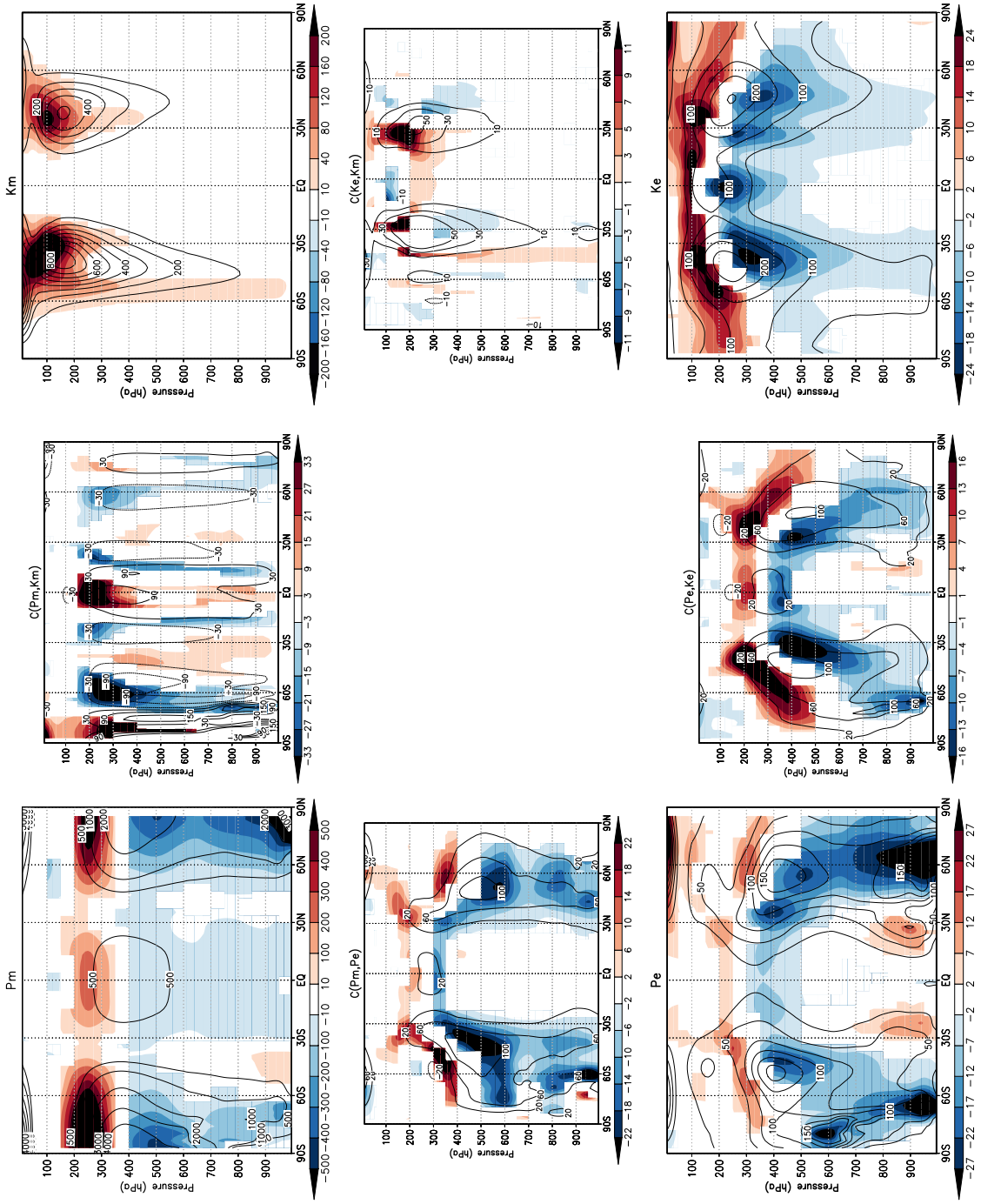

Figure 2.3: Vertical cross sections of the LEC terms for the 1xCO_2 control run (contours), and change in the 2xCO_2 run relative to the 1xCO_2 control run (color shaded, 95% significance). Counterclockwise, starting from the upper left: P_m, $C(P_m, P_e)$, P_e, $C(P_e, K_e)$, K_e, $C(K_e, K_m)$, K_m, and $C(P_m, K_m)$. Units are J Kg^{-1} for reservoirs, and $\times 10^{-5}$ W m^{-2} for conversion terms.

because internal flux terms, which are only zero for global integrals, are not included. Nevertheless, these plots give a good idea about the zonal and vertical distribution of the actual contributions to each LEC-term.

The first striking result is the pattern in the 2xCO_2-change of P_m (upper left diagram of Figure 2.3). There is a strong increase of P_m in the upper troposphere and lower stratosphere (between 150 hPa and 350 hPa), whereas throughout the middle and lower troposphere P_m decreases. This pattern is very well defined in P_m, but can also be seen in $C(P_m, P_e)$, P_e, $C(P_e, K_e)$ and K_e. However, it does not extend into $C(K_e, K_m)$ or K_m, where the increase-response dominates. A possible explanation for this comes from the vertical distribution of these terms (line contours). Both K_m and $C(K_e, K_m)$ are more concentrated in the upper levels of the troposphere with maximum values located above 300 hPa (they are related to the jet streams), whereas the other terms (P_m, P_e, K_e and the conversions between them) are widely spread throughout the troposphere, with maximum values located below 300 hPa, partly centered near 400 - 500 hPa. Because of these different vertical distributions, the global response of $C(K_e, K_m)$ and K_m is dominated by the values in the upper troposphere, where the increase-response is detected, while the global response of the other terms is dominated by the values in the middle and lower troposphere, where the decrease response is strong.

Figure 2.4 shows the changes in the vertical distribution of P_m in year 10 of one transient ensemble (color shaded) relative to the 1xCO_2 run distribution (contour lines). The corresponding plot for the other transient ensemble (not shown) is almost identical to the one shown in Figure 2.4. Also, the patterns of the other LEC-terms in both transient ensembles (not shown) are very similar but with smaller amplitude than the patterns of the 2xCO_2 run shown in Figure 2.3. The vertical cross-section of P_m (Fig. 2.4) differs from that obtained for the equilibrium runs (Fig. 2.3). In particular, there are larger differences between the Northern Hemisphere and the Southern Hemisphere in year 10 of the transient experiments than in the 2xCO_2 run. Although the upper troposphere shows a similar pattern to the 2xCO_2 case, in the middle and lower troposphere P_m decreases in the Northern Hemisphere, but increases in the Southern Hemisphere. This asymmetry of P_m in the Northern Hemisphere and Southern Hemisphere is strong in the transient warming, but becomes less pronounced in the 2xCO_2 equilibrium run, where the responses in the two hemispheres are similar.

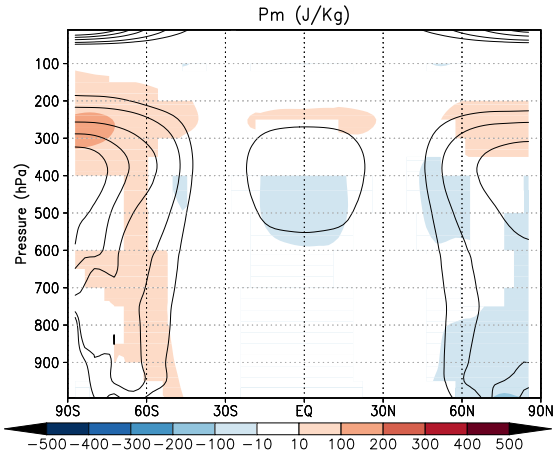

Figure 2.4: Vertical cross-section of P_m for the 1xCO_2 control run (contours), and change in year 10 of one transient ensemble relative to the 1xCO_2 control run (color shaded, 95% significance).

The analysis of the vertical cross-sections suggests a strengthening of the LEC-terms in the

upper levels and a weakening in the lower levels. However, as we noted before, it does not provide a rigorous description of the energetics. In particular, these vertical cross-sections do not tell us anything about possible exchanges or fluxes within the upper and lower levels. To explore the different behaviors in the upper and lower levels in a more rigorous manner, a splitting of the atmosphere is carried out in the next subsection.

Splitting the atmosphere

In order to obtain a more rigorous picture of the different contributions of the upper and lower levels to the global LEC-changes, we split the atmosphere at 350 hPa into the so-called upper and lower regions. We diagnose then the LEC-terms for each of these regions, plus the boundary fluxes at the isobaric surface of 350 hPa. This level has been chosen because the pattern of change of P_m (upper left corner of Fig. 2.3) suggests it as the boundary between the region where P_m increases and the region where it decreases.

With this procedure we do not intend to carry out a local analysis of the LEC for any of these two regions. This would be incorrect, due to the global formulation of the LEC. To carry out a local analysis, a different energetic formulation, such as that given by Marquet (1991), should be used. However, the aim of this section is not a local analysis of the LEC in the upper or lower regions. We split the global LEC in order to identify two contributions to the global LEC in a more rigorous way than just looking at vertical cross-sections. The added value of this splitting procedure comes from the calculation of the boundary fluxes of the reservoirs, which allows us to estimate (as residuals) the generation and dissipation rates in each region.

The 2-box diagram of the LEC with the split atmosphere (Fig. 2.5) reveals that most of the generation of P occurs in the lower region, as well as the conversion into K and its further dissipation, i.e., most of the energetic activity takes place here. The reservoir of P has also a higher contribution from the lower region, whereas kinetic energy is mostly stored in the upper

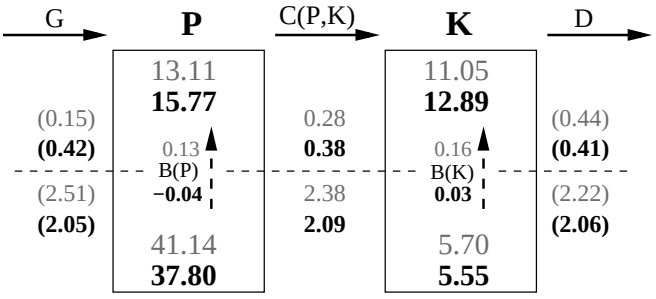

Figure 2.5: 2-box LEC computed for the atmosphere split at 350 hPa (dashed line), including boundary fluxes (dashed arrows). Values are for the 1xCO_2 control run (gray, above) and for the 2xCO_2 equilibrium run (below, black). Generation and dissipation terms (in parenthesis) are obtained as residuals. Units are 10^5 J m^{-2} for reservoirs and W m^{-2} for conversion, generation, dissipation, and boundary flux terms. Arrows show the direction corresponding to positive values; negative values imply opposite direction.

region, where little dissipation takes place. The boundary fluxes of K and P go upward, from the region with a stronger energy conversion to the region with a weaker energy conversion. The fact that the boundary fluxes are small compared to the generation, conversion, and dissipation terms in the lower region indicates that the annual-mean energy exchange between the upper and lower region is small.

Under a CO_2 doubling (bold numbers in Fig. 2.5), the LEC-terms of the 2-box diagram increase in the upper region and decrease in the lower region. The strength of the cycle (measured by $C(P,K)$) increases from 0.28 W m^{-2} to 0.38 W m^{-2} (about 36%) in the upper region, and decreases from 2.38 W m^{-2} to 2.09 W m^{-2} (about 12%) in the lower region. In order to visualize better how the changes in generation, conversion and dissipation take place in each region it is useful to focus only in the changes in these terms and the boundary fluxes, leaving the reservoirs aside. The changes in generation, conversion, dissipation, and boundary fluxes in each of the regions (Fig. 2.6) reveal that the largest changes show up in the generation rates. Due to the change in the boundary flux $B(P)$, these strong changes in generation are balanced by weaker changes in the conversion rate $C(P,K)$ in each region. In other words, the strong change in generation—increase in the upper region and decrease in the lower region—is followed by a weaker change in the conversion term $C(P,K)$. Going one step further, the lower region decrease of $C(P,K)$ is balanced by a decrease in the dissipation term D—although again of less magnitude—and a decrease in the upward boundary flux $B(K)$. On the contrary, the upper region increase of $C(P,K)$ is not followed by an increase in dissipation, as one would expect, but rather by a slight decrease. This is because the reduction in the upward flux $B(K)$ —probably driven by the decrease in energetic activity in the lower region—exceeds the increase in the conversion rate $C(P,K)$ of the upper region. However, this reduction in dissipation is very small. Summing up, the strong changes that start in the generation rates are followed by weaker changes in the conversion of P into K, and finally only the lower region decrease is followed by a decrease in the dissipation rate. The upper region increase of the conversion rate is mostly balanced by a decrease in the upward flux $B(K)$, instead of an increase in the dissipation rate.

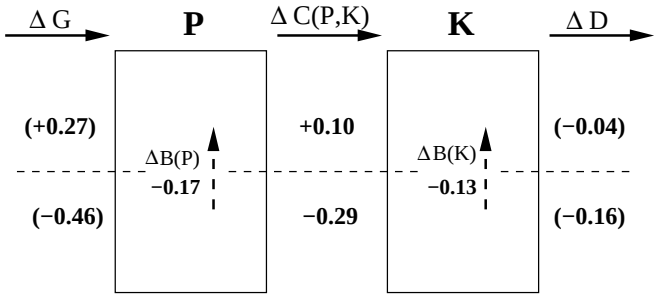

Figure 2.6: 2xCO_2 changes in generation, conversion, dissipation and boundary flux terms in the 2-box LEC for the atmosphere split at 350 hPa (dashed lines). Generation and dissipation terms (in parenthesis) are obtained as residuals. Units are W m^{-2}.

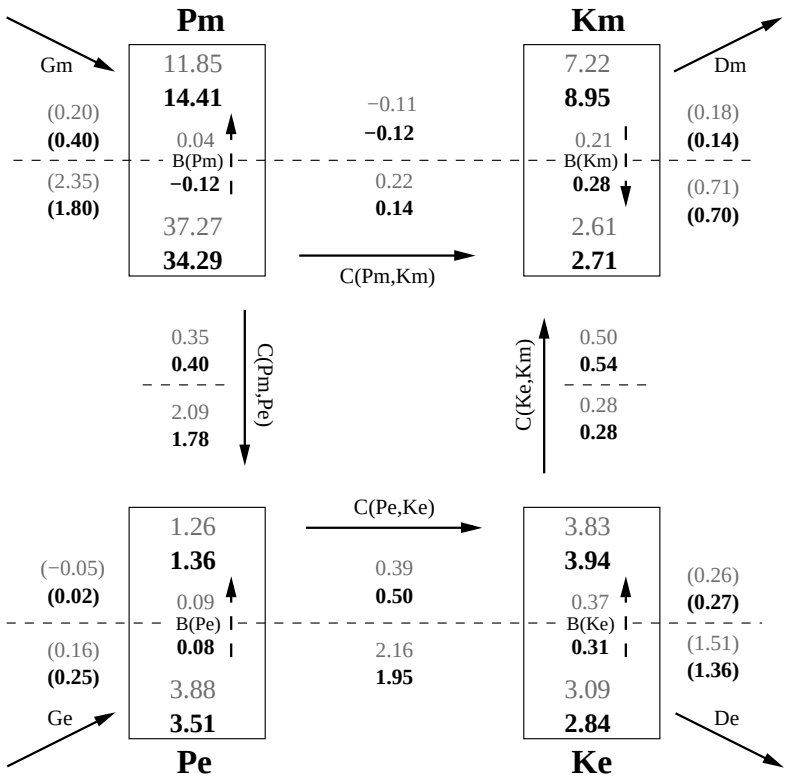

Figure 2.7: 4-box LEC computed for the atmosphere split at 350 hPa (dashed lines), including boundary fluxes (dashed arrows). Values are for the 1xCO_2 control run (gray, above) and for the 2xCO_2 equilibrium run (below, black). Generation and dissipation terms (in parenthesis) are obtained as residuals. Units are 10^5 J m^{-2} for reservoirs and W m^{-2} for conversion, generation, dissipation and boundary flux terms. Arrows show the direction corresponding to positive values; negative values imply opposite direction.

To get a closer look into the split-LEC responses, we also computed the 4-box LEC diagram for the split atmosphere (Fig. 2.7). A similar response is seen here: in general, LEC-terms in the upper region increase, while they decrease in the lower region. Regarding the reservoirs, the only exception is K_m, which increases in both regions. However, it only increases by 4% in the lower region, while it increases by 24% in the upper one. Just as for the 2-box LEC, we have computed the changes in generation, conversion, dissipation and boundary flux terms of each region, in order to track better the changes in energetic activity. These are shown in Figure 2.8.

Just as in the 2-box case, the strongest changes are in the generation rates, in particular for G_m, the generation rate of P_m. Focusing now on the upper region, we see that the strong increase in G_m (+0.20 W m^{-2}) is followed by an increase of 0.05 W m^{-2} in $C(P_m, P_e)$, while the rest is balanced by a reduction in the upward flux $B(Pm)$. This increase in $C(P_m, P_e)$, combined with an additional increase of 0.07 W m^{-2} in G_e, is followed by an increase of

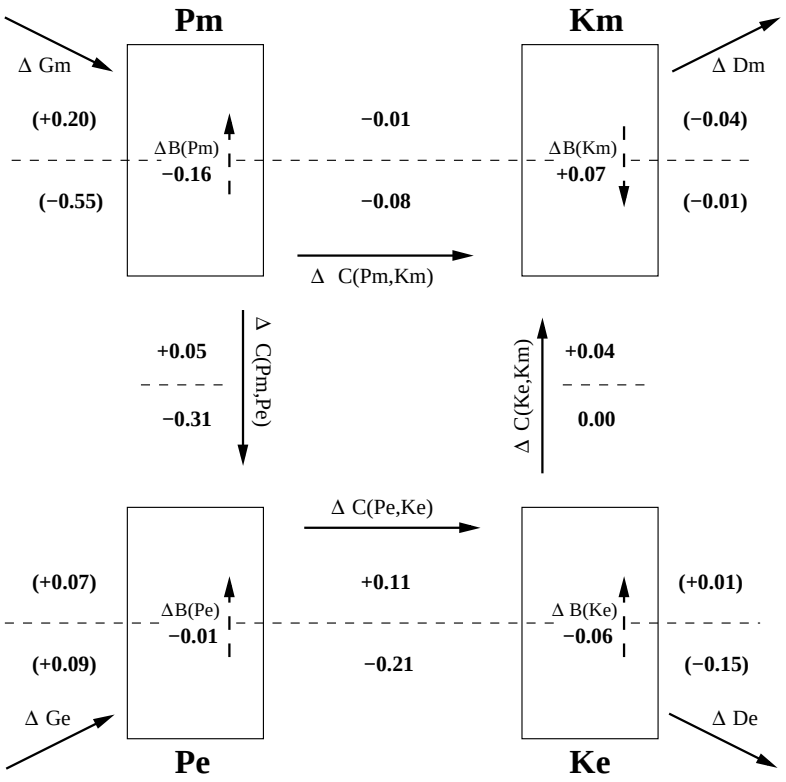

Figure 2.8: 2xCO$_2$ changes in generation, conversion, dissipation and boundary flux terms in the 4-box LEC for the atmosphere split at 350 hPa (dashed lines). Generation and dissipation terms (in parenthesis) are obtained as residuals. Units are W m^{-2}.

0.11 W m^{-2} in $C(P_e, K_e)$. This is followed by a small increase of 0.01 W m^{-2} in the dissipation term D_e and an increase of 0.04 W m^{-2} in $C(K_e, K_m)$. The remaining 0.06 W m^{-2} are balanced by a decrease in the upward flux $B(K_e)$. However, no increase in the upper region dissipation term D_m is obtained, but rather a decrease of 0.04 W m^{-2}. The increase in $C(K_e, K_m)$ is exceeded by an increase in the downward flux $B(K_m)$, so that D_m must slightly decrease in order to reach balance. However, the increase in LEC-strength in the upper region is quite consistent throughout the whole cycle.

The strongest response in the lower region is a decrease in G_m of 0.55 W m^{-2}. $C(P_m, P_e)$ decreases by 0.31 W m^{-2}, and combining this with an increase of 0.09 W m^{-2} in G_e, $C(P_e, K_e)$ decreases then by 0.21 W m^{-2}. This decrease in $C(P_e, K_e)$ is then completely compensated by a decrease of 0.15 W m^{-2} in the dissipation rate D_e and a decrease of 0.06 W m^{-2} in the upward flux $B(K_e)$. This implies that the weakening response disappears when we look further into the conversion term $C(K_e, K_m)$, which does not change in the 2xCO$_2$ run. This shows why the weakening response does not reach further than K_e. It is compensated by less dissipation and less upward flux $B(K_e)$, but the conversion rate of K_e into K_m remains unchanged. On the other hand, even though the weakening response only reaches up to K_e, it

takes place in the region of more energetic activity and shows larger changes than the strengthening response of the upper region. This explains why the weakening response dominates the globally integrated LEC.

It seems very reasonable that such a strong pattern of increase and decrease in the generation of P_m, which is usually considered as the starting point of the LEC, is driving the strenthening and weakening responses of the cycle. In this case, the pattern of temperature change is crucial for understanding the changes in G_m and in P_m. The next section examines the role of the warming pattern.

Patterns of temperature change and mean static stability

We know that P is closely related to the temperature distribution. More specifically, P, as computed for the LEC, is proportional to the variance of spatial temperature anomalies, i.e., to the mean square of temperature difference relative to the global mean temperature, and to γ, the *inverse mean static stability* (see Appendix A). Hence, a statically more stable atmosphere has less P. Evaluating changes in horizontal temperature variance, and changes in mean static stability may help us to understand the changes in P.

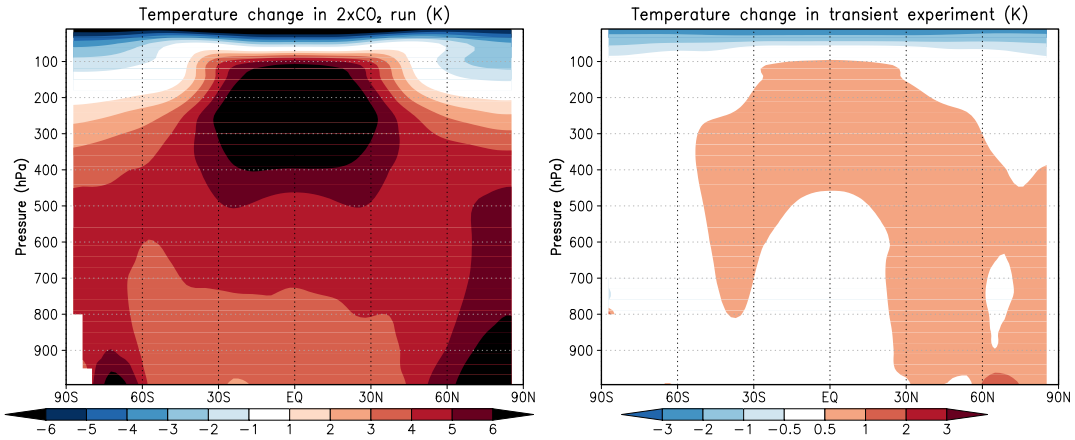

Figure 2.9: Zonal and annual mean temperature change in the $2xCO_2$ run (left) and in year 10 of one transient ensemble (right) relative to the $1xCO_2$ control run.

We will first focus on the changes in the horizontal variance of temperature on P. The equilibrium climate change signal (Fig. 2.9, left panel) is characterized by a stronger warming in the tropics than in the high-latitude region in the upper troposphere, but a stronger warming in the high-latitude region than in the tropics in the lower troposphere. Given that the temperature decreases poleward throughout the troposphere, the climate change signal implies an increase in equator-to-pole temperature difference in the upper troposphere, and a decrease in the same temperature difference in the lower troposphere. Figure 2.10 summarizes these two opposite responses of temperature. This plot shows the zonally-averaged temperature change at 250 hPa

and at 2 meters height. At 250 hPa (empty circles) the temperature change increases the meridional temperature gradient at all latitudes. At 2 meters height (filled circles), the warming is stronger at high latitudes than at low latitudes, causing a decrease in the meridional temperature gradient. As a result, P_m increases in the upper troposphere, but decreases in the lower troposphere. The decrease of P_m is stronger in the Northern Hemisphere than in the Southern Hemisphere due to a stronger warming at northern high-latitudes.

Having this relationship between temperature changes and P_m-changes in mind, it is also possible to understand the difference between the response of P_m in the transient ensemble and in the 2xCO_2 run. The right panel in Figure 2.9 shows that the warming in year 10 is much smaller than in the 2xCO_2 run. In year 10, the warming occurs mainly in the upper tropical troposphere and in the Northern high latitudes, and does not exceed 1K (except for a very small region near the surface of the Northern Hemisphere). In the 2xCO_2 run it is always above 3K, and even above 7K in the large regions of stronger-warming. This explains the smaller amplitudes in the changes of the LEC-terms in the transient runs. On the other hand, no warming is yet visible in year 10 at the southern high latitudes (in neither the upper nor the lower region). This means that P_m should slightly increase there throughout the whole troposphere. This increase is not only due to the tropical warming. More importantly, it is due to a feedback process in and over the Southern Ocean that keeps the temperature over the Southern Ocean nearly unchanged in the transient runs (von Storch, 2008). Such a process is missing in the Northern Hemisphere. The initial increase of P_m in the Southern Hemisphere (Figure 2.4) is therefore related to the faster warming of the Northern Hemisphere in comparison to the Southern Hemisphere warming. Once the warming is more symmetric, as in the stabilized 2xCO_2 run, this transient response disappears. P_m decreases in the middle and lower troposphere of both Southern and Northern Hemispheres, although not with complete symmetry (P_m in Fig. 2.3).

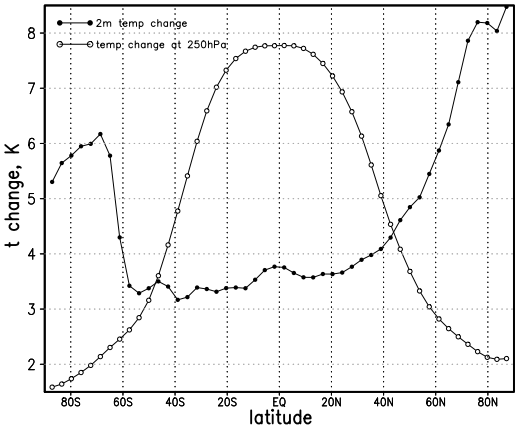

Figure 2.10: Differences in zonally averaged 2-meter temperature (filled circles) and zonally averaged temperature at 250 hPa (empty circles) between the 2xCO_2 run and the 1xCO_2 control run, in K.

Consider now the effect of changes in γ in the P_m response. γ is an inverse measure of the mean static stability, and therefore has variations only in the vertical. Hence, it cannot cause any latitudinal pattern in the P_m-response. Only mean vertical changes in P may be caused by changes in γ. From Figure 2.11 we see that γ decreases throughout the layer between 300 hPa and the surface, with a maximum decrease of about 15% at 400 hPa. It increases in the region above 300 hPa, but never more than 9%. This means that on average the atmosphere becomes

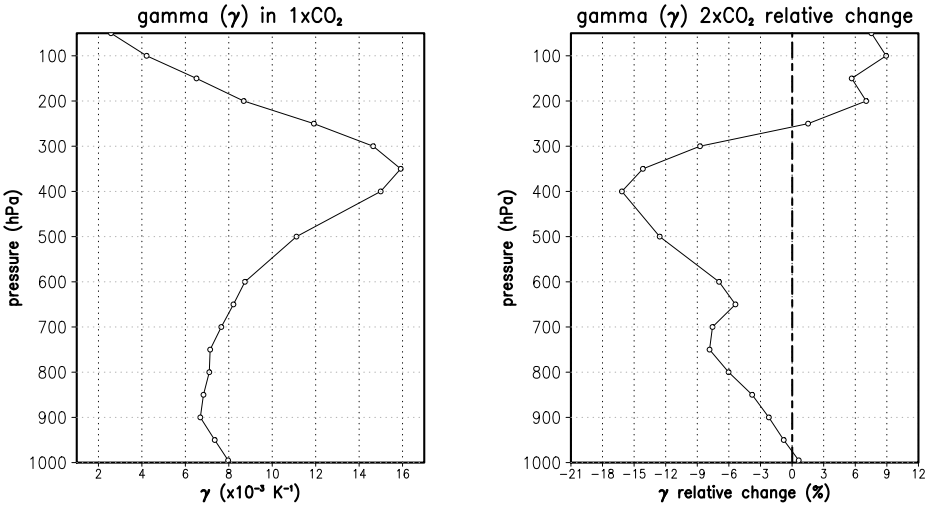

Figure 2.11: Mean value of gamma (γ) in 1xCO_2 run (left) and its relative change (right) in the 2xCO_2 run (difference divided by the 1xCO_2 value).

more stable below 300 hPa, and less stable above this level. This affects P_m by increasing it above 300 hPa, and decreasing it below.

However, changes in P_m are due to the combination of both effects (γ and temperature variance). In order to evaluate the relative impact of each of the two effects on the changes in P_m, we show the vertical profile of the relative change in P_m due to doubling of CO_2 (Figure 2.12). Comparing this plot with the relative change of γ (Figure 2.11) gives an idea of the contribution of the changes in γ to the mean changes of P_m. The remaining changes, not explained by the changes in γ, must be due to horizontal temperature variance changes.

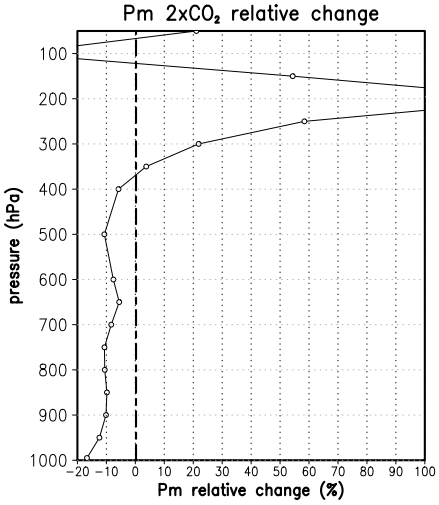

Figure 2.12: Global mean vertical profile of the relative change of P_m in the 2xCO_2 run (difference divided by the 1xCO_2 value).

Starting from the surface and until about 700 hPa, P_m decreases by about 10%. Near the surface it even decreases by almost 20%. On the other hand γ-changes start from almost zero at the lowest level, to about 7-8% decrease at 700 hPa. This suggests that in this region, changes in P_m are dominated by changes in temperature variance and not by changes in γ. However, from 700 hPa up to about 450 hPa, the relative changes of P_m and of γ are similar in magnitude, and they both show a relative minimum at 650 hPa. This suggests that in this region, which is

roughly speaking the "free troposphere", changes in γ are the main reason for the changes in P_m. This is also consistent with the fact that in this region the warming is rather homogeneous (see left panel of Figure 2.9), and therefore does not change the horizontal temperature variance significantly.

In the remaing upper levels, γ starts with a strong decrease of about 15% at 450 hPa, to an increase of about 6-9$\%$ at 200 hPa and above. However, P_m is already increasing at 350 hPa, and reaches a maximum increase of 140% at 200 hPa (out of scale in Figure 2.12). This strong increase of P_m in the upper levels cannot be explained by the small changes in γ. Instead, the P_m-changes above 400 hPa must be due to the changes in temperature variance because of the strong tropical upper-troposphere warming, as mentioned above.

2.1.4 Conclusions and discussion

The LEC-changes due to CO_2-increases reveal fundamental aspects of the dynamical responses of the atmosphere in a warming climate. These changes are studied using the coupled ECHAM5/MPI-OM atmosphere-ocean-sea-ice model. We analyzed a 1xCO_2 control climate, a stabilized 2xCO_2 climate, and two ensembles of transient experiments with 3%-CO_2 increase per year for 10 years. Two main conclusions are obtained.

First, the LEC-changes result from a dual role of the warming pattern, characterized by the strongest warming in the tropical upper-troposphere and in lower-level high-latitudes. This pattern causes an increase of P_m in the upper troposphere (upper region), and a decrease of P_m in the lower troposphere, near the surface. In the free troposphere—roughly between 700 hPa and 400 hPa—where the warming is approximately homogeneous, the increase in mean static stability is responsible for a decrease in P_m. The result is a decrease in P_m throughout both the lower and middle troposphere (lower region), and an increase in the upper region. Our calculations also show that an increase in CO_2 concentration leads to a greater generation of P in the upper troposphere and a reduced generation of P in the lower troposphere. This, together with the expected response of baroclinic activity due to the changes in temperature gradients and static stability—and therefore to the changes in P_m—, explains why we find a general strengthening of the LEC in the upper region (of about 36% in $C(P,K)$) and a general weakening of the LEC in the lower region (of about 12% in $C(P,K)$) in the 2xCO_2 climate. However, the total dissipation decreases in both regions (although only slightly in the upper one). When integrated globally, the weakening of the LEC in the lower region dominates, and leads to decreases in the part of the LEC that links P_m to P_e to K_e. The strengthening of the LEC in the upper region, on the other hand, appears together with a significant increase in K_m.

The second conclusion is that the transient responses are less north-south symmetric than the equilibrium responses. In the transient runs, the weakening of the lower tropospheric LEC is stronger in the Northern Hemisphere than in the Southern Hemisphere. In fact, the available potential energy has even increased in the southern lower and middle troposphere in year 10. This transient feature is likely due to a coupled feedback process that tends to maintain the

latitudinal temperature gradient over the Antarctic Circumpolar Current (von Storch, 2008). This process is much less pronounced in the Northern Hemisphere, leading to a faster and stronger high-latitude warming there.

The weakening of the LEC in the middle and lower troposphere is consistent with earlier studies (Boer, 1995; Marquet, 2005, 2006). It is expected from the reduced equator to pole temperature gradients (because of high-latitude warming) and the reduced land-sea contrasts during the winter season (because of stronger warming over continents). It reflects a reduction in baroclinic activity. However, we show that this weakening reflects only one prominent change in the global LEC. The other prominent feature is the increase in K_m in the upper troposphere.

The strong increase in K_m is not only seen in the ECHAM5/MPI-OM runs, but also found in climate change experiments using other GCM's. For example, Lorenz and DeWeaver (2007) found that the IPCC-AR4-climate models show a strengthening and poleward shifting of the tropospheric zonal jets, of transient kinetic energy and of momentum flux in response to global warming. Fyfe and Saenko (2006) report 12 GCM's that show a consistent strengthening and poleward shifting in zonal wind stress in the Southern Hemisphere extra-tropics. Although these quantities are not exactly the same we use here, they do suggest that the increase in K_m, which is dominated by the tropospheric zonal jets, is not just an ECHAM5-feature, but is likely a robust signal in global warming simulations of the IPCC-AR4 climate models. In our results, the poleward shifting of the tropospheric zonal jets is visible in the increase of K_m in the southern hemisphere in the poleward-side of the jet throughout the whole troposphere. On the other hand, the increase in LEC-strength in the upper region is consistent with results from Marquet (2006). Using a local energetics formulation for the winter season of the North Atlantic region, he observed an increase in the energetic activity in the jet regions, as well as a reduction in the energetic conversions in the low troposphere.

The pattern of tropical warming in the upper troposphere and high-latitude warming in the lower troposphere represents the typical warming signal, and is also found in the IPCC-AR4 climate change runs (Meehl et al., 2007). Held (1993) pointed out the dual role of this warming pattern for baroclinic eddies: baroclinic eddies can be strengthened by an increase in pole to equator temperature gradient in the upper troposphere, but weakened by the decrease in this gradient in the lower troposphere. Our results confirm this dual role of the warming pattern. Moreover, we are able to quantify the dual role in terms of the strengthening and weakening of the LEC in the upper and lower troposphere.

The tropical upper-troposphere warming is known to be related to moist convection within the tropics (Held, 1993). This would suggest that moisture is an important factor in the upper-level strengthening of the LEC. Lorenz and DeWeaver (2007) argue that the strengthening of the polar jets, which they find in all IPCC-models, is mostly driven by the rising of the tropopause rather than by the increase in moisture content. However, one could also argue that the tropopause rises mostly due to the strong tropical upper-troposphere warming, which is caused by moisture effects. Furthermore, part of the weakening response of the LEC in the

lower and middle troposphere can be related to the increase in mean static stability, which is also related to water vapor effects (Schneider et al., 2010). We will be able to reach more conclusive statements regarding this matter in the remaining text.

2.2 Responses obtained with the higher resolution ECHAM5/MPI-OM coupled model

2.2.1 Introduction

The coupled model runs used for the previous section show a clear energetics response due to higher CO_2 concentrations. However, they correspond to relatively coarse resolution model runs (T31L19 for the atmosphere and GR30L40 for the ocean). In this section we analyse the energetics response when doubling CO_2 concentrations in a coupled model run with T63L31 spectral resolution for the atmosphere and GR15L40 resolution for the ocean. We have two main objectives:

- To verify if the equilibrium energetics response described in the previous section is also valid for higher resolution model runs.
- To perform an additional decomposition of the eddy terms of the LEC into transient and stationary eddy components, in order to study their independent responses to a doubling of CO_2.

Regarding the first objective, verifying our previous results with higher resolution model output provides valuable information on its own. Regarding the second objective, we want to separate the eddy components because a warmer climate may affect each of them in a different way. For example, the stronger warming over the continents could affect the stationary wave activity. It is not clear whether this is the case, and if yes, to what extent these changes contribute to the global energetics response. It is well known that the transient eddies have a larger contribution to the global energetic activity than the stationary eddies (Oort and Peixoto, 1974; Holton, 2004). On the other hand, we do not know if this is the case in terms of their response to a warmer climate. We want to obtain a clear answer to this. Furthermore, the second objective can be better addressed with a higher resolution model, as the eddy components are expected to be better described than with the lower resolution model.

2.2.2 Method

Model and experiments

The model setup of the coupled runs we use here is the same as the one used in the previous section (ECHAM5/MPI-OM atmosphere-ocean general circulation model), except for the resolution. The atmospheric component, ECHAM5.2.02a, has a T63L31 spectral resolution

($\approx 1.875^\circ \times 1.875^\circ$ and 31 vertical levels), and the ocean component, MPI-OM version 1.0, a GR15L40 resolution ($\approx 1.5^\circ \times 1.5^\circ$ and 40 vertical levels). We use two integrations performed for the IPCC fourth assessment report:

- The last 50 years (from a total of 505 years) of the pre-industrial control experiment PIcntrl (Roeckner et al., 2006), with a constant 1xCO_2 concentration of 280 ppm.
- The last 50 years of the 1%/year CO_2-increase experiment to doubling (run no.1) (Roeckner, 2004). In this run, the CO_2 concentration is doubled after 70 years, and kept constant for 150 additional years (see Fig. C.1 in Appendix C).

Lorenz Energy Cycle equations

We consider here the same LEC equations as in the previous section (equations 2.1 and 2.2), but we also go one step further in the decomposition of the LEC. We consider now the transient and stationary eddy components separately, so that $P_e = P_{se} + P_{te}$ and $K_e = K_{se} + K_{te}$. Here the subscript se denotes stationary eddy component, and te denotes transient eddy component. The LEC equations in expression (2.2) become now

$$\begin{aligned}
\frac{dP_m}{dt} &= -C(P_m, P_{se}) - C(P_m, P_{te}) - C(P_m, K_m) + G_m + B(P_m) \\
\frac{dP_{se}}{dt} &= C(P_m, P_{se}) + C(P_{te}, P_{se}) - C(P_{se}, K_{se}) + G_{se} + B(P_{se}) \\
\frac{dP_{te}}{dt} &= C(P_m, P_{te}) - C(P_{te}, P_{se}) - C(P_{te}, K_{te}) + G_{te} + B(P_{te}) \\
\frac{dK_{se}}{dt} &= C(P_{se}, K_{se}) - C(K_{se}, K_{te}) - C(K_{se}, K_m) - D_{se} + B(K_{se}) \\
\frac{dK_{te}}{dt} &= C(P_{te}, K_{te}) + C(K_{se}, Kte) - C(K_{te}, K_m) - D_{te} + B(K_{te}) \\
\frac{dK_m}{dt} &= C(K_{se}, K_m) + C(K_{te}, K_m) + C(P_m, K_m) - D_m + B(K_m).
\end{aligned} \tag{2.4}$$

There are only two entirely new terms that correspond to the conversion rates between the stationary and transient components of each eddy reservoir: $C(P_{te}, P_{se})$ and $C(K_{se}, K_{te})$. The other "new" terms are only a decomposition of old terms:

$$\begin{aligned}
C(P_m, P_e) &= C(P_m, P_{se}) + C(P_m, P_{te}) \\
C(P_e, K_e) &= C(P_{se}, K_{se}) + C(P_{te}, K_{te}) \\
C(K_e, K_m) &= C(K_{se}, K_m) + C(K_{te}, K_m).
\end{aligned} \tag{2.5}$$

The exact expressions for each of the new terms are given in Appendix B. They are fully consistent with the previous expressions given in Appendix A, as well as with the formulations of Peixoto and Oort (1974) and of Boer and Lambert (2008).

Decompositions

Regarding the decomposition of the different variables, we base our equations and computations on the same Eulerian mean decomposition described in the previous section (equation (2.3)).

Note that the stationary and transient eddy decomposition separates quadratic terms of the form $\left[\langle X\rangle^{*2}\right]$ for the stationary eddy terms, and $\left[X'^2\right]$ for the transient eddy terms. The stationary eddy components describe departures from the *zonal-mean* field that are persistent in time, and the transient eddy components describe the zonal mean of departures from the *time-mean* field. In the atmosphere, stationary eddies appear due to spatial inhomogeneities like topography and the position of continents; transient eddies result from dynamical instabilities and are related to storm activity.

LEC computations

The computations are done according to the equations given in Appendix A and B. Because we consider here only the equilibrium cases (1xCO_2 and 2xCO_2), the computations are based on time means and not on ensemble means, just as we did for the low-resolution equilibrium runs. For details about these computations, please refer to Section 2.1.2.

As opposed to the previous section, we cannot use here the Bootstrapping technique in order to estimate the statistical significance of the results. Each of the two equilibrium runs we use here is 50 years long, and provides us with only one ”realization” of the LEC. In order to apply the Bootstrapping technique we would need longer integrations so that we could generate a large number of ”realizations”. Unfortunately, this is not possible with these high-resolution runs. However, we have an estimate of the significance of the low-resolution response, which we can use as a reference for comparison. The features of the LEC-response in the low resolution 2xCO_2 case proved to be statistically significant with at least a 90% confidence interval. Therefore, as long as the high resolution response we obtain here is similar to the previous low resolution response, we can infer that it is also statistically significant.

2.2.3 Results - 2xCO_2 response

Warming pattern

Before showing here the LEC-response of the T63L31 resolution runs, we will first look at the zonal-mean temperature response of this new 2xCO_2 run, and compare it to the lower resolution runs. This should be a first indicator of any possible differences between the two resolutions, and, as we learned in the previous section, it will also help us to understand the energetics response that will be presented in the next subsections.

Comparing the zonal and time mean temperature change due to CO_2 doubling in the higher resolution runs (Fig. 2.13) with the coarse resolution runs (Fig. 2.9, left panel), we find that the high resolution 2xCO_2 run shows a smaller warming amplitude, but with a very similar

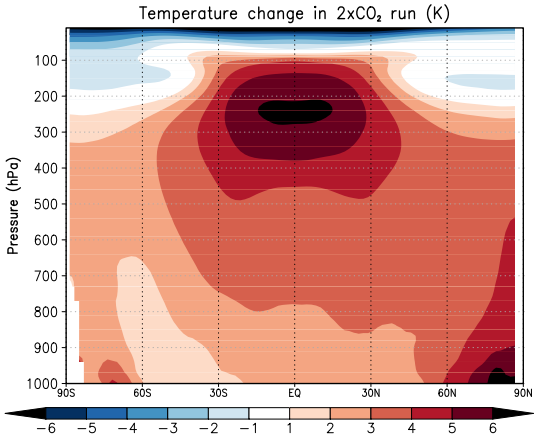

Figure 2.13: Zonal and annual mean temperature change in the $2xCO_2$ run with T63L31 resolution, relative to the $1xCO_2$ pre-industrial control run.

pattern. The regions with more than 6 K warming are smaller in the higher resolution runs, but the overall pattern, with the strongest warming in the upper tropical troposphere and in the surface high-latitude regions (mostly in the Northern Hemisphere) is the same. Several factors may be responsible for the difference in warming amplitude in the $2xCO_2$ response. First of all, the two integrations were carried out not only with different resolutions, but also with different versions of the model. However, the main reason for this difference is probably related to the period of time in which the $2xCO_2$ concentration is held constant in both experiments. The T63L31 $2xCO_2$ run was obtained by increasing the CO_2 concentration by 1% per year during 70 years, and then holding it constant for 150 years. We use here the last 50 years, but in order to obtain a fully equilibrated deep ocean, 100 years is certainly not enough. The low resolution $2xCO_2$ run that was used for the previous section has 880 years of integration with constant $2xCO_2$ concentration (Seiffert and von Storch, 2008), of which we use the last 100 years. This longer equilibrium integration certainly accounts for some further warming as the deep ocean approaches its equilibrium temperature. Nevertheless, the fact that the warming pattern in both cases is the same, suggests that the temperature response in the atmosphere in both cases is consistent, although with slightly different amplitudes. In Appendix C we show a more detailed description of the equilibrium conditions of this $2xCO_2$ run. Although there is still a positive trend in surface temperature, it is very small compared to its natural variability. We conclude that its atmosphere is sufficiently equilibrated so that the remaining trends should not affect the main energetics response. For further details, please refer to Appendix C.

Lorenz Energy Cycle

In order to visualize the changes in the energetic activity, we use the values obtained for the 2-box and 4-box LEC terms (Fig. 2.14) to calculate the changes in energy generation, conversion

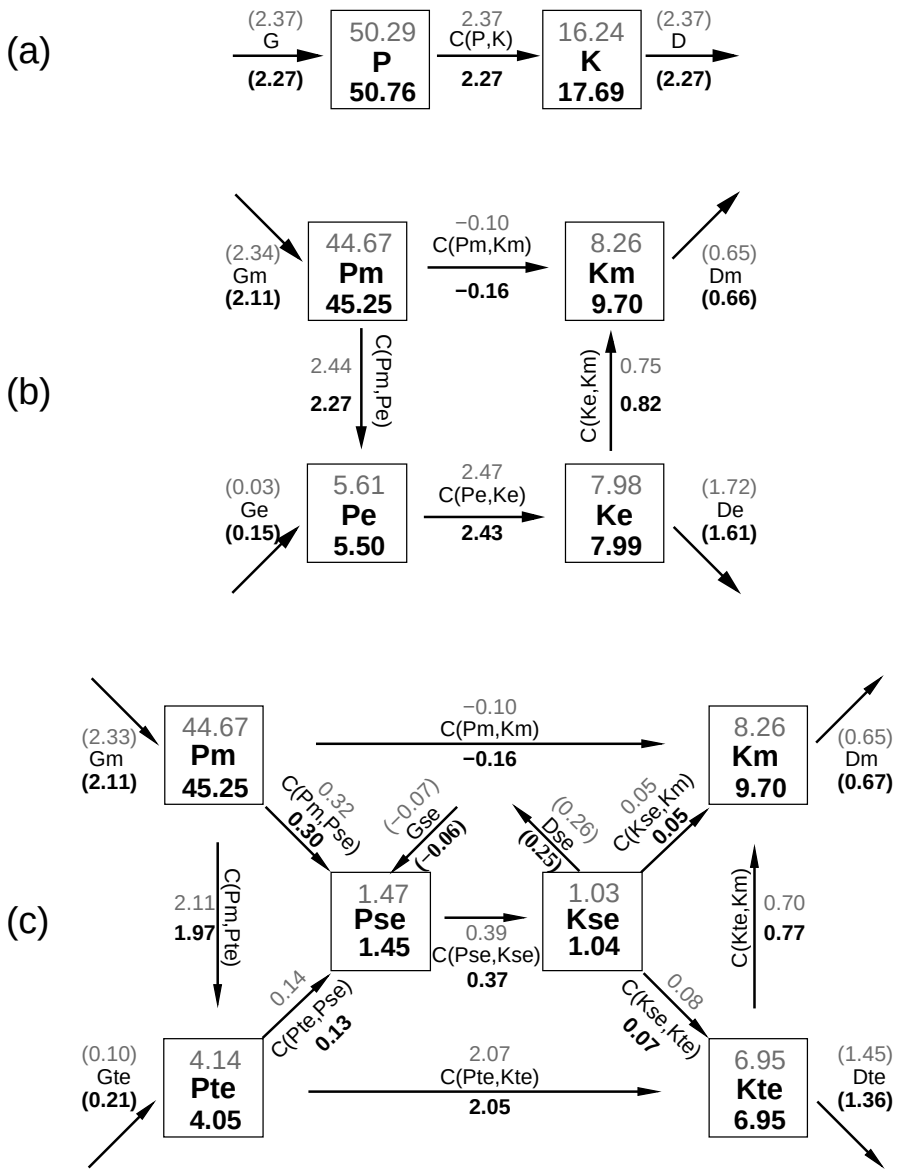

Figure 2.14: (a) 2-box, (b) 4-box, and (c) 6-box diagram of the LEC-terms for the 1xCO2 control run (above, gray) and the 2xCO2 equilibrium run (below, black) with T63L31 resolution. Generation and dissipation terms (in parenthesis) are obtained as residuals. Units are 10^5 J m^{-2} for reservoirs and W m^{-2} for conversion, generation and dissipation terms. Arrows indicate the direction corresponding to positive values; negative values imply opposite direction.

and dissipation rates due to CO_2 doubling (Fig. 2.15), leaving the changes in reservoirs aside (just as we did for the split-LEC in the previous section). First of all, we do not expect that the values of the LEC-terms in this case are exactly equal to the ones obtained with the lower resolution runs. This is evident when comparing Figures 2.14 and 2.1. For example, the total

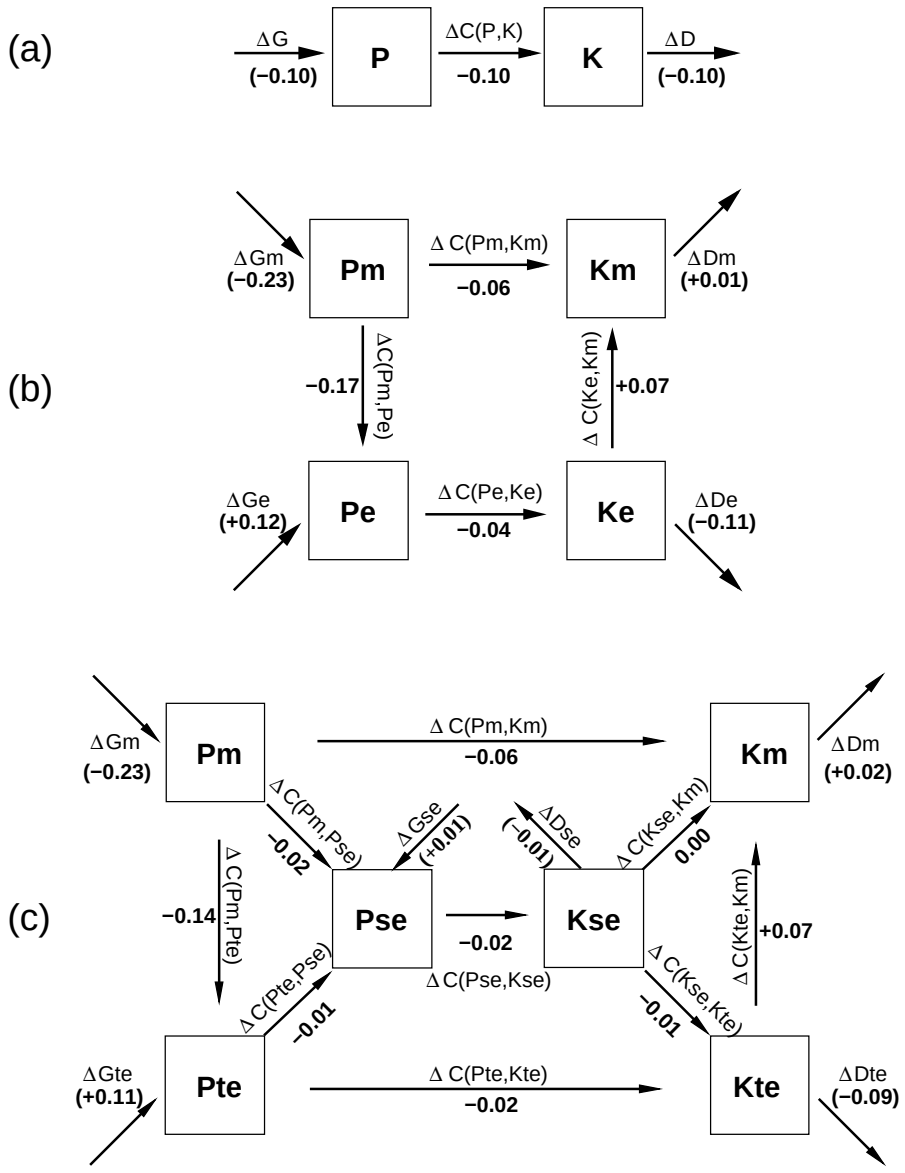

Figure 2.15: (a) 2-box, (b) 4-box, and (c) 6-box diagram of the changes in energy generation, conversion and dissipation rates in the LEC due to CO_2 doubling, evaluated from Figure 2.14. Units are W m^{-2}. Arrows indicate the direction corresponding to positive values; negative values imply opposite direction.

conversion term $C(P, K)$ in the T63L31 1xCO_2 pre-industrial run is of 2.37 W m^{-2}, while it is 2.66 W m^{-2} in the T31L19 1xCO_2 control run, even though both describe similar states of the atmosphere. These differences can be due to numerous reasons related to the model parametrizations, numerical resolution, etc. Tracing the causes of these differences can be useful in terms of model development, but it is not the aim of this work. Only in the case of a very large inconsistency should we worry about this. What we do expect is that the response

of the LEC-terms to a CO_2-doubling is similar.

The numbers in Figure 2.14(a) reveal a reduction of 4% in $C(P, K)$ (the total strength of the LEC), compared to a 7% reduction in the low resolution runs. K increases by almost 9% and P increases by 1%. In the low resolution runs, K increases by 10%, and P by 1% (Section 2.1.3). In other words, regarding the reservoirs of the 2-box LEC, the higher resolution response is very similar to the lower resolution response. The LEC-strength, i.e., the total P to K conversion rate ($C(P, K)$), decreases by 4.2%, compared to a 6.8% decrease in the low resolution runs. Thus, the response of the LEC-strength in the higher resolution runs is consistent with the response of the low resolution runs, but slightly weaker.

Regarding the 4-box LEC (Figure 2.14(b)), we find some small differences with respect to the low resolution runs, but no inconsistencies. In the following we describe these small differences in terms of percentual changes: K_e remains almost constant (only increases by 0.1%) in the high resolution runs; in the low resolution runs it decreases by 2.2%. P_e decreases in both cases, but only by 2% in the high resolution runs; it decreases by 5.6% in the low resolution runs. P_m increases by 1.3% in the high resolution runs, but it decreases by 0.8% in the low resolution runs. Regarding the reservoirs, the change in K_m is again the strongest of all: it increases by 17% in the high resolution runs. In the low resolution runs, it increases by 18.7%. The conversion terms show changes consistent with the low resolution runs, but with some small differences in magnitude: $C(P_m, P_e)$ weakens by 7% in the high resolution runs, and by 11% in the low resolution runs. $C(P_e, K_e)$ weakens by 1.6%, compared to 3.9% in the low resolution runs, and $C(K_e, K_m)$ strengthens by 9.3%, compared to 5.1% in the low resolution runs. $C(P_m, K_m)$—a number always very close to zero—decreases by 60%, compared to 72% in the low resolution runs.

In conclusion, looking at Figures 2.14 and 2.15, we observe the same overall response as in the low resolution runs (Figure 2.1), but slightly less pronounced. We find, as in the low resolution runs, a weakening in the path $P_m \rightarrow P_e \rightarrow K_e$, followed by a strengthening in $C(K_e, K_m)$ and a strong increase in K_m.

Vertical cross-sections

We show here the vertical cross-sections of the 4-box LEC-terms (Fig. 2.16) in order to visualize the zonal and vertical distribution of their response, just as we did in the previous section for the T31L19 resolution runs. For comparison with the previous results, this does not include yet the transient and stationary eddy decomposition.

In general terms, the plots in Figures 2.3 and 2.16 are very similar. Regarding the zonal mean distribution of the terms in the 1xCO_2 control runs (contoured lines), the main difference between the low and the high resolution runs is that there are slightly more detailed structures in the high resolution plots, specially in the lower levels, while the overall patterns remain the same. This is attributable to the increase in both horizontal and vertical resolution. Second, K_e has larger maximum values in the higher resolution runs, as well as larger global values. This

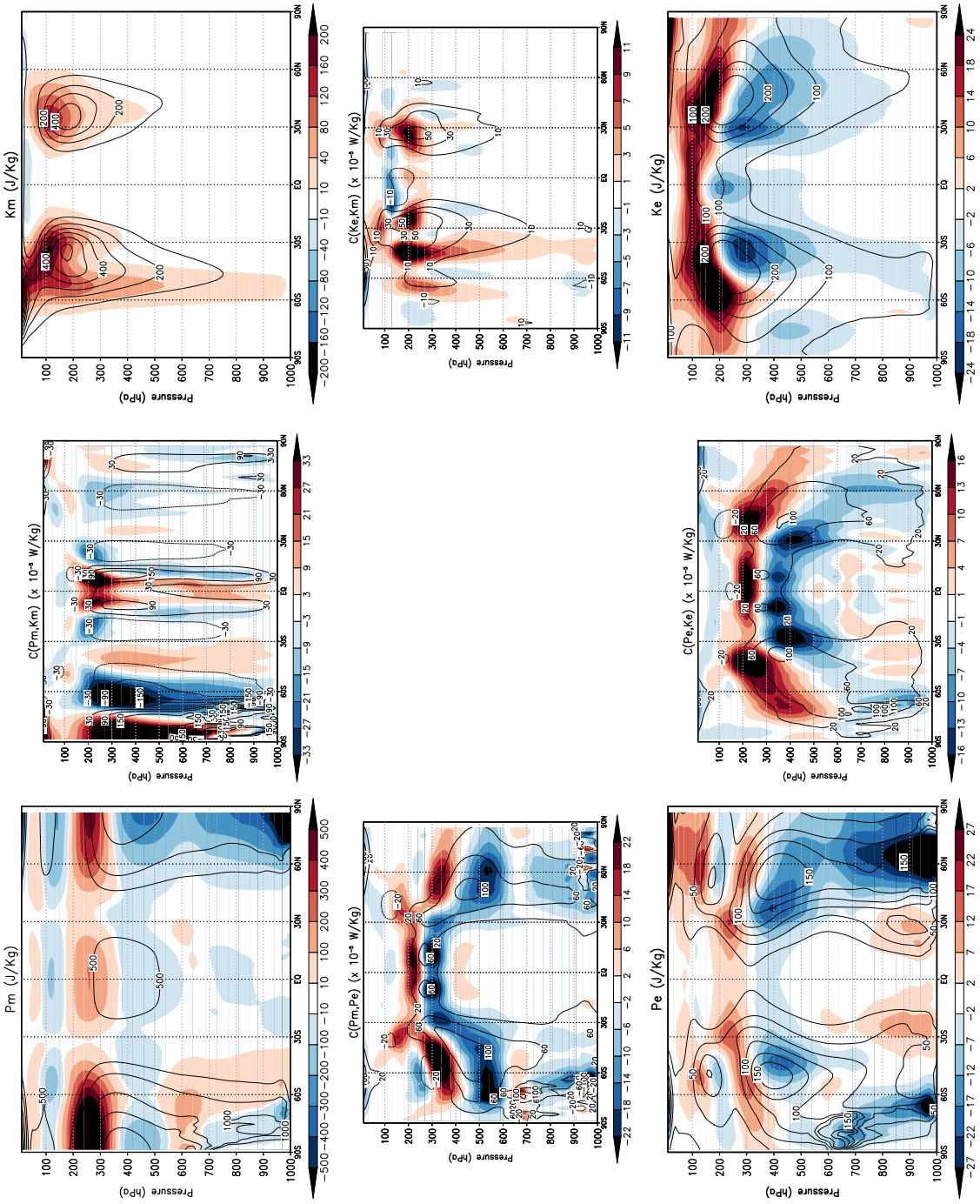

Figure 2.16: Vertical cross-sections of the 4-box LEC terms for the 1xCO_2 pre-industrial control run (contours), and their change in the 2xCO_2 run (color shaded). Counterclockwise, starting from the upper left: P_m, $C(P_m, P_e)$, P_e, $C(P_e, K_e)$, K_e, $C(K_e, K_m)$, K_m, and $C(P_m, K_m)$. Units are J Kg^{-1} for reservoirs, and $\times 10^{-5}$ W m^{-2} for conversion terms.

is not surprising, because the higher resolution model is expected to resolve smaller eddies. On the other hand, K_m has smaller maximum values in the high resolution runs, especially in the Southern Hemisphere, and also a smaller global value. This could be seen as a "compensation" for the difference in K_e so that total kinetic energy remains approximately constant in both resolutions. However, we do not find any clear reason for the difference in K_m other than a different tuning in both resolutions.

Regarding the changes due to CO_2 doubling, the biggest difference is in the Southern Hemisphere P_m-response. In the low resolution runs there is a general decrease, except for a small region between 60°S and 30°S near the surface, where P_m slightly increases. This region of P_m-increase extends higher up in the higher resolution runs, with a maximum around 600 hPa. It resembles to some extent the transient response in the previous section (Figure 2.4), where P_m increased throughout the whole tropospher in the Southern Hemisphere. Although not as strong as in the transient experiments, this feature might be due to the fact that the system is not yet fully equilibrated (as noted above and in Appendix C), and because the warming is weaker than in the low resolution runs. Furthermore, the decrease response in $C(P_m, P_e)$, P_e, $C(P_e, K_e)$ and K_e is slightly less pronounced in the higher resolution runs, especially in the Southern Hemisphere. This could also be related to the difference in the P_m-response in the Southern Hemisphere. Despite this, the patterns we observe in these vertical cross-sections are consistent in both resolutions. Just as before, they suggest a strengthening of the LEC in the region above 340 hPa, and a weakening below.

Transient and stationary eddy decomposition

We will now move to the transient and stationary eddy decomposition of the LEC-terms, which was not done with the lower resolution experiments. This should enable us to quantify the individual contribution of these components to the full response of the LEC to a CO_2-doubling.

The values of the corresponding LEC terms in this case (Fig. 2.14c) show that regarding both the reservoirs and the conversion terms, the eddy activity is dominated by the transient eddy terms, and the stationary eddy terms have smaller contributions, as expected. We find the same predominance of the transient eddy terms over the stationary eddy terms regarding the 2xCO_2-changes of P_e, $C(P_m, P_e)$ and $C(K_e, K_m)$. Their responses are clearly dominated by the changes in P_{te}, $C(P_m, P_{te})$ and $C(K_{te}, K_m)$, respectively (Figure 2.15(c)). Only in the conversion term $C(P_e, K_e)$ we observe the global response similarly distributed in both $C(P_{se}, K_{se})$ and $C(P_{te}, K_{te})$. In general, this decomposition suggests that the eddy activity and its response due to CO_2 doubling are dominated by the transient eddy response.

The vertical cross-sections of the decomposed reservoirs are shown in Figure 2.17, and of the decomposed conversion rates in Figure 2.18. Regarding the reservoirs, the pattern of increase in the upper troposphere and decrease further below is mainly due to the response of the transient components P_{te} and K_{te}. The main pattern of change of P_e to which we have refered to, comes from the pattern of change of P_{te}. The pattern of change of P_{se} reveals some particular features,

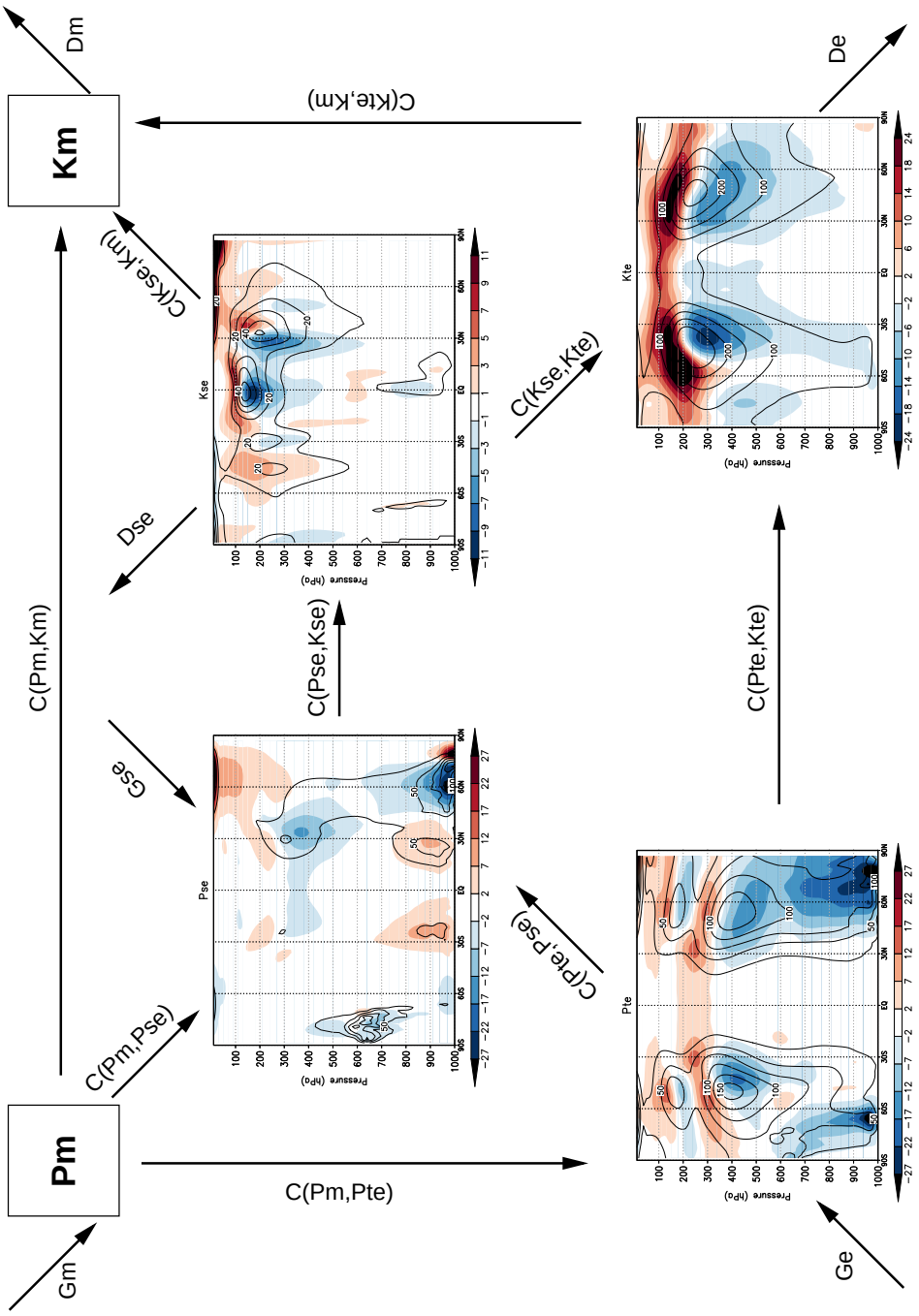

Figure 2.17: Vertical cross sections of the stationary and transient eddy reservoirs (P_{se}, P_{te}, K_{se} and K_{te}) for the 1xCO_2 pre-industrial control run (contours), and their change in the 2xCO_2 run (color shaded). Units are J Kg^{-1}.

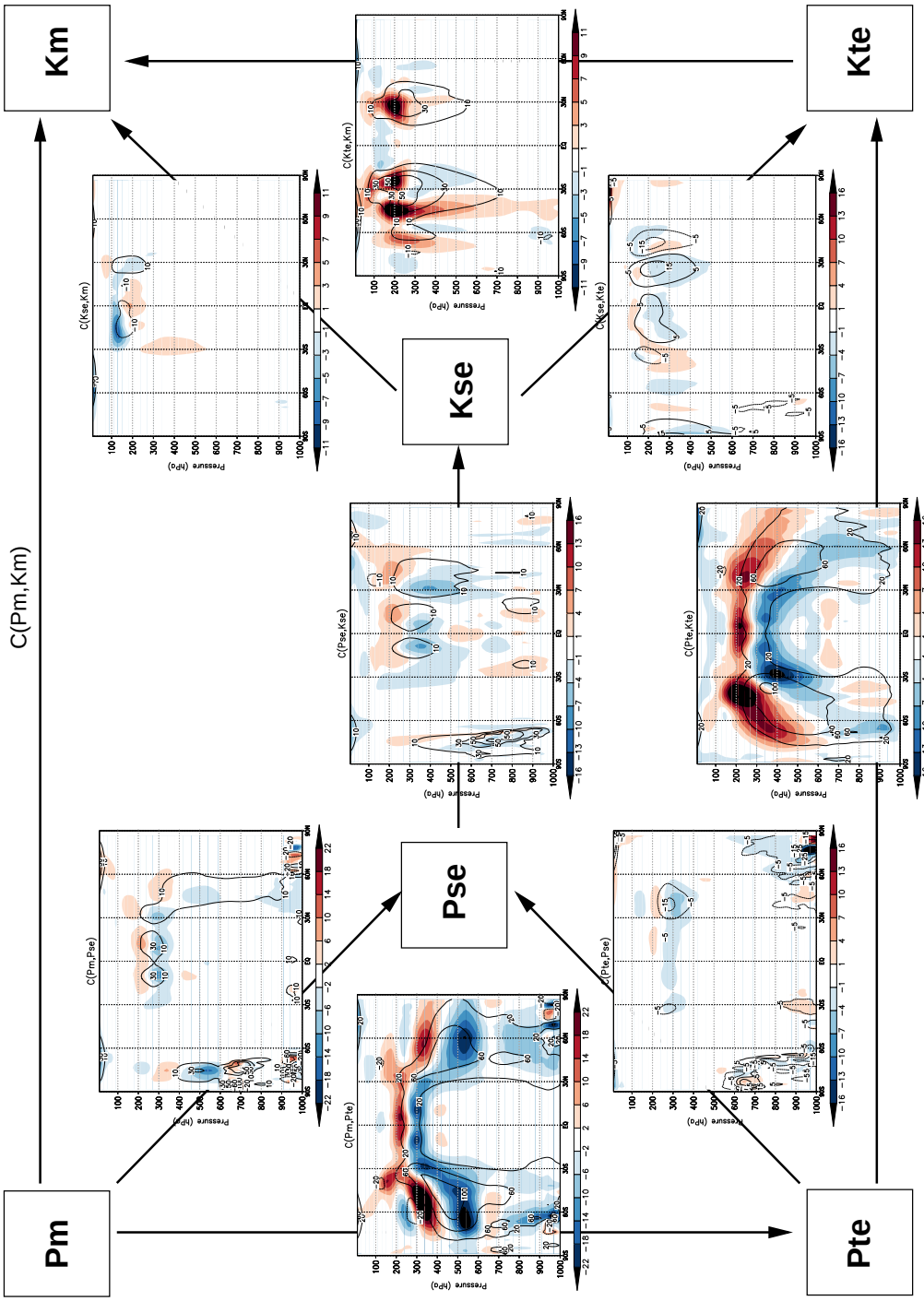

Figure 2.18: Vertical cross sections of the stationary and transient eddy conversion terms ($C(P_m, P_{te})$, $C(P_m, P_{se})$, $C(P_{te}, P_{se})$, $C(P_{te}, K_{te})$, $C(P_{se}, K_{se})$ $C(K_{te}, K_m)$, and $C(K_{te}, K_m)$) for the 1xCO_2 pre-industrial control run (contours), and their 2xCO_2 change (color shaded). Units are 10^{-5} W m^{-2}.

but these do not contribute to the main global energetics response. We deal with these in the next subsection. Regarding K_e, the main upper-strengthening and lower-weakening response is coming from the K_{te} response. The contribution of the change of K_{se} to the K_e-response is much smaller (note the different scale used in the plots of K_{se} and K_{te}).

Regarding the conversion rates (Figure 2.18), it is also very clear that the response to a CO_2-doubling is dominated by the response of the conversions related to the transient eddy reservoirs, i.e, $C(P_m, P_{te})$, $C(P_{te}, K_{te})$, and $C(K_{te}, K_m)$. The other conversion terms show much weaker responses, and the pattern we have observed in $C(P_m, P_e)$, $(C(P_e, K_e)$, and $C(K_e, K_m)$ is clearly a feature of the conversions along the path $P_m \rightarrow P_{te} \rightarrow K_{te} \rightarrow K_m$. Both the energy conversions and their response to a CO_2-doubling are dominated by the terms related to the transient eddy components; the conversions related to the stationary eddy components are small, as well as their change in the 2xCO_2 case.

Summing up, the transient eddy reservoirs and conversion rates clearly dominate the global energetics response. The energetics response we find when considering the stationary and transient eddy components together corresponds to the response of the transient eddy components, whereas the stationary components have a very small contribution. Knowing this, we can return to the previous 4-box LEC, having in mind that the responses of the eddy components reflect mainly the transient eddy responses. This, in order to avoid an unnecessary complexity of our figures. Before proceding with the remaining features of the energetics response, we will disscuss the particular features observed in the reservoir of P_{se}.

The stationary eddy response

There is one feature of the P_{se}-response that, although not related to the main energetics response, stands out and is worth a brief analysis. P_{se} has two symmetric regions of increase near the surface at around 30°N and 30°S, which contribute to the vertical cross-section of P_e in Figure 2.16. Figure 2.19 (above) shows a plot of the change in the integrand of P_{se} (before applying the zonal mean), $(c_p/2)\gamma\langle\beta\rangle\langle T\rangle^{*2}$, at 900 hPa. It shows that the increase region around 30°S is due to an increase in P_{se} over Australia, central-South America and a region over the Eastern Pacific. The increase region around 30°N is related to an increase in P_{se} over the Saharan and the Arabian Deserts. This is clearly related to the 2xCO_2 temperature change in these regions. The 2xCO_2 temperature change at 900 hPa (Fig. 2.19, bottom) shows that the regions that are causing changes in P_{se} correspond to regions where the warming creates a temperature field such that it has stronger deviations from the zonal mean temperature field than their corresponding latitudinal belts. For example, the mean temperature field at 900 hPa in the 1xCO_2 run (not shown here) reveals that the Australian continent has a higher mean temperature than its corresponding zonal-belt. On the contrary, the Eastern Pacific has a lower mean temperature compared to its zonal belt. By doubling CO_2, the Australian continent warms up to 3.5 K and the Eastern Pacific warms about 1-1.5 K. The zonal mean warming at this latitude-belt is around 2 K. Therefore, both deviations from the zonal mean tempera-

ture field are enhanced by the 2xCO$_2$ warming, implying an increase of P_{se} in these regions. The Amazon basin, and the Sahara and Arabian Deserts are also on average warmer than their zonal-belts, and the 2xCO$_2$ warming enhances these contrasts.

The opposite happens in the Atlantic between Greenland and Northern Europe. This region is on average warmer than its latitudinal-belt, causing the largest contribution to P_{se} globally. The 2xCO$_2$ warming pattern reduces this difference in temperature, because (a) the continental

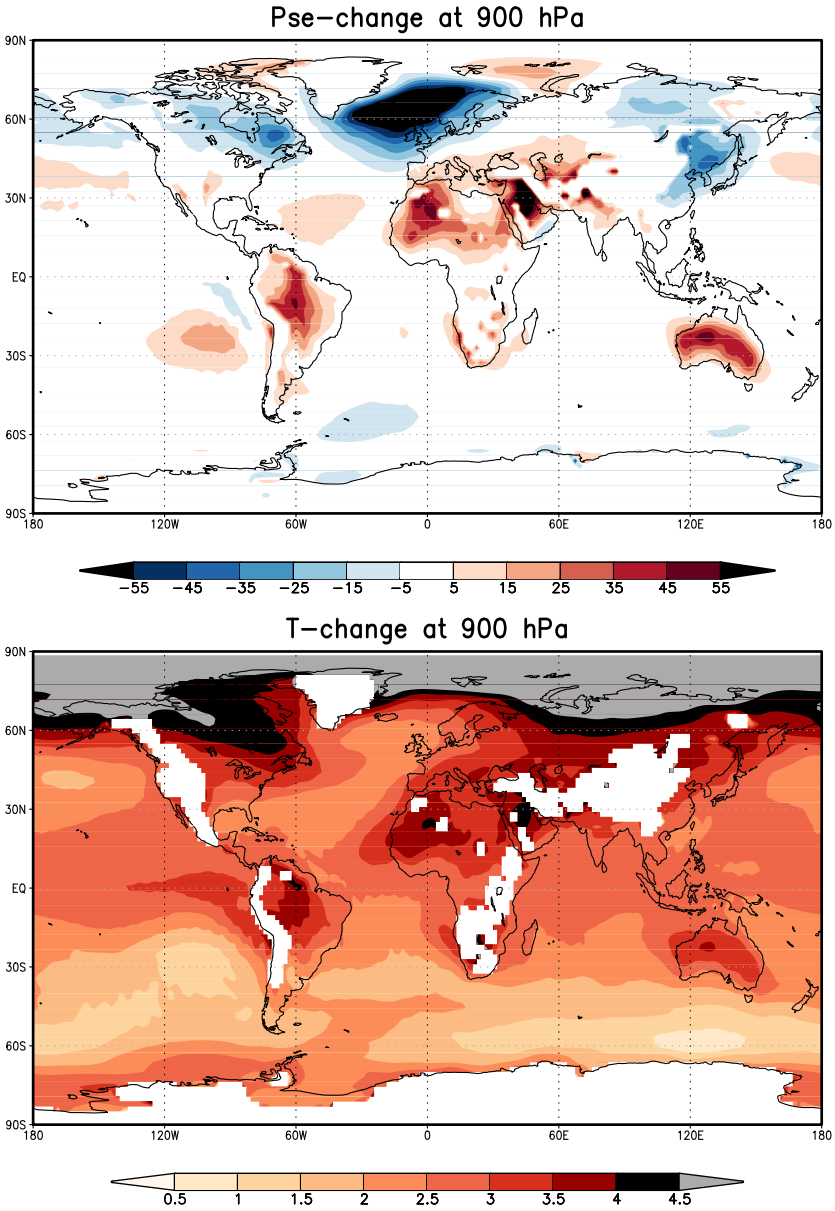

Figure 2.19: P_{se}-change (above) and temperature change (below) at 900 hPa due to CO$_2$ doubling.

warming is stronger, and (b) the weakening of the Atlantic meridional overturning reduces the sea surface temperature in this region (Meehl et al., 2007). This explains the strong decrease in P_{se} in Figure 2.19 around 60°N. These features of the 2xCO_2 warming pattern are not new. Most current climate models predict such a warming pattern (Meehl et al., 2007).

Although these changes in P_{se} stand out and are clearly related to the 2xCO_2 warming, they do not affect the global energetics response of the atmosphere. In order to do so, these changes in P_{se} would also have to cause changes in the conversion rate into K_{se}, $C(P_{se}, K_{se})$. There is indeed a contribution around 30°N and 30°S in this conversion rate, but it is very small. Actually, we expect this conversion to be small in these regions, because in order to convert P_{se} into K_{se}, a good correlation between $\langle\omega\rangle^*$ and $\langle\alpha\rangle^*$ is needed (see Appendixes A and B). Intuitively, this can be seen as rising of relatively warm air and sinking of relatively cold air in the stationary eddies. However, these regions are mostly subtropical deserts where there is relatively warm air, but very little or no rising of air. Therefore, $C(P_{se}, K_{se})$ has a very small contribution from these regions, and the global energetics is not affected much by such features in P_{se}. Regarding the decrease of P_{se} in the North Atlantic region, this does not have any effect on the conversion rate $C(P_{se}, K_{se})$ either. In this case, the only reason we find is that the contribution of $C(P_{se}, K_{se})$ to the total $C(P_e, K_e)$ in this region is so small already that a further reduction in the reservoir of P_{se} makes no difference.

Splitting the atmosphere

Just as with the T31L19 resolution runs, the vertical cross-sections suggest a strengthening response of the LEC in the upper troposphere and a weakening response below. In order to verify this in a more rigorous way, we split the atmosphere at an isobaric surface of 340 hPa and evaluate the LEC terms of each region, plus the corresponding boundary fluxes, calculated according to Appendix A. We use the 340 hPa instead of 350 hPa level because due to the new resolution, this level corresponds to a model-level, which facilitates the computations.

We have computed the LEC-terms for the upper and lower regions (Fig. 2.20) as well as the corresponding changes in the generation, conversion, dissipation rates and boundary fluxes (Fig. 2.21) for the split atmosphere. Overall, we do observe a strengthening of the LEC terms in the upper region and a weakening in the lower region, just as with the lower resolution runs. If we compare Figures 2.6 and 2.8 with Figures 2.21(a) and 2.21(b) respectively, we see a clear consistency, with only one remark: the weakening response of the lower region is less pronounced in the higher resolution runs, but the strengthening response of the upper region has a similar magnitude in both resolutions. This could be due to the differences in the amplitude of the warming pattern. Nevertheless, the overall response is consistent with our conclusions from the low resolution runs. Clearly, the response of G_m is the strongest in both regions, suggesting once more that this term is driving the whole energetics response.

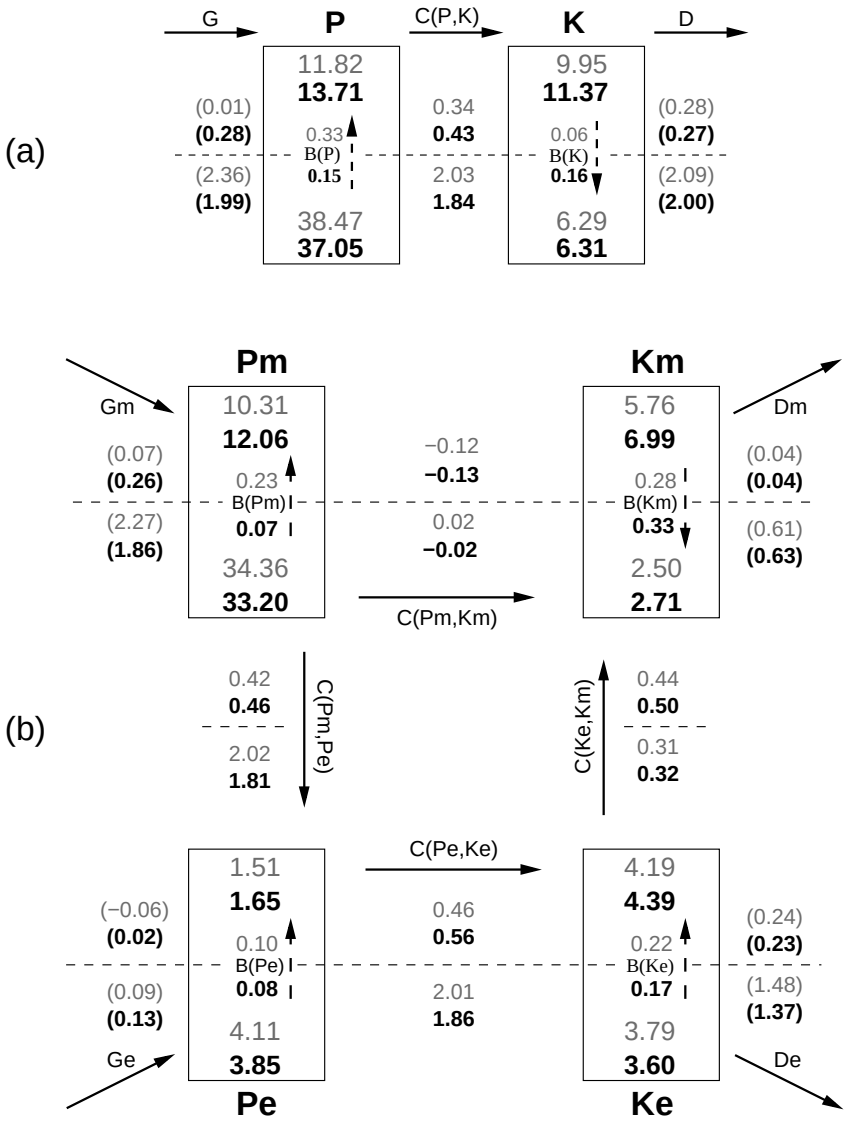

Figure 2.20: (a) 2-box and (b) 4-box diagram of the LEC-terms for the 1xCO2 control run (above, gray) and the 2xCO2 equilibrium run (below, black) with T63L31 resolution, split at 340 hPa (dotted line). Generation and dissipation terms (in parenthesis) are obtained as residuals. Units are 10^5 J m^{-2} for reservoirs and W m^{-2} for conversion, generation and dissipation terms. Arrows indicate the direction corresponding to positive values; negative values imply opposite direction.

Mean static stability

In the analysis of the low resolution experiments, plotting the responses of γ (the inverse mean static stability), and of the vertical profile of P_m (Figures 2.11 and 2.12) revealed that the changes in meridional temperature gradient are driving the increase in P_m in the upper troposphere (due to the tropical, upper-tropospheric warming) and its decrease from the surface up

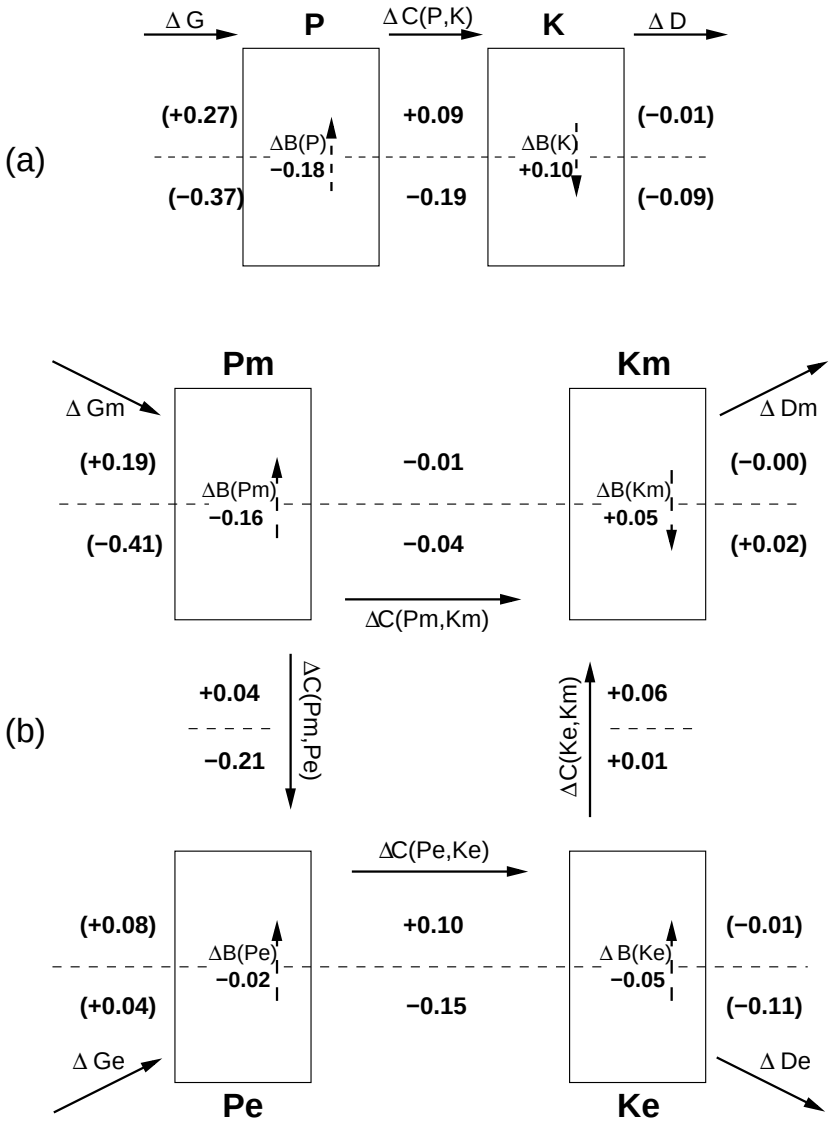

Figure 2.21: (a) 2-box and (b) 4-box diagram of the changes in energy generation, conversion and dissipation rates in the LEC due to CO_2 doubling, evaluated from Figure 2.20. Units are W m^{-2}. Arrows indicate the direction corresponding to positive values; negative values imply opposite direction.

to about 700 hPa (due to the high-latitude surface warming). The decrease of P_m in the "free troposphere", from 700 hPa to 450 hPa was found to be related to the enhancement of mean static stability (decrease in γ). We argued that these changes in P_m, could be the drivers for the dual pattern of strengthening and weakening of the LEC via changes in baroclinicity. Here we will (a) repeat this same analysis but now with the high resolution runs, and (b) discuss why understanding the causes for the changes in G_m, the generation rate of P_m, may be a more

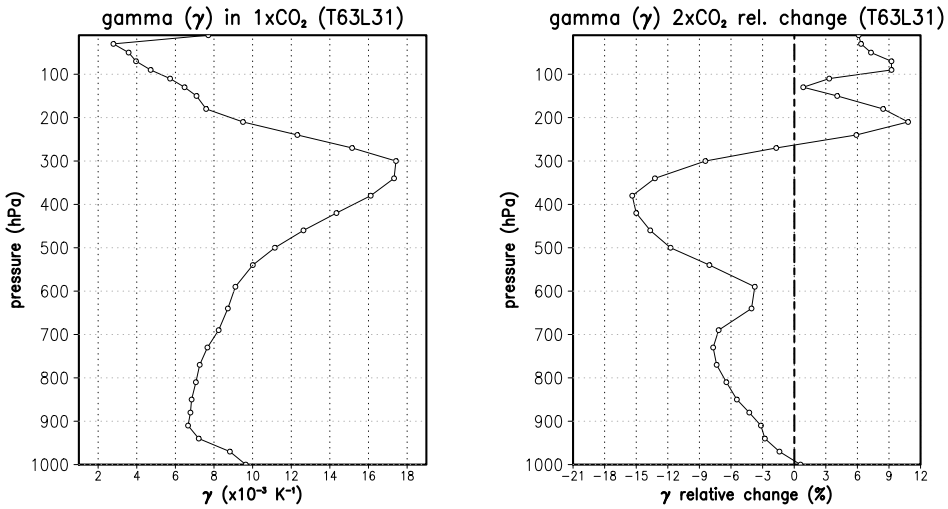

Figure 2.22: Mean vertical profile of gamma (γ) in 1xCO_2 run (left) and its relative change (right) in the 2xCO_2 run (difference divided by the 1xCO_2 value) using T63L31 resolution.

direct way of explaining the dual pattern in the energetics response, instead of doing it through changes in P_m only.

Due to the higher vertical resolution we observe now a smoother profile for γ and its relative change when doubling CO_2 concentrations (Fig. 2.22), compared to the low resolution plots (Fig. 2.11). We also find a more pronounced boundary layer, from the surface up to about 900 hPa, where γ has higher values than above (less stable conditions). The relative change of γ (right panel) shows the same profile as the low resolution runs, but with a smoother profile and some better defined structure in the upper levels, due to the increased vertical resolution. Even the magnitude of the relative change of γ is very similar in both cases. It starts with almost no change at the surface, and decreases with height up to about 700-750 hPa where it reaches a (local) maximum decrease of about 7-8$\%$. Higher up, between 600 and 650 hPa, there is a local minimum in the relative decrease of γ that reaches about 4$\%$ decrease. The maximum decrease of about 15$\%$ is located around 400 hPa, and the zero crossing is near 250 hPa. Above this level, γ increases up to 10-11$\%$. In conclusion, γ exhibits a relative decrease throughout the whole troposphere of the same magnitude and with a very similar profile in both resolutions.

The vertical profile of the relative change of P_m (Figure 2.23) is also very similar to the one obtained with the low resolution runs (Figure 2.12), although the magnitude of the change is slightly smaller. Between roughly 900 hPa and 700 hPa it decreases now by almost 5$\%$; in the low resolution it decreases in this region by about 10$\%$. The relative minimum at about 650 hPa reaches now a slight increase; in the low resolution runs it reaches a decrease of about 5$\%$. In any case, the profile reveals again that the strong decrease in P_m near the surface must be due to changes in horizontal temperature variance, and the decrease of P_m above 600 hPa is clearly driven by the relative decrease of γ, i.e., the increase in global mean static stability.

Above 250 hPa, P_m reaches an increase of about 140% (out of scale in Figure 2.23), which must be related to horizontal temperature variance changes, because the relative changes of γ are never as large.

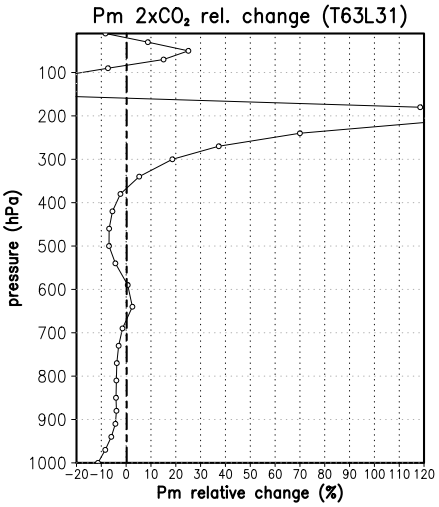

Figure 2.23: Global mean vertical profile of the relative change of P_m in the 2xCO$_2$ run (difference divided by the 1xCO$_2$ value) using T63L31 resolution.

We reach then the same conclusion we obtained for the low resolution experiments. The effects of the changes in static stability and horizontal temperature variance cause the dual pattern of change in P_m, and this response of P_m can, via changes in baroclinic activity, explain qualitatively the dual response in strength of the LEC. Baroclinic activity is what allows us to make a connection between the response of P_m—a reservoir of energy—and the conversion rates $C(P_m, P_e)$ and $C(P_e, K_e)$. P_m can be seen as the energy source for baroclinic instabilities. Therefore, we are assuming that changes in baroclinicity will result from changes in its energy source, which of course makes sense, but we cannot verify this with certainty.

We can also assess this without having to rely upon this assumption regarding changes in baroclinicity and changes in the P_m-reservoir. G_m, the generation rate of P_m is the term that drives the whole LEC (Lorenz, 1955, 1967; Peixoto and Oort, 1974, 1992). Futhermore, in terms of energetic activity, we found that it is also the term which suffers the strongest changes due to CO$_2$ doubling (see subsection 2.2.3 and Section 2.1.3). We can therefore understand the strengthening and weakening of the LEC if we understand why G_m increases in the upper region and decreases below. Unfortunately, we cannot obtain vertical profiles of G_m, which we could use in a similar way as we did with P_m. This is because G_m has been estimated as a residual of the corresponding conversion terms, rather than directly computed from the model output. A full 6-hourly 3D-field of diabatic heating rates, which is not a standard output of the model, would be necessary for a direct calculation of G_m. However, by analysing the expression for G_m (equation (A.6) from Appendix A), we can infer several properties. First of all, the expression for G_m is very similar to the expression for P_m. It is also proportional to γ, so changes in mean static stability could affect G_m in a similar way as they affect P_m. The difference with P_m is that instead of being proportional to $[\langle T\rangle]''[\langle T\rangle]''$, the horizontal variance of temperature, it is proportional to $[\langle T\rangle]''[\langle Q\rangle]''$, the "correlation" between deviations of temperature and diabatic heating. In other words, G_m has positive contributions from relatively warm latitudes that have net diabatic heating, or from relatively cold latitudes that have net diabatic cooling. Negative contributions would imply relatively warm latitudes with net diabatic cooling, or relatively cold latitudes with net diabatic heating. We know that on average, the relatively warm latitudes—

the low latitudes—have an excess of diabatic heating, while the relatively cold latitudes—the high latitudes—have an excess of diabatic cooling (e.g., Peixoto and Oort, 1992). Hence, G_m is by far positive, because $[\langle T\rangle]''$ and $[\langle Q\rangle]''$ are strongly correlated. This is not the case of G_e, for example. In terms of deviations from the time and zonal-means, there is no such strong correlation between $\langle T\rangle^*$ and $\langle Q\rangle^*$, or between T' and Q'. Most of the processes leading to the generation of P_e cancel each other, such that globally, this term ends up being very close to zero, or even slightly negative (Lorenz, 1955; Romanski, 2009).

The fact that $[\langle T\rangle]''$ and $[\langle Q\rangle]''$ are so highly correlated implies that G_m should have a distribution similar to P_m. For example, the vertical profile of G_m should have characteristics very similar to those of P_m, although with different units. We do not find any reason for this high correlation to change significatively in a 2xCO_2 climate. The pattern of change of G_m must be very similar to the pattern of change of P_m due to CO_2-doubling. This means that we can extend our analysis regarding P_m to G_m: having in mind that G_m should behave in a very similar way to P_m, we can conclude that the increase in G_m in the upper region is related to the strong increase in horizontal temperature variance due to the tropical upper-tropospheric warming. This assumes that in this upper region, the correlation between $[\langle T\rangle]''$ and $[\langle Q\rangle]''$ becomes stronger due to the larger meridional temperature gradient. The decrease of G_m in the lower region is related to a combination of the increased mean static stability due to the upper tropospheric warming, and the decreased meridional temperature gradient due to the high-latitude surface warming, which should decrease the correlation between $[\langle T\rangle]''$ and $[\langle Q\rangle]''$ near the surface. This dual response of G_m drives then the strengthening of the LEC in the upper region and the weakening in the lower region.

2.2.4 Conclusions and discussion

In relation to the two main objectives of this section, we now present the corresponding conclusions:

- The energetics response to a CO_2-doubling of the higher resolution runs is consistent with the results obtained with the lower resolution runs. The amplitude of the response is slightly smaller in the higher resolution runs. This is not surprising because the warming pattern has also a smaller amplitude. Therefore, the conclusions regarding the equilibrium 2xCO_2-response from Section 2.1.4 are also valid for the higher resolution runs. Further, we can add that the dual role of the warming pattern, which we know affects P_m due to changes in horizontal temperature variance and mean static stability, should also affect G_m in a similar way. This explains, without considering other conceptual models, how the warming pattern can cause the whole energetics response, given that changes in G_m drive the changes in strength of the LEC.

- The additional transient and stationary eddy decomposition of the LEC revealed that the main energetics response is determined by the response of the transient eddy reservoirs

P_{te} and K_{te} and by the corresponding energy conversion rates ($C(P_m, P_{te})$, $C(P_{te}, K_{te})$ and $C(K_{te}, K_m)$). The response of the stationary eddy reservoirs P_{se} and K_{se}, and of their corresponding energy conversion terms $C(P_m, P_{se})$, $C(P_{te}, P_{se})$, $C(P_{se}, K_{se})$, $C(K_{se}, K_{te})$ and $C(K_{se}, K_m)$ is very small compared to the transient component response. The response of P_{se} reflects some features due to the regional warming pattern over several subtropical deserts, but this does not involve or influence at all the main energetics response. We argue that the main energetics response obtained without the transient and stationary decomposition corresponds to the transient eddy response. In order to avoid adding too much complexity to our figures, we will not carry out the full transient and stationary decomposition in the remaining chapter. Instead, we will stay with the standard 4-box LEC, but now having in mind that the main 2xCO_2-response is related to changes in transient, and not stationary, eddy activity.

2.3 Conclusions

In this chapter we investigated the global energetics response of the atmosphere in the coupled ECHAM5/MPI-OM atmosphere-ocean model due to higher CO_2 concentrations. We do this by diagnosing changes in the Lorenz Energy Cycle (LEC) (Lorenz, 1955).

Using a coarse resolution (T31L19 for the atmosphere and GR30L40 for the ocean) we examined two 50-member ensembles, each consisting of 10-year transient experiments with 3% CO_2-increase per year, and one equilibrium 2xCO_2 run, comparing these to a pre-industrial 1xCO_2 experiment. Then, we used a higher resolution version of the same coupled model (T63L31 for the atmosphere and GR15L40 for the ocean) to verify the equilibrium 2xCO_2 response of the coarse resolution runs, and to perform an additional transient and stationary eddy decomposition of the LEC.

We obtained three main conclusions:

- Globally, the LEC weakens with higher CO_2 concentrations. There is less conversion of available potential energy into kinetic energy. For a doubling of CO_2, this reduction is of approximately 7% and of 4% in the coarse and higher resolutions, respectively. By splitting the atmosphere at an isobaric level near 350 hPa, we find that there is a consistent pattern of strengthening of the LEC in the upper region and a weakening below. This dual response is related to the zonal-mean warming pattern that consists of a maximum warming in the tropical upper-troposphere and at high latitudes near the surface. Changes in horizontal temperature variance cause an increase of P_m in the upper troposphere and a decrease near the surface. In the free troposphere (roughly between 700 and 400 hPa) P_m decreases due to changes in mean static stability caused by the upper tropospheric warming. These changes in P_m can explain qualitatively, via changes in baroclinic activity, the strengthening of the whole LEC in the upper region—accompanied by a strong increase in K_m—and its weakening below—characterized by

a decrease in the eddy reservoirs and their conversion terms. Alternatively, one can understand this dual pattern in strength of the LEC from the point of view of G_m, whose changes clearly drive the changes in strength of the whole LEC. G_m behaves in a very similar way to P_m, so the warming pattern affects it accordingly. This provides a clear link between the warming pattern and the changes in strength of the LEC without having to include assumptions about baroclinic activity.

This conclusion applies to both resolutions of the coupled model. The few differences that exist between the two resolutions concern mainly the amplitude of the response, which follows from the difference in the warming pattern amplitude.

- Due to the weaker warming in the transient (coarse resolution) experiments, the transient response to increasing CO_2 concentrations is less pronounced than the equilibrium 2xCO_2 response, but consistent with it. The transient response is less north-south symmetric than the equilibrium response, mainly because of the stronger north-south assymetry in the warming pattern of the transient runs. The Northern Hemisphere warms much faster than the Southern Hemisphere, likely due to a coupled feedback process that tends to maintain the latitudinal temperature gradient over the Southern Ocean (Fyfe and Saenko, 2006; von Storch, 2008).

- The decomposition of the eddy reservoirs into transient and stationary eddies show that the energetics response we describe above affects mainly the transient and not the stationary eddy components. In order not to increase the complexity of the LEC in terms of the number of terms to consider, we will continue with the 4-box LEC (without the transient and stationary eddy decomposition), but having now in mind that the main energetics response to higher CO_2 concentrations involves mainly the transient eddy components and not the stationary ones.

Chapter 3

Understanding the energetics response: effects of different warming patterns

3.1 Introduction

The previous chapter describes how the energetics of the atmosphere, in terms of the Lorenz Energy Cycle (LEC), respond to higher CO_2 concentrations in the coupled atmosphere-ocean model ECHAM5/MPI-OM. We found that the main response is closely related to the zonal mean warming pattern that has two main features: a tropical upper-tropospheric warming, and a high-latitude surface warming. This relationship holds if one assumes that changes in horizontal temperature variance and in mean static stability can drive the strengthening and the weakening of the LEC in the atmosphere. We came to this conclusion because we found two opposite responses that are spatially separated: the strengthening of the LEC in the upper troposphere, and its weakening below. One could naively interpret this as a separation of the effects of the two main features of the warming pattern, because these features show up in the same separate regions where the net effects are found (the tropical warming in the upper troposphere, where the LEC strengthens, and the high-latitude warming below, where the LEC weakens). However, this is not necessarily true because the effects of each feature of the warming pattern may extend beyond the region where the warming takes place. For example, the upper-tropospheric warming enhances the mean static stability throughout the lower and middle troposphere, but not in the upper troposphere. Furthermore, the high-latitude surface warming reduces the pole to equator temperature gradient near the surface, but the consequences of this in terms of changes in baroclinic activity could extend throughout most of the extratropical troposphere. Hence, we only made a qualitative connection between the warming pattern features and the energetics response.

The separation of the energetics response that we carried out in Chapter 2 does not imply a separation of the effects of the two main features of the warming pattern. Using a global climate model, the most direct way of determining the effects of each feature of the warming pattern is by imposing each of these features to the coupled model separately, and then evaluating their response. By taking this approach we expect to understand in more detail how the warming pattern causes the energetics response to doubling of CO_2 described in the previous chapter.

We carry out experiments in which we artificially produce specific warming patterns by using spectral nudging—instead of increasing CO_2 concentrations—and then analyse their energetics response. These experiments are not realistic in the sense that the imposed warming patterns are not a *natural response* of the system. The natural response of the atmosphere to a CO_2-doubling of the temperature field results from a complex combination of processes and feedbacks, and consists, according to our coupled model (and to most climate models), of a tropical upper-tropospheric and a high-latitude surface warming. In order to simulate these two features of the $2xCO_2$ warming pattern separately, we need to include in each experiment different *artificial* diabatic heating and/or cooling terms. Using such a complex and realistic coupled model as we do, this is the only way to achieve a steady state with such warming patterns different from the "natural" one. However, the fact that the warming patterns we aim at are part of the "natural" warming pattern facilitates this task. Furthermore, by showing that the responses of these separate warming patterns combine linearly to produce the responses of the full warming pattern, it follows that the separate responses are a valid and useful way of understanding the combined (and intrinsic) $2xCO_2$ response.

To our knowledge, there have been no previous attempts to study the atmospheric response due to specific warming patterns in terms of the global energetics. Nevertheless, several studies are closely related. O'Gorman and Schneider (2008) use an idealized moist general circulation model to which they apply two radiative forcings that simulate (a) the total effect of higher greenhouse gas concentrations or (b) changes in meridional temperature gradient. They find that eddy kinetic energy in mid-latitude baroclinic zones scales approximately linearly with available potential energy, and can therefore be related to changes in the thermal structure of the atmosphere. This is consistent with our results from the previous chapter, but it does not include the response of the energy conversion rates. In another study, Lim and Simmonds (2009) conclude that the tropical upper tropospheric warming is the main cause for the reduction in frequency and depth of the Southern Hemisphere winter extratropical cyclones, due to changes in static stability. They find this by using an atmospheric general circulation model with a relatively coarse resolution to which they introduce idealized warm anomalies that mimic specific warming patterns. Other studies (e.g., Geng and Sugi, 2003; Bengtsson et al., 2009; Sienz et al., 2010) analyse in detail the responses of extratropical cyclones to warmer climates, but without separating the different features of the warming pattern as we or Lim and Simmonds (2009) do. Furthermore, although the behavior of extratropical cyclones is closely related to the energetics response, it is only one specific feature of it (mainly related to the eddy kinetic energy reservoir). We do not aim at studying specific events in detail here, but rather to obtain a general view of the global energetics response. This could in turn offer further fundamental support to previous (and future) studies that deal with the response of extratropical cyclones.

In the following section we describe the model runs we use and the temperature nudging method we apply in order to produce the specific warming patterns. Section 3.3 describes the energetic responses of the forced experiments, followed by the last section, where we discuss the results and present the main conclusions of this chapter.

3.2 Method

3.2.1 Model and experiments

For this chapter we have carried out 4 integrations with the coupled atmosphere-ocean ECHAM5/MPI-OM general circulation model developed at the MPI for Meteorology in Hamburg. The atmosphere component is ECHAM5.4.01 (Roeckner et al., 2003) with T63L31 resolution ($\approx 1.875^\circ \times 1.875^\circ$ and 31 vertical levels), coupled —without flux corrections— via the coupler OASIS3 (Valcke et al., 2004) to the ocean component, MPI-OM version 1.3.1 (Marsland et al., 2003), running with GR15L40 resolution ($\approx 1.5^\circ \times 1.5^\circ$ and 40 vertical levels). Therefore, both components of the coupled model we use here are newer versions of the ones used in Section 2.2. CO_2 concentrations are fixed to preindustrial levels (280 ppm) in all integrations. They differ only in the forcing applied to the temperature field, achieved by means of spectral nudging (see subsection 3.2.2). The experiments are:

- **CTRL**: The control integration with no forcing (comparable to the 1xCO_2 runs from the previous chapter).
- **FULL**: An integration with a forcing such as to produce a "2xCO_2-like" zonal-mean warming pattern according to the simulated pattern from Section 2.2. This includes the tropical upper-tropospheric warming, and the high-latitude surface warming. This run is expected to reproduce the 2xCO_2 energetics response as in Chapter 2, serving as a validation of our nudging method.
- **UP**: An integration with a forcing such as to produce a zonal-mean warming pattern where only the tropical upper-tropospheric warming is present.
- **SFC**: An integration with a forcing such as to produce a zonal-mean warming pattern where only the high-latitude surface warming is present.

All experiments start with a spin up run (see subsection 3.2.3) and are followed by a 50-year integration with equilibrated temperature field. This 50-year period of each experiment is analysed below. The aim when applying the temperature-nudging to the model is to reach a certain time and zonal-mean warming pattern relative to the control run (CTRL), as indicated above. Therefore, a plot of such a warming pattern for each of the forced runs characterizes their forcing. Figure 3.1 shows the time and zonal-mean warming patterns of the three forced runs, FULL (upper panel), UP (lower left panel) and SFC (lower right panel). In the three plots the time and zonal mean temperature field of CTRL is shown as contour lines. Further details about these integrations are given in subsection 3.2.3.

3.2.2 Spectral nudging

The forcing we apply in order to produce the warming patterns in the different model integrations is achieved by using a nudging module developed for the atmospheric model ECHAM5.

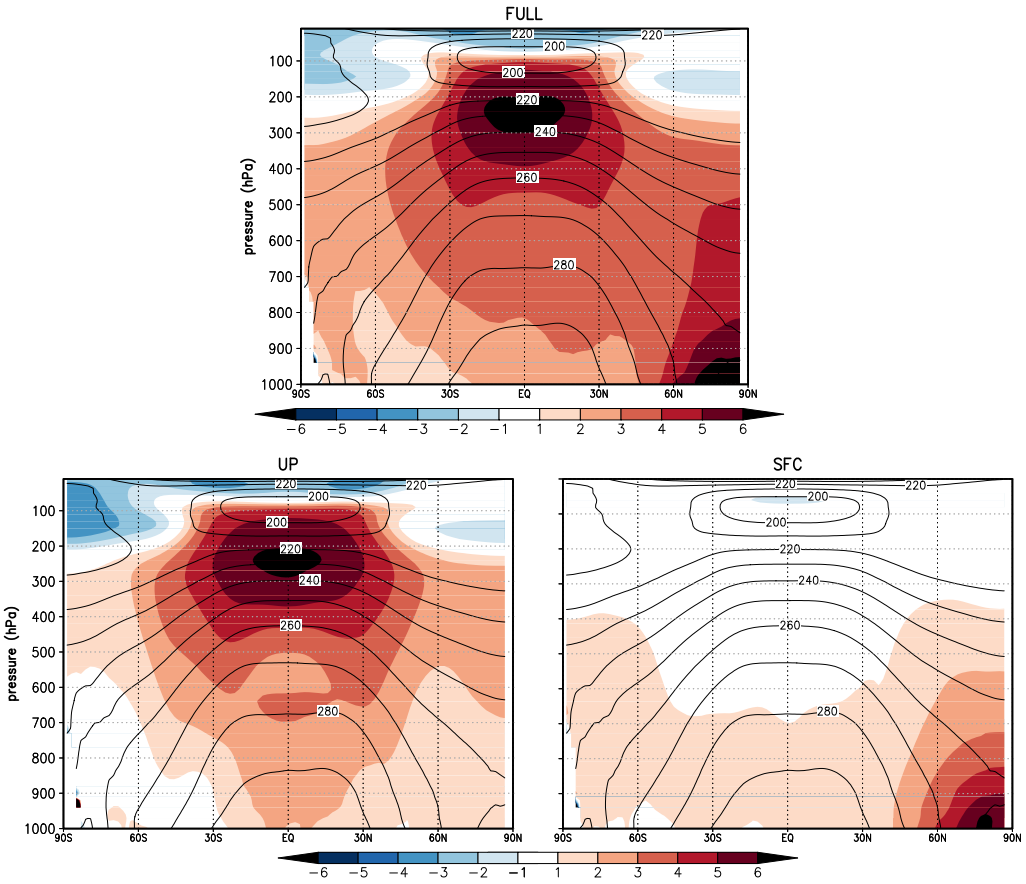

Figure 3.1: Time and zonal-mean temperature change (color shaded) in FULL (upper panel), UP (below, left panel) and in SFC (below, right panel) relative to CTRL (contours).

This module is based on the methodology used by Krishnamurti et al. (1991). It uses newtonian relaxation of temperature, vorticity, divergence, surface pressure and sea surface temperature (SST), and is originally intended for adjusting the model output to observations. There is one nudging coefficient assigned to each variable, which determines the relative weight given to the observations and to the model on each timestep. Krishnamurti et al. (1991) apply the nudging according to

$$X(t+dt) = \frac{X_1(t+dt) + 2NdtX_2(t+dt)}{1+2Ndt}, \tag{3.1}$$

where $X_1(t+dt)$ is the predicted value of $X(t+dt)$ prior to nudging, and $X_2(t+dt)$ is the future value towards which the nudging is aimed at. N is the nudging coefficient. This is implemented in the ECHAM5 nudging module with a slight modification of the nudging coefficient (I. Kirchner, personal communication):

$$X(t+dt) = AX_1(t+dt) + BX_2(t+dt), \tag{3.2}$$

where

$$A = \frac{1}{1 - 2Ndt} \qquad \text{and} \qquad B = \frac{2Ndt}{1 - 2Ndt}. \tag{3.3}$$

The inverse of the nudging coefficient N reflects the relaxation time. Typical values used to match reanalysis data correspond to relaxation times of 6 to 48 hours, depending on the considered variable. Additionally, because the nudging is done in spectral mode, it is also possible to nudge only specific wave numbers.

3.2.3 Procedure for temperature nudging

In this study we are not interested in matching observations, but rather in producing a specific atmospheric warming pattern. Therefore, the way we use the nudging module is slightly different to the "standard" way of nudging. Before describing the steps carried out to produce the temperature-nudged experiments, we will describe the main differences of our method with the "standard" one:

- Only the temperature field needs to be nudged. The idea is to introduce a diabatic forcing consistent with a chosen warming pattern, and at the same time to allow the atmospheric dynamics to freely adjust to this forcing. Therefore, the nudging coefficients of divergence, vorticity and surface fields are set to zero. From here on, "the nudging coefficient" refers to "the temperature nudging coefficient".

- We nudge to a constant temperature field, as opposed to the usual case where time varying observations are used. This implies that the nudging coefficient must be small enough not to constrain the natural variability of the model. After several tests, we found that a nudging coefficient of $N = 0.01 \times 10^{-5}$ s^{-1} (relaxation time of ≈ 116 days) is small enough not to constrain the natural variability in the model. We verified (not shown here) that the variability from daily to inter-annual timescales is not affected by the nudging procedure when we use such a long relaxation time and nudge only zonal wave numbers 0 and 1 (see below).

- The forcing we want to apply is a zonally symmetric temperature field. Therefore, we must only nudge wave number 0 (global mean) and wave number 1 (zonal mean). Higher zonal wave numbers are not nudged. This also avoids unnecessary constraining of higher frequency variability in the model.

The whole nudging procedure is based on the 2xCO_2 warming pattern obtained with the T63L31 resolution in the previous chapter (Fig. 2.13). The temperature fields that we use as nudging fields are obtained by adding a warming pattern to the time and zonal-mean temperature field of CTRL. The warming pattern we add is constructed from the 2xCO_2 warming pattern obtained from the last 50 years of the 1%/year CO_2-increase experiment to doubling,

described in Section 2.2.2. For example, the nudging field for FULL would be just the zonal-mean temperature field of CTRL plus the 2xCO_2 warming pattern. However, such a temperature nudging-field does not produce enough warming because of the small nudging coefficient. In order to obtain the desired warming pattern, we must add a "modified" 2xCO_2 warming pattern to the CTRL temperature field. This modification is an amplification (or reduction) of the warming, level by level. That is, we multiply the warming pattern by "amplification coefficients", which are numbers assigned to each vertical level. The values of these amplification coefficients are determined by trial and error, until the desired time and zonal-mean warming pattern is achieved (and in equilibrium) for at least 50 years.

For the FULL integration, we obtained the warming pattern (Fig. 3.1, above) using an amplification coefficient of 5.9 at the lowest level, then decreasing this number up to zero at 250 hPa, and increasing it again up to 3.5 at the upper most level (10 hPa). The remaining two nudged integrations (UP and SFC) are obtained in the same way, but using different amplification coefficients. For UP we use an amplification coefficient of -3.8 at the lowest level, 8.1 at 250 hPa, and 3.0 at 10 hPa in order to obtain the warming pattern in the lower left panel of Figure 3.1. For SFC, we used 11.2 at the lowest level, -7.5 at 250 hPa and 0.0 at 10 hPa, obtaining then the warming pattern in the lower right panel of Figure 3.1. Note that we use negative values in certain regions, which imply a cooling forcing. This is due to the strong link between the two features of the warming pattern. It is well known (Held, 1993; Held and Soden, 2000; Bengtsson and Hodges, 2009; Sherwood et al., 2010) that the tropical upper-tropospheric warming is an amplification of the surface warming due to deep convection. Therefore, in order to warm only the lower levels, we must apply a strong cooling forcing in the upper troposphere. Similarly, warming the upper troposphere tends to warm the lower levels of the atmosphere, but not as strongly as the previous case. Therefore, the cooling forcing we apply at the surface in UP (-3.8) is not as strong as the cooling forcing we apply at 250 hPa in SRFWRM (-7.5). At the end, the amplification coefficients result from a large number of integrations with different values to match the warming pattern.

Note that these coefficients, which amplify differentially the warming pattern in the temperature nudging field, are the ones that allow us to achieve the *artificial* warming patterns that are different from the *natural* warming pattern of the system, despite the small values we must use for the nudging coefficients. As we noted in the introduction of this chapter, the fact that the warming patterns we aim at are derived from the natural 2xCO_2-warming pattern makes it easier to obtain them with the help of these amplification coefficients. Obtaining other, much different warming patterns, like for example a completely homogeneous one, would be almost impossible because the model reacts with strong inhomogeneities. The "tuning" process of the amplification coefficients for such a warming pattern would be far too complicated and time consuming.

The annual time series of the complete integration time of the four experiments (Fig. 3.2) give a good idea of the temporal evolution of the different experiments. We show time series of global mean surface temperature and global mean temperature at 250 hPa because these two

quantities are closely related to the two main features of the $2xCO_2$ warming pattern that we want to study—the tropical upper-tropospheric and the high-latitude surface warmings. The plots in Figure 3.1 are computed from the last 50 years of each integration (thick lines in Fig. 3.2). The largest trend in these periods of the 4 experiments is found in t250 of CTRL and SFC, estimated by simple linear regression to be 0.003 K/year, i.e., an increase of only 0.15 K in 50 years. Such a trend is small enough so that these 50-year periods can be considered as in equilibrium.

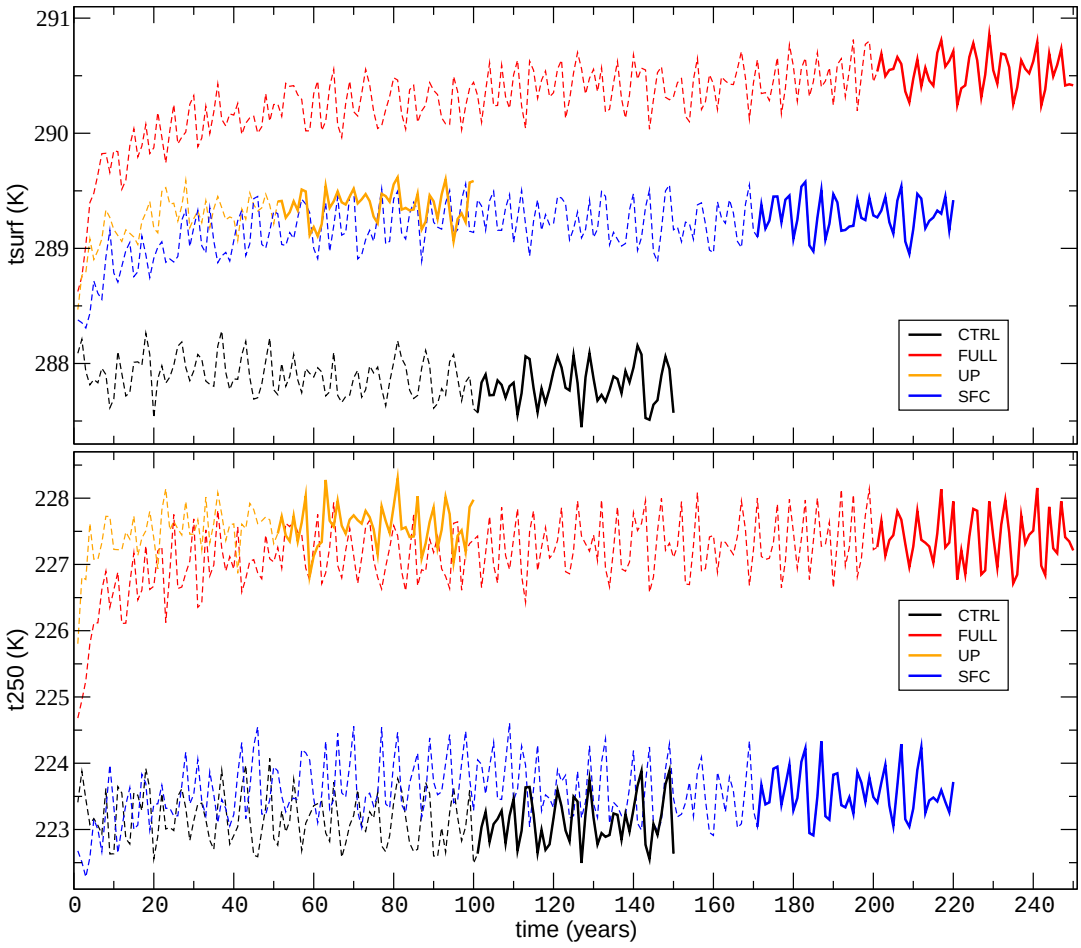

Figure 3.2: Annual time-series of global mean surface temperature (above) and global mean temperature at 250 hPa of the CTRL, FULL, UP and SFC experiments. Thick lines correspond to the 50 years used for the computations in this chapter, in which the desired steady state was reached. Dashed lines correspond to the period prior to reaching the desired warming pattern and/or when the atmosphere is not yet in equilibrium.

3.3 Energetics response of the temperature-nudged experiments

In this section we analyse the energetics response of the three temperature-nudged experiments, FULL, UP and SFC with respect to CTRL. Due to the large number of plots and figures related to this section, some plots are included as supplementary material in Appendix D.

3.3.1 2xCO$_2$-like warming pattern (FULL)

The last 50 years of the FULL experiment provide a zonal-mean warming pattern that is very similar to the 2xCO$_2$ one. Figure 3.3 reveals how similar the warming patterns of FULL and the 2xCO$_2$ experiment are. The only differences in the troposphere between the two warming patterns are located near the surface at high latitudes. North of 60°N and below 700 hPa, FULL is slightly warmer, but with less than 1 K difference. The bias south of 60°S has opposite sign, is slightly larger in amplitude near to the surface, but is restricted to the region below 900 hPa. Applying a stronger temperature nudging could decrease the bias in the Southern Hemisphere, but would increase it in the Northern Hemisphere, unless we use latitude-dependent amplification coefficients (see Section 3.2.3). Anyway, these differences are not large enough to justify this additional complication.

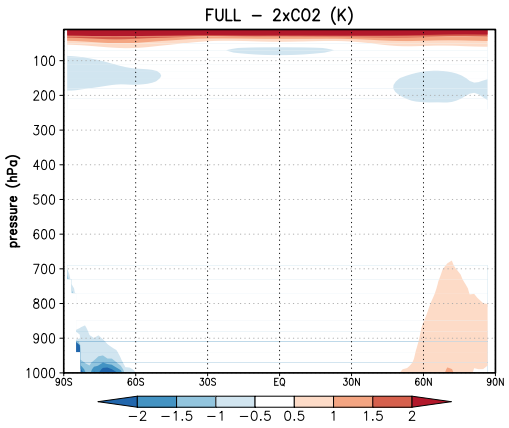

Figure 3.3: Difference in the zonal-mean warming patterns of FULL and 2xCO$_2$, in K (upper panel of Figure 3.1 minus Figure 2.13). Positive values indicate stronger warming (or weaker cooling) in FULL compared to the 2xCO$_2$ case.

There is also a difference in the upper levels between the two warming patterns. The stratospheric cooling of the 2xCO$_2$ run is not as strong in FULL. This is not a serious problem for our study. We have not invested much effort in trying to match this feature of the 2xCO$_2$ warming pattern because (a), our study focuses in the troposphere; (b), the model does not have enough vertical resolution in the stratosphere in order to describe detailed processes there; and (c), because trying to do this would introduce an unnecessary complication to the ”tuning” of the nudging procedure.

We consider FULL’s warming pattern sufficiently similar to the 2xCO$_2$ warming pattern so that we can use it as our ”2xCO$_2$-like” integration. With FULL we want to verify if the 2xCO$_2$ energetics response from Chapter 2 can be reproduced by adding a diabatic forcing to the atmospheric component of the coupled model—via temperature-nudging—towards the 2xCO$_2$ zonal-mean warming pattern, instead of increasing CO$_2$ concentrations. If this is possible, we can use this temperature-nudging method to investigate the effect of different warming

patterns with confidence that the results will have physical meaning, even though they might not represent realistic situations (such warming patterns may not show up naturally in the Earth's atmosphere). Nevertheless, they can be very useful in order to understand the dynamical effects of the $2xCO_2$ warming pattern.

Lorenz Energy Cycle response

We analyse here the energetics response of FULL relative to CTRL in terms of changes in the Lorenz Energy Cycle (LEC), in the same way we did it for the $2xCO_2$ energetics response in Section 2.2. We use the same methodology, computations and notation as in Chapter 2. Here we do not decompose the eddy components into transient and stationary eddies. Instead, we consider them together, having in mind that the main $2xCO_2$ energetics response is given by the transient eddy components.

Comparing the LEC values in Figure 3.4 with the ones in Figure 2.14 reveals a strong similarity between the CTRL experiment and the $1xCO_2$ control run from Section 2.2, as well as between the FULL experiment and the $2xCO_2$ equilibrium run. The first similarity is expected, since both runs have the same external forcings and use similar versions of the same coupled model. The second similarity is a first indication that the energetics response of doubling CO_2

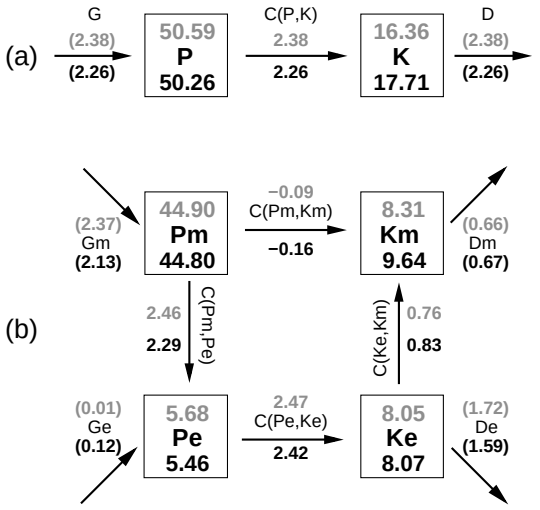

Figure 3.4: (a) 2-box and (b) 4-box diagram of the LEC-terms for CTRL (top line, gray) and FULL (bottom line, black). Generation and dissipation terms (in parenthesis) are obtained as residuals. Units are 10^5 J m^{-2} for reservoirs and W m^{-2} for conversion, generation and dissipation terms. Arrows indicate the direction corresponding to positive values; negative values imply opposite direction.

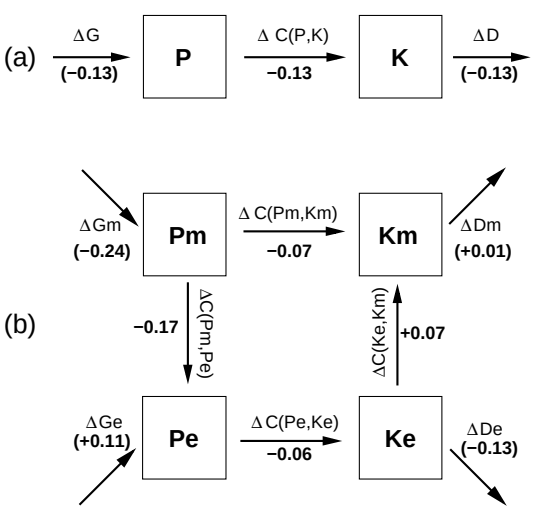

Figure 3.5: (a) 2-box and (b) 4-box diagram of the changes in energy generation, conversion, and dissipation rates in the LEC for the FULL experiment, evaluated from Figure 3.4. Units are W m^{-2}. Arrows indicate the direction corresponding to positive values; negative values imply opposite direction.

concentrations can be reproduced with our temperature-nudging method. The largest difference between two corresponding generation terms is of 0.02 W m^{-2} in $C(P_m, P_e)$, in both pairs of experiments (CTRL and 1xCO_2, and FULL and 2xCO_2). That is a relative difference of less than 1%. The reservoirs differ slightly more, but still, their largest relative difference is of 1.2% (in P_e). Furthermore, it is the energy conversion rates that best describe the energetic activity of the atmosphere, and not the reservoirs.

Of course, if the two integrations (CTRL and FULL) are very similar in terms of the LEC to the previous 1xCO_2 and 2xCO_2 integrations, the energetic response due to the warming of FULL relative to CTRL (Fig. 3.5) will be also very similar to the one due to a CO_2 doubling. The overall weakening of the cycle in FULL is slightly stronger, of -0.12 W m^{-2}, compared to -0.10 W m^{-2} due to CO_2-doubling (Fig. 2.15a). That is the largest difference we can find. Clearly, in both cases the global LEC-response is the same.

Vertical cross-sections

We expect that also the vertical cross-sections of the changes in each LEC-term in FULL are similar to the 2xCO_2 ones. Clearly, there is no important difference between these vertical cross-sections (Fig. 3.6) and the ones corresponding to the 2xCO_2 case (Fig. 2.16). Every LEC-term shows the same patterns of change when increasing the temperature by the nudging method, or when doubling CO_2 concentrations. Along the path $P_m \rightarrow P_e \rightarrow K_e \rightarrow K_m$ we find the same patterns of increase in the upper troposphere and decrease below, just as in the 2xCO_2 case. Even the two symmetric regions where P_e increases around 30°N and 30°S, which correspond to changes in P_{se} due to specific regional warming patterns (see Section 2.2.3), are also present here.

In fact, the similarities we have found until here between the FULL energetics response and the 2xCO_2 energetics response in terms of the global LEC and the vertical cross-sections could be enough to "validate" the temperature-nudging method we use here. However, we want to compare the other temperature-nudged experiments (UP and SFC) with this one (FULL) because these three runs are fully consistent in terms of model version and setup. The 2xCO_2 run was carried out with an older version of the coupled model. Therefore, and for the sake of completeness we will also analyse the split-LEC and the changes related to the mean static stability, as we did with the 2xCO_2 run in Section 2.2.

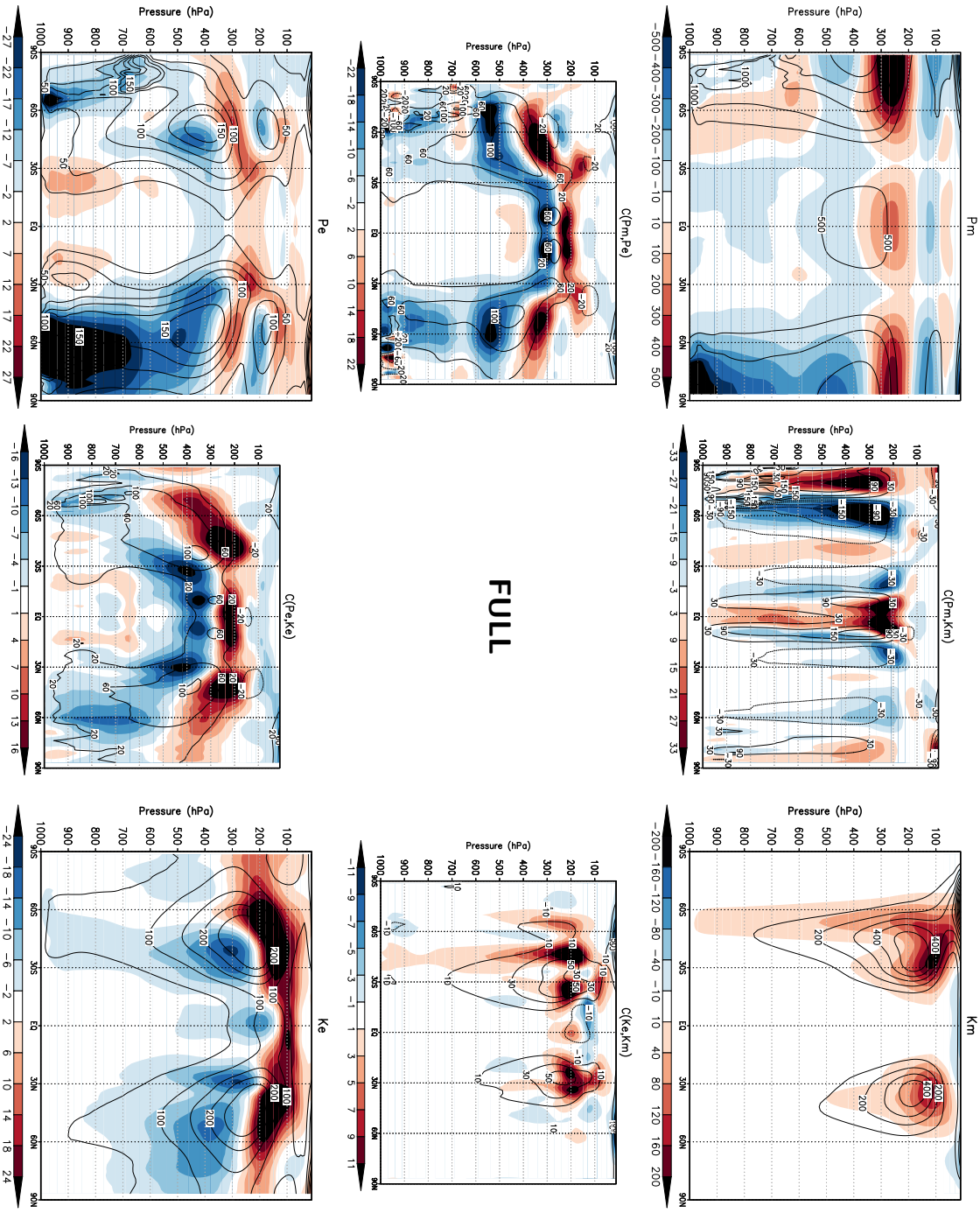

Figure 3.6: Vertical cross sections of the 4-box LEC terms for the CTRL integration (contours), and their change in FULL (color shaded). Counterclockwise, starting from the upper left: P_m, $C(P_m, P_e)$, P_e, $C(P_e, K_e)$, K_e, $C(K_e, K_m)$, K_m, and $C(P_m, K_m)$. Units are J Kg^{-1} for reservoirs, and $\times 10^{-5}$ W m^{-2} for conversion terms.

Splitting the atmosphere

Following the same steps as with the 2xCO_2 analysis, we now split the atmosphere with a horizontal boundary at 340 hPa, and evaluate the LEC-terms in the upper and lower region. Additionally, we must compute the corresponding fluxes at the boundary (see Chapter 2 and Appendix A). The values for this split-LEC (Fig. D.3 in Appendix D) are very similar to the 2xCO_2 split-LEC values (Fig. 2.20). However, we will focus on the energetics response as measured by the changes in the energy generation, conversion and dissipation rates (Fig. 3.7). Once again, comparing this response with the 2xCO_2 response (Fig. 2.21) reveals that both experiments show the same features: a strengthening of the LEC in the upper region, and a weakening below. Furthermore, the magnitude of these responses is roughly identical in FULL relative to CTRL as due to the doubling of CO_2 concentrations.

Static stability

The last quantities we would like to compare between the FULL integration and the 2xCO_2 integration are the changes in the vertical profiles of the inverse mean static stability, gamma (γ), and of zonal-mean available potential energy (P_m).

Regarding the relative changes of γ in FULL (left plot in Figure 3.8), a comparison with the 2xCO_2 relative change (Fig. 2.22) reveals how similar they are. From the surface up to 500 hPa the two profiles are identical. Above this level, the profiles reach a minimum (or maximum decrease) around 400 hPa. This minimum is about 1% weaker in FULL ($\approx$-14%, and $\approx$-15% in the 2xCO_2 case). Higher up it reaches a maximum increase around 200 hPa, which is also by about 1% stronger in FULL (around +12%, and $\approx$+11% in the 2xCO_2 case). In other words, the profile of FULL in this region has the same shape as in the 2xCO_2 case, but slightly displaced towards higher values. Nevertheless, this is a very small difference. Higher up in the stratosphere above 100 hPa, the profiles differ more. FULL reaches an increase of about 1.5% in the uppermost level; this level in the 2xCO_2 case reaches an increase of 6%. This is due to the cooling in the stratosphere, which we have not tried to reproduce as precisely as the tropospheric warming. The stronger stratospheric cooling in the 2xCO_2 case above the tropopause accounts for a stronger reduction in static stability in the stratosphere (or a stronger increase in γ) compared to the change in FULL. Although this difference is clear, it appears in a region that we are not considering as important as the troposphere for this study. The fact that even with this difference in the stratospheric temperature change we still obtain the same energetics response in the troposphere, corroborates this.

The profile of the change of P_m has in general the same shape in FULL (Fig. 3.8, right panel) and in the 2xCO_2 case (Fig. 2.23). However, in FULL the profile from the surface up to just above 400 hPa is slightly displaced towards lower values, compared to the 2xCO_2 run. Again, this is a very small difference. For the rest, there is no significant difference. The analysis of these two plots would lead us to the same conclusion as with the 2xCO_2 run. The decrease in P_m near the surface, up to about 750 hPa can be attributed to changes in temperature variance,

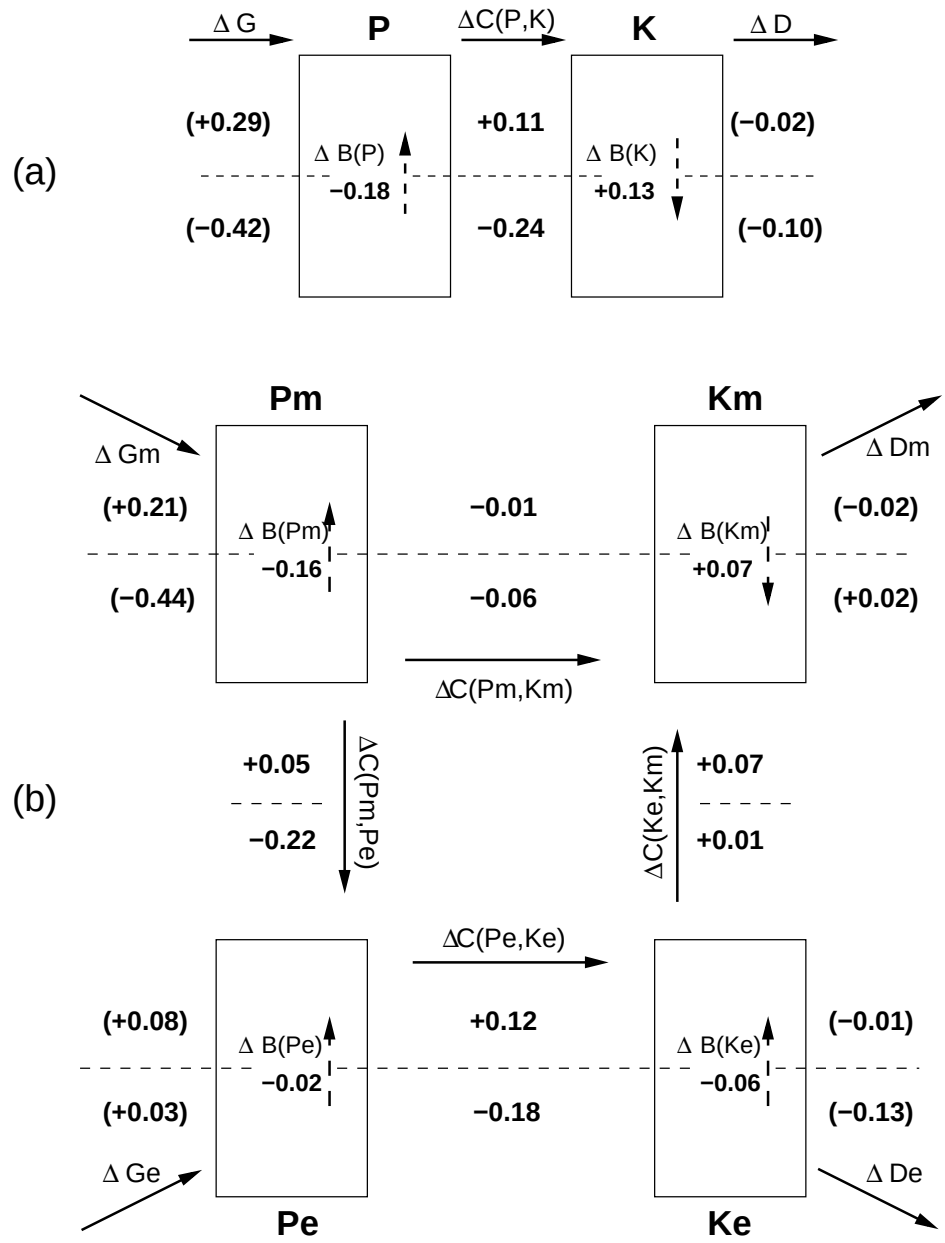

Figure 3.7: (a) 2-box and (b) 4-box diagram of the changes in energy generation, conversion and dissipation rates in the LEC in FULL relative to CTRL, evaluated from Figure D.3. Units are W m^{-2}. Arrows indicate the direction corresponding to positive values; negative values imply opposite direction.

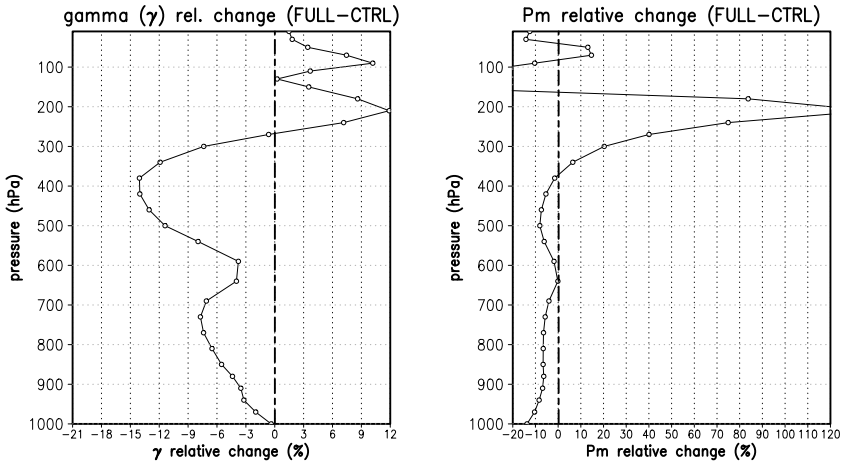

Figure 3.8: Relative change of the vertical profile of γ (left panel) and P_m (right panel) in FULL relative to CTRL (difference divided by CTRL value).

because the relative change in γ is not strong enough. From this level up to about 400 hPa the decrease in P_m can be attributed to the increase in mean static stability (decrease in γ). The strong increase of P_m above 350 hPa and below 150 hPa is clearly due to changes in horizontal temperature variance. Once again, we assume that the response of G_m, which, from the point of view of the LEC is the driver of the energetics responses, must be very similar to this P_m-response.

In conclusion, we have verified that the 2xCO_2 energetics response can be reproduced with a temperature-nudged integration where we force the atmosphere with the zonal-mean 2xCO_2 warming pattern, instead of explicitly increasing the CO_2 concentrations. The temperature-nudged response resembles so much the 2xCO_2 response, that we are confident that (a) the nudging method works as expected, without introducing any different effects than the physical effects of the warming pattern, and (b) the 2xCO_2 energetics response is a consequence of the zonal-mean warming pattern. Having achieved this, we can analyse the energetics response of the two remaining integrations, UP and SFC, and compare them with the response of FULL.

3.3.2 FULL as a linear combination of UP and SFC

In order to understand the response due to the 2xCO_2 warming pattern by studying the responses of the experiments with the decomposed warming pattern (UP and SFC), we must first verify that adding these decomposed responses results indeed in a response similar to the FULL one. That is, that they combine approximately linearly. If we cannot verify this, by understanding the separate UP and SFC responses we will not gain much understanding about the combined, 2xCO_2-response (here represented by the FULL-response). In this subsection we will emphasise on the verification of the linearity in the combination of the two responses, while we describe the main features of each response in terms of the global LEC-response, the vertical cross-sections of the LEC-terms, and the split-LEC response. This is a necessary step

before deepening in the analysis and understanding of the separate responses of the UP and SFC experiments.

Lorenz Energy Cycle response

We start by looking at the global LEC-response. We are interested in the energetics response, i.e., the changes in energy generation, conversion and dissipation rates of these integrations relative to CTRL, and in comparing this with the energetics response of FULL (Fig. 3.9). The figure corresponding to FULL was already shown in the previous section, but we show it again here to facilitate the comparison. For further reference, the values of the LEC-terms in each experiment (not just the changes relative to CTRL) are shown in Appendix D (Figures D.1 and D.2).

First of all, UP and SFC have opposite energetics responses. We noted in Chapter 2 how Held (1993) pointed out the possible dual role of the warming pattern in terms of strengthening or weakening baroclinic eddies. The strengthening would be due to the tropical, upper-tropospheric warming that enhances the meridional temperature gradient, and the weakening due to the high-latitude surface warming, which does the opposite. Here, in terms of the LEC, we indeed see a pronounced dual role of these warming patterns, but exactly the other way around. The tropical upper-tropospheric warming (UP) causes a weakening of the LEC, and the high-latitude, surface warming (SFC) causes a strengthening of the LEC. This is true for the 2-box LEC and for the path $P_m \rightarrow P_e \rightarrow K_e$ in the 4-box LEC, which is related to baroclinic instabilities. On the other hand, the conversion term $C(K_e, K_m)$, which is related to the barotropic processes, behaves differently. Instead of decreasing in UP, it increases, whereas in SFC it does not change significantly. This response of $C(K_e, K_m)$ explains why K_m increases strongly in UP, but not in SFC (see Figures D.1 and D.2 in Appendix D). We will return to this later in this chapter.

Second, it is the energetics response of UP the one that best resembles FULL's energetics response. Furthermore, if we add the energetics responses of UP and SFC, we obtain a response even more similar to FULL's response. We can reproduce the FULL response by adding the energetic responses of the decomposed warming pattern. Figure 3.10 shows the result of adding the UP and SFC responses. This suggests that the 2xCO_2 energetics response behaves rather linearly with respect to the two main features of the warming pattern. Though with a slightly stronger weakening effect, this is very similar to the FULL energetics response (Fig. 3.9, upper panel). In conclusion, we find that regarding the global LEC, the UP warming pattern causes a weakening of the LEC, whereas the SFC warming pattern causes a strengthening of the LEC. Additionally, the sum of these two responses is very similar to the FULL response.

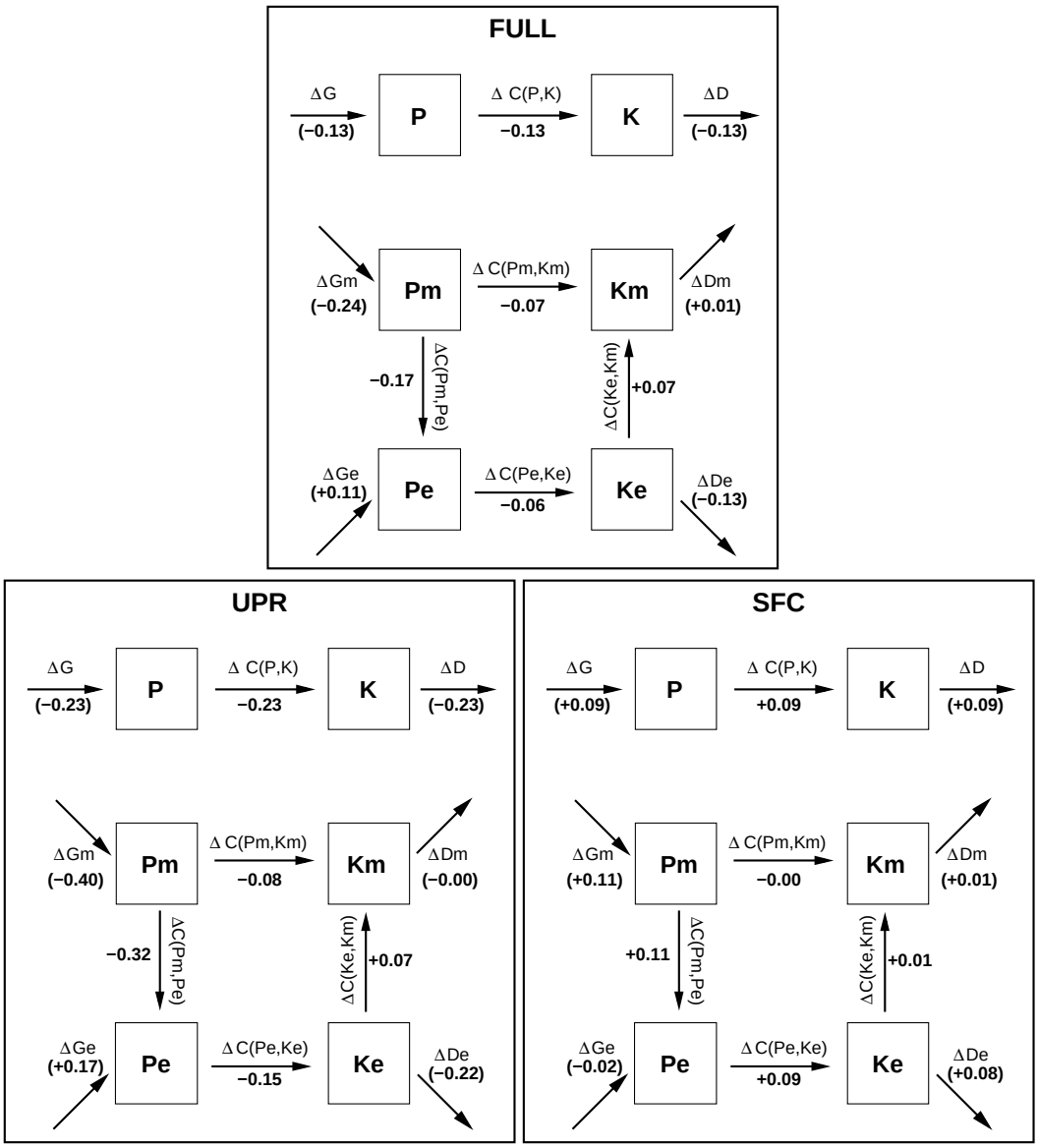

Figure 3.9: 2-box (above) and 4-box (below) diagrams of the changes in energy generation, conversion, dissipation rates, and boundary fluxes in the LEC for FULL (upper panel), UP (lower left panel) and SFC (lower right panel) relative to CTRL. Units are W m^{-2}. Arrows indicate the direction corresponding to positive values; negative values imply opposite direction.

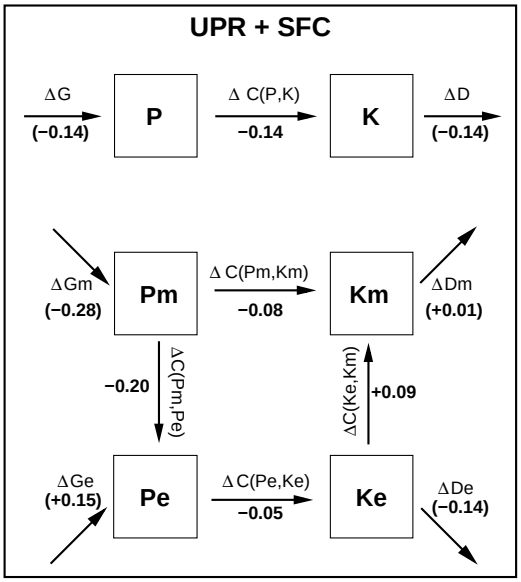

Figure 3.10: Energetics response of UP (left panel, Fig. 3.9 plus the energetics response of SFC (right panel, Fig. 3.9. Units are W m^{-2}. Arrows indicate the direction corresponding to positive values; negative values imply opposite direction.

Vertical cross-sections

Here we analyse the vertical cross-sections of the changes in the LEC-terms in UP and SFC (Figures 3.11 and 3.12), and compare them to the FULL experiment (Fig. 3.6). In both cases we observe a dual response of the LEC-terms: a decrease below, and an increase above. Nevertheless, the magnitudes are different in each experiment, as well as the altitudes. In UP (Fig. 3.11) the decrease response is stronger than the increase response, whereas in SFC (Fig. 3.12) the increase response is stronger than the decrease response. Furthermore, the increase response in UP shows up at a higher altitude than the increase response in SFC. Actually, the altitude of the increase response in SFC roughly coincides with the altitude of the decrease response in UP. Visual inspection of the patterns in figures 3.6, 3.11 and 3.12 suggests that the increase response in the upper troposphere is due to both the SFC and the UP responses, but predominantly due to SFC. On the other hand, the decrease response below is due to the UP response, and partly compensated by the SFC response. This suggests again that UP and SFC combine approximately linearly to produce the FULL response.

We have verified this by plotting the differences between the FULL-plots and the UP and SFC-plots in Appendix D. Figure D.4 depicts how much of the FULL response is not reproduced by the UP response. In terms of the decrease-response in FULL, except for the northern high-latitudes in P_m and P_e, the UP response reproduces it rather well. However, in terms of the increase-response in the upper troposphere, the UP-response is not as strong as the FULL-response. Finally, note the strong resemblance between the patterns in Figure D.4 and the

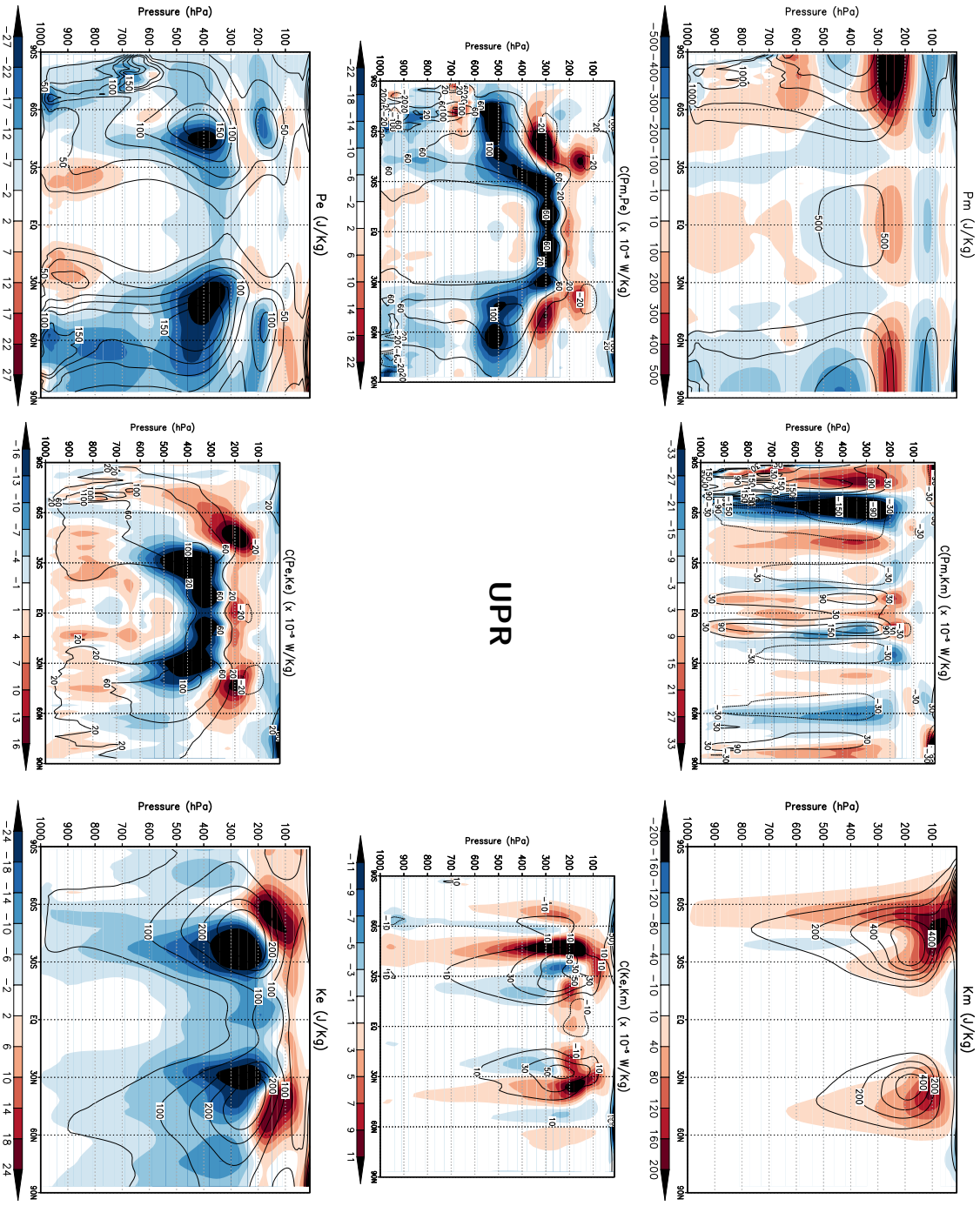

Figure 3.11: Vertical cross sections of the 4-box LEC terms for the CTRL integration (contours), and their change in UP (color shaded). Counterclockwise, starting from the upper left: P_m, $C(P_m, P_e)$, P_e, $C(P_e, K_e)$, K_e, $C(K_e, K_m)$, K_m, and $C(P_m, K_m)$. Units are J Kg^{-1} for reservoirs, and $\times 10^{-5}$ W m^{-2} for conversion terms.

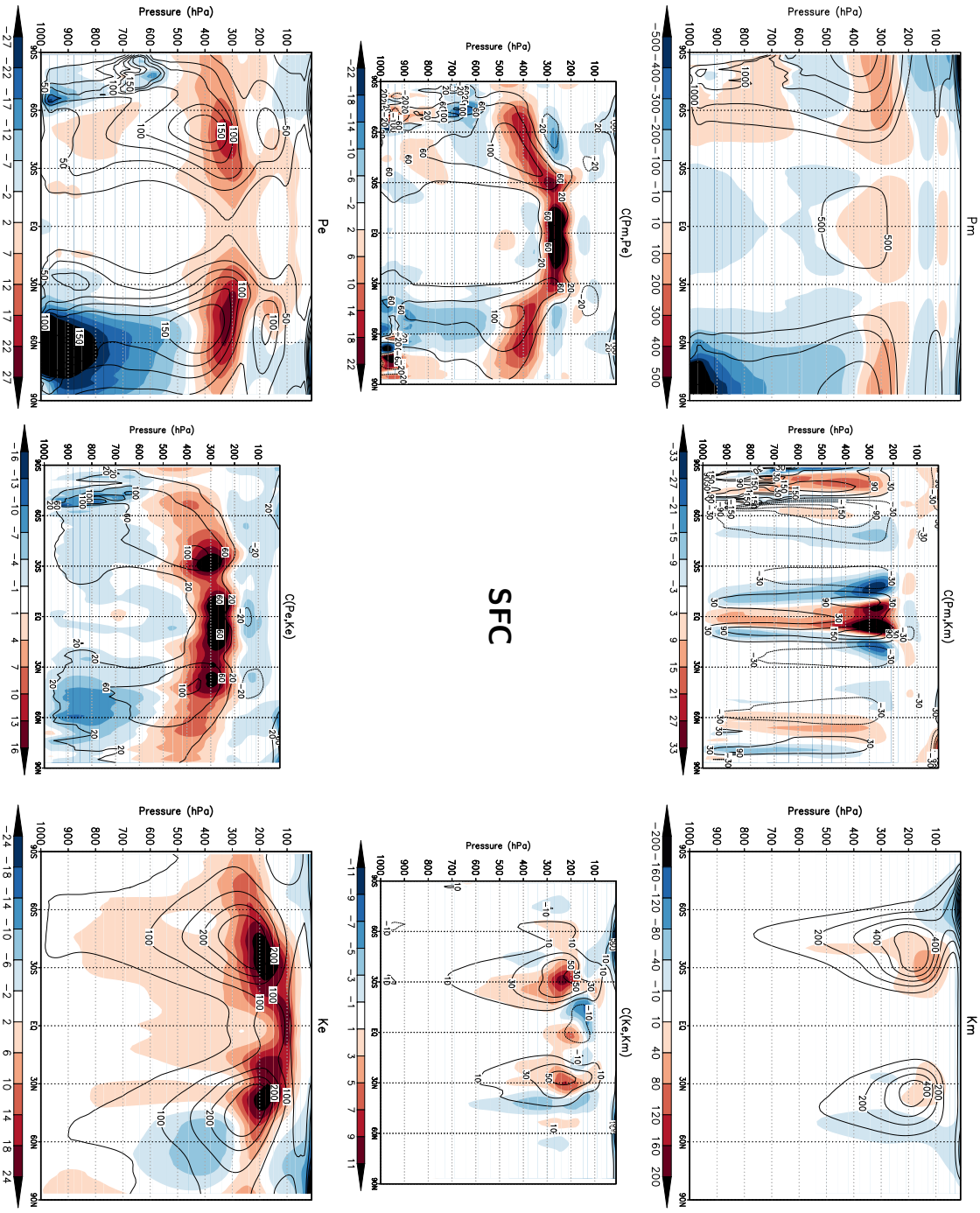

Figure 3.12: Vertical cross sections of the 4-box LEC terms for the CTRL integration (contours), and their change in SFC (color shaded). Counterclockwise, starting from the upper left: P_m, $C(P_m, P_e)$, P_e, $C(P_e, K_e)$, K_e, $C(K_e, K_m)$, K_m, and $C(P_m, K_m)$. Units are J Kg^{-1} for reservoirs, and $\times 10^{-5}$ W m^{-2} for conversion terms.

patterns in Figure 3.12. This means that the fraction of the FULL-response that is not reproduced by the UP-response is captured by the SFC-response. An analogous conclusion results from the difference between the vertical cross-sections of FULL and SFC (Fig. D.5). Note now how similar these vertical cross-sections are to the ones of the UP-response (Fig. 3.11). This means now that the fraction of the FULL-response that is not reproduced by the SFC-response is captured by the UP-response. This would imply that adding the UP and SFC responses should reproduce the FULL-response, and indeed, this is the case: plotting the difference between the FULL-response and the sum of the UP and SFC-responses (Fig. D.6) reveals almost no patterns. Clearly, considering the sum of the two responses not only captures the global LEC-response of FULL, as seen in Figure 3.10, but also the pattern of change in the vertical cross-sections of each LEC-term. The plots in Figure D.6 show very small amplitudes compared to any of the other vertical cross-sections plots, and the pattern of increase in the upper troposphere and decrease below has disappeared. We can conclude that, in terms of the vertical cross-sections of the LEC-terms, the responses of UP and SFC combine approximately linearly to produce the FULL response.

Splitting the atmosphere

The next step, given that both UP and SFC show a pattern of increase of the LEC-terms in the upper-troposphere and decrease below, is to analyse the split-LEC. Just as we did with FULL, we split the atmosphere at the isobaric level of 340 hPa. The values of the 2-box and 4-box split-LEC diagrams of UP and SFC are shown for further reference in Appendix D (Figures D.7 and D.8), but we analyse here the changes relative to CTRL (Figures 3.13 and 3.15).

Regarding the 2-box LEC (Fig. 3.13), the response of $C(P, K)$, which is the one we calculate directly from the model output, is a weakening in both regions—above and below 340 hPa—in UP, although much more pronounced in the lower region. In SFC it strengthens in the upper region, and slightly weakens below. Adding up these two responses, UP and SFC, gives a response that is remarkably similar to the FULL response (see Figure 3.14). This confirms again the strong linearity in the combination of the two effects of the warming patterns.

Regarding the 4-box LEC diagrams (Figures 3.15 and 3.16), we find again that the response of FULL seems to be decomposed into the UP and SFC responses. When adding these two responses (Fig. 3.16), we obtain once more a response remarkably similar to the FULL response. From figure 3.15 we can conclude that the strengthening response in the upper region throughout the path $P_m \rightarrow P_e \rightarrow K_e$ is caused by the SFC warming pattern, whereas the weakening response in the lower region throughout this same path is mainly caused by the UP warming pattern. The contribution to this weakening by the high-latitude surface warming, although not zero, is much smaller. On the other hand, the strengthening of the conversion term $C(K_e, K_m)$ in the upper region is caused by the tropical, upper-tropospheric warming, as we saw before in the globally integrated LEC. This suggests that UP has a weakening effect in the lower region in the terms related to baroclinic instability, but a strengthening effect in the upper region in the

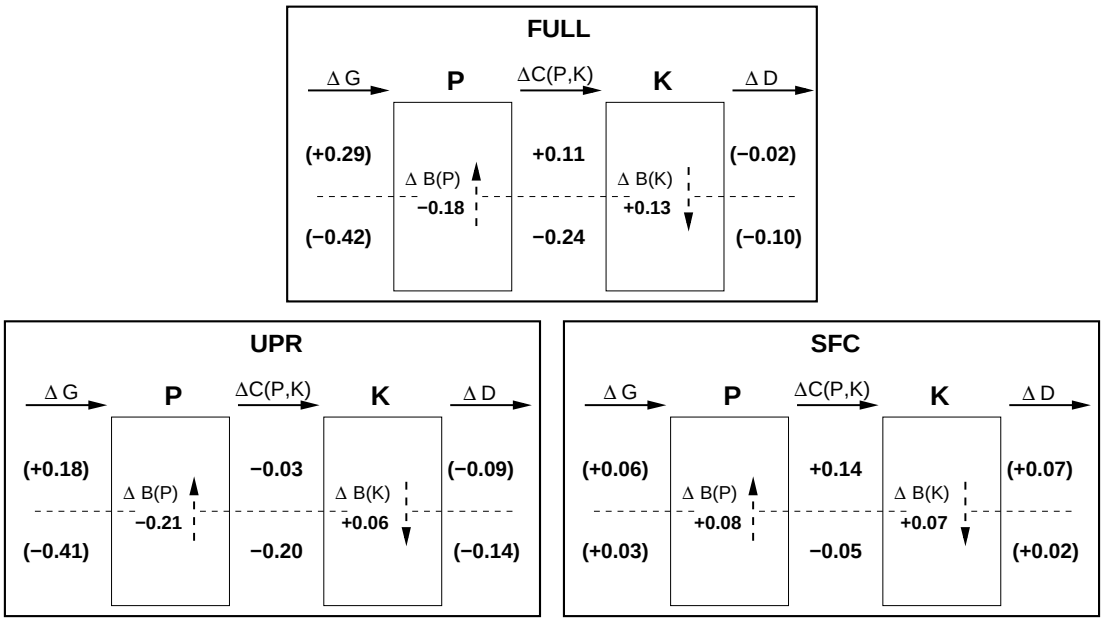

Figure 3.13: 2-box diagrams of the changes in energy generation, conversion, dissipation rates, and boundary fluxes in the LEC split at 340 hPa for FULL (upper panel), UP (lower left panel) and SFC (lower right panel) relative to CTRL. Units are W m^{-2}. Arrows indicate the direction corresponding to positive values; negative values imply opposite direction.

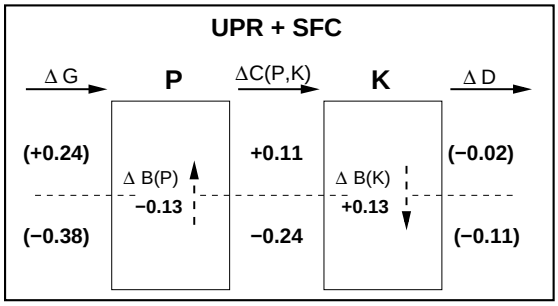

Figure 3.14: 2-box LEC diagram of the changes in energy generation, conversion, dissipation rates and boundary fluxes in the LEC split at 340 hPa for UP + SFC relative to CTRL. Units are W m^{-2}. Arrows indicate the direction corresponding to positive values; negative values imply opposite direction.

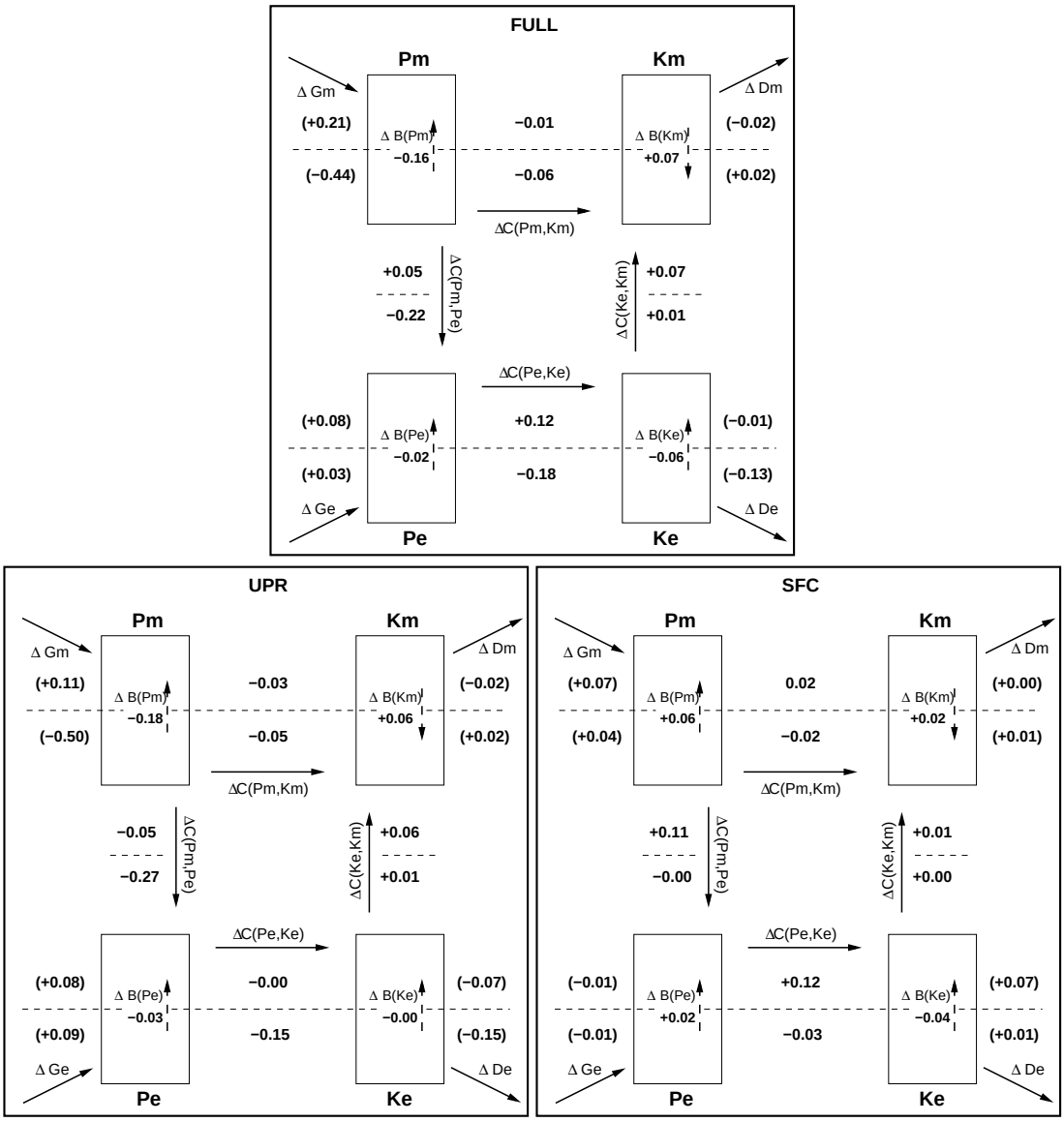

Figure 3.15: 4-box diagrams of the changes in energy generation, conversion, dissipation rates, and boundary fluxes in the LEC split at 340 hPa for FULL (upper panel), UP (lower left panel) and SFC (lower right panel) relative to CTRL. Units are W m^{-2}. Arrows indicate the direction corresponding to positive values; negative values imply opposite direction.

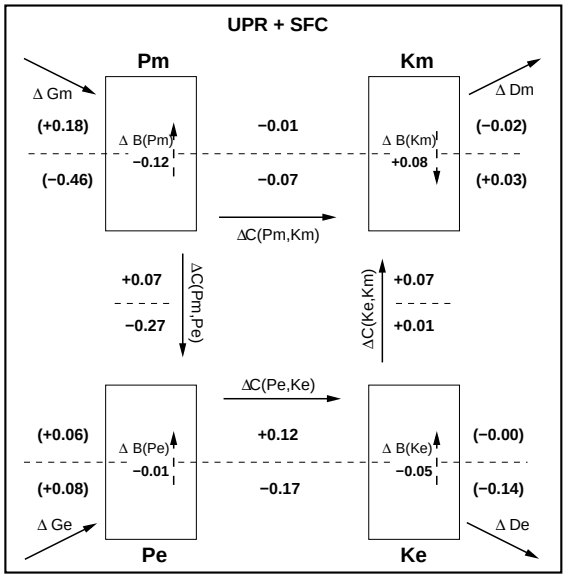

Figure 3.16: 4-box LEC diagram of the changes in energy generation, conversion, dissipation rates and boundary fluxes in the LEC split at 340 hPa for UP + SFC relative to CTRL. Units are W m^{-2}. Arrows indicate the direction corresponding to positive values; negative values imply opposite direction.

conversion related to barotropic processes. On the other hand, SFC has a strengthening effect in the upper region in the terms related to baroclinic instability, and very little effect elsewhere, except for a small contribution to the weakening of $C(P_e, K_e)$ in the lower region.

Thus, we can conclude that also in terms of the split-LEC, adding the responses of UP and SFC provides a very good approximation of the FULL response. With this, we have been able to verify this linear behavior in terms of three different aspects of our LEC-analysis: the global LEC-response, the changes in the vertical cross-sections of each term, and the split-LEC response. Studying the individual responses will therefore help in understanding the combined FULL energetics response, a good proxy for the 2xCO$_2$ energetics response. This is the aim of the following subsections.

3.3.3 The tropical upper-tropospheric warming (UP)

In this subsection we analyse in more detail the response of the UP experiment, in which the warming pattern consists of a strong warming in the tropical upper-troposphere, with its maximum around 250 hPa (see lower left panel of Figure 3.1). In the previous subsection we pointed out the principal features of the energetics response of this experiment. We will now analyse them in 5 steps that correspond to the main changes of the LEC in this case:

1. Change in strength of the 2-box LEC ($C(P, K)$).
2. Changes in the conversion terms $C(P_m, P_e)$ and $C(P_e, K_e)$ (baroclinic response)
3. Changes in $C(K_e, K_m)$ (barotropic response)

4. Changes in $C(P_m, K_m)$ (changes in merdional overturning circulations)

5. Changes in the energy reservoirs, in particular K_e, an indicator of extratropical storm activity.

1. Change in strength of 2-box LEC

There is a clear global weakening of the LEC in the UP experiment relative to CTRL ($C(P, K)$ decreases by 0.23 W m^{-2}, or 9.7%) (Fig. 3.9, lower left panel.). This weakening in the energetic activity in UP is the main cause of the weakening in the FULL experiment, hence in the 2xCO_2 case. We can conclude from this that the overall weakening of the LEC due to CO_2-doubling is due to this tropical, upper-tropospheric warming, and not due to the surface warming. Actually, the high-latitude surface warming counteracts this weakening partly, because its global effect is a strengthening of the LEC (we will return to this later). Note that when splitting the atmosphere at 340 hPa, it is clear that the strongest weakening signal of the LEC is in the lower region, even though the main feature of this warming pattern is located above, around 250 hPa. The fact that the LEC weakens due to this warming pattern suggests that the mean static stability effects are more important than the horizontal temperature variance changes for the energetics response.

2. Changes in $C(P_m,P_e)$ and $C(P_e,K_e)$ – baroclinic response

The global weakening of the LEC is a result of a weakening response in both conversion terms, $C(P_e, K_e)$ and $C(P_m, K_m)$, with the former having a larger contribution. The contribution of $C(P_e, K_e)$ to the weakening is accompanied by a strong decrease in the conversion term $C(P_m, P_e)$. This combination is an indication of a decrease in baroclinic activity. But before talking about baroclinicity, we will analyse this response from the point of view of the LEC itself, as we have done for the 2xCO_2 experiments.

Just as in the 2xCO_2 experiments, the strongest weakening of the LEC appears in G_m, the generation rate of P_m. In UP, the weakening of G_m is even stronger than in FULL or in the 2xCO_2 case: 0.40 W m^{-2} less, a decrease of almost 17%, compared to 10% in FULL. This weakening becomes less pronounced as one follows the conversion terms through the path $P_m \rightarrow P_e \rightarrow K_e$, suggesting that the main driver is the G_m-response. In the 2xCO_2 case we assumed G_m and P_m should behave in a similar way because both are proportional to γ (the inverse mean static stability), and because we expect $[\langle T \rangle]''$ to be highly correlated with $[\langle Q \rangle]$ (see Section 2.2.3). Therefore, analysing the changes in P_m could be useful for understanding the changes in G_m, as long as this assumption remains valid. Figure 3.17 shows the relative changes of gamma (γ) (left) and P_m (right) in the three temperature-nudged experiments.

First of all, note that the relative changes of γ in UP and FULL are very similar, whereas the relative change in SFC has a completely different vertical profile. We can infer from this that the changes in mean static stability in FULL (or in the 2xCO_2 experiment) are mainly

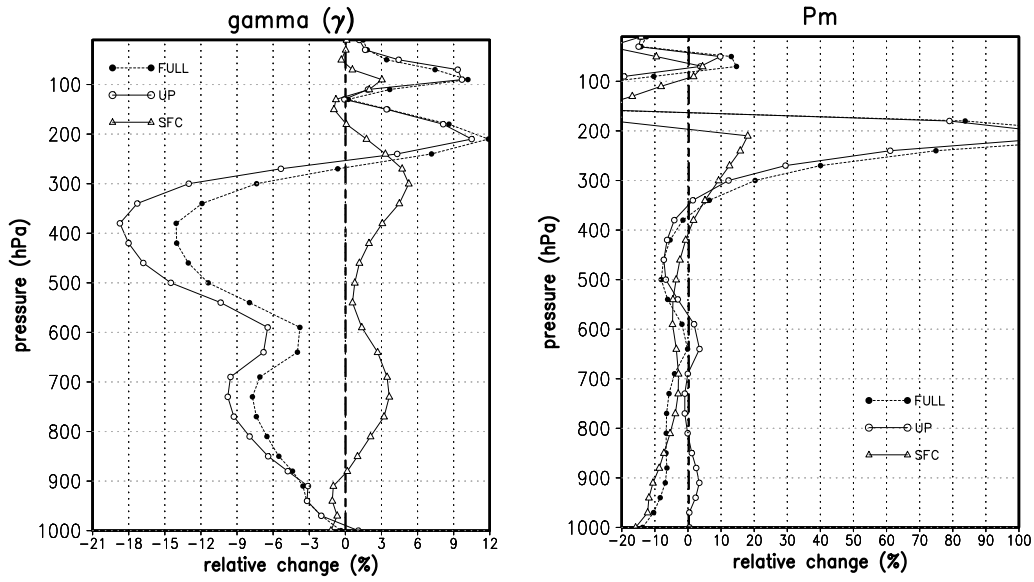

Figure 3.17: Change in the vertical profile of γ (left) and P_m (right) in FULL (filled circles), UP (empty circles) and SFC (triangles) relative to CTRL. The thick dashed vertical line indicates zero relative change.

due to the tropical, upper-tropospheric warming. However, the γ-relative changes in UP and FULL differ in magnitude. The decrease of γ throughout the whole troposphere is about 3-5% stronger in UP than in FULL. Without the surface warming, the stabilizing effect of the upper-tropospheric warming is expected to be stronger due to the larger effect on the lapse rate. Despite this stronger reduction of γ, P_m decreases less in UP than in FULL from the surface up to about 500 hPa. This implies that the horizontal variance of temperature, $[\langle T\rangle]''^2$, must have increased enough to overcome the additional decrease in γ. This is not surprising, because the UP warming pattern increases the horizontal temperature variance due to the stronger warming in low latitudes at all vertical levels.

Nevertheless, this is not how G_m responds. P_m decreases *less* in UP than in FULL throughout the lower region (below 340 hPa), but G_m decreases *more* in UP than in FULL (just as γ does). This implies that in this case $[\langle T\rangle]''[\langle Q\rangle]''$ does not respond like $[\langle T\rangle]''^2$, and G_m here is more sensitive to the changes in γ than P_m is. In other words, the UP warming pattern causes a much larger increase in the horizontal temperature variance than in the product $[\langle T\rangle]''[\langle Q\rangle]''$, so that the G_m-response is more influenced by the γ changes, whereas the P_m response is more influenced by the $[\langle T\rangle]''^2$-response. Therefore, in this case the changes in P_m are not good indicators of the changes in G_m, and hence of the changes in energetic activity. Unfortunately, we cannot draw any other conclusions regarding the effect of the changes in $[\langle T\rangle]''[\langle Q\rangle]''$ on G_m because we have no output data of the diabatic heating rate Q. But the fact that G_m decreases more in UP than in FULL, just as γ and the conversion terms $C(P_m, P_e)$ and $C(P_e, K_e)$ do, indicates that the increase in mean static stability is the main cause for the decrease in G_m,

hence for the weakening of the LEC in UP. This stabilizing effect dominates over the effects due to changes in horizontal temperature distribution.

An simple way of understanding this response is that such a warming pattern (UP), which tends to reduce the lapse rate and therefore create more stable conditions in the atmosphere, will be less favorable for vertical motions in the atmosphere. This means less conversion of available potential energy into kinetic energy, because $C(P, K)$ consists of rising of relatively warm air and sinking of relatively cold air (see Eq. (A.3) and (A.5)). Hence, a weaker LEC.

We can also understand this response from the point of view of baroclinicity changes. The conversion term $C(P_m, P_e)$ represents how the eddies transport heat horizontally along the meridional temperature gradient (first term on the right side of equation (A.2)), and vertically along the vertical temperature gradient (second term on the right side of equation (A.2)), with the horizontal transport being the dominating term. At the same time, rising of relatively warm air and sinking of relatively cold air in the eddies converts this eddy available potential energy into eddy kinetic energy ($C(P_e, K_e)$). These processes are related to baroclinic activity (Peixoto and Oort, 1992). Baroclinic instability is associated to vertical shear in the mean flow, which due to thermal wind balance, imply horizontal temperature gradients. The latter provide the energy source through the associated available potential energy (Holton, 2004). Clearly, changes in baroclinicity due to the warming pattern can provide us with additional information about the weakening of these two conversion rates from a different perspective. In the following, we will provide further support to our results by considering two different measures, without carrying out a detailed analysis on baroclinicity.

The most widely used indicator for baroclinicity is the maximum Eady growth rate (Eady, 1949; Lindzen and Farrell, 1980; Pedlosky, 1987), given by

$$\sigma_{eady} = 0.31 \frac{|f| \frac{\partial u}{\partial z}}{N} = 0.31 \frac{M^2}{N}, \tag{3.4}$$

where f is the Coriolis parameter, u is the zonal wind velocity, z is height, and N is the Brunt-Väisälä frequency, $\sqrt{(g/\theta)(\partial\theta/\partial z)}$, a measure of static stability. Because of the thermal wind balance, the vertical wind shear term $|f|\frac{\partial u}{\partial z}$ can be written in terms of the meridional temperature gradient $M^2 = |\frac{-g\partial\theta}{\theta\partial y}|$. According to Lim and Simmonds (2007, 2009), σ_{eady} is dominated by the meridional temperature gradient, and underestimates the static stability effect so that it does not reproduce well enough the Southern Hemisphere (SH) extratropical cyclone characteristics. They argue that a more appropriate measure is the non-dimensional *baroclinic parameter* (BP) (Green, 1960; Held, 1978; Pedlosky, 1987),

$$BP = \frac{f^2 \frac{\partial u}{\partial z}}{\beta H N^2} = \frac{|f| M^2}{\beta H N^2}, \tag{3.5}$$

where β is the latitudinal variation of f, and H is the density scale height, given by $\left(\frac{1}{\rho}\frac{\partial \rho}{\partial z}\right)^{-1}$. This parameter results from Charney's model (Charney, 1947), which as opposed to Eady's model, takes into account the sphericity of the earth (through β), and does not consider an

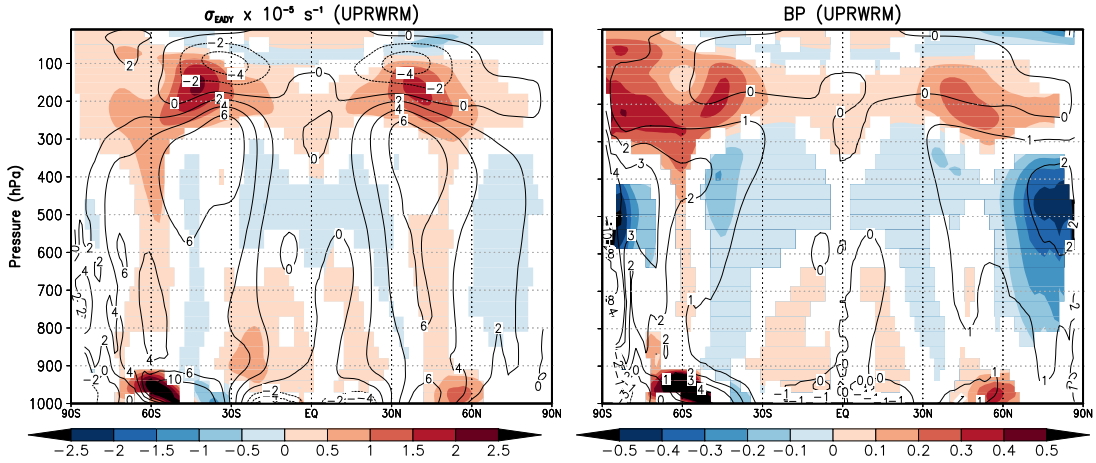

Figure 3.18: Zonal mean plots of σ_{eady} (left panel) and BP (right panel) in CTRL (contours), and their change in UP (color shaded). Only differences with 95% significance level are shown, based on a standard t-test. Units are 10^{-5} s^{-1} for σ_{eady}, BP is dimensionless.

upper boundary but a finite density scale height. Our focus is global, and therefore taking the sphericity of the earth into account seems more appropriate. However, having in mind that σ_{eady} is such a widely used measure, we will also consider it. We investigate here the changes in both measures, and at the same time we can use this opportunity to compare their performance in the context of our LEC-results.

The changes in the zonal mean pattern of σ_{eady} in the UP experiment (Fig. 3.18, left panel) are clearly dominated by the changes in meridional temperature gradient M^2 (Fig. 3.19, left

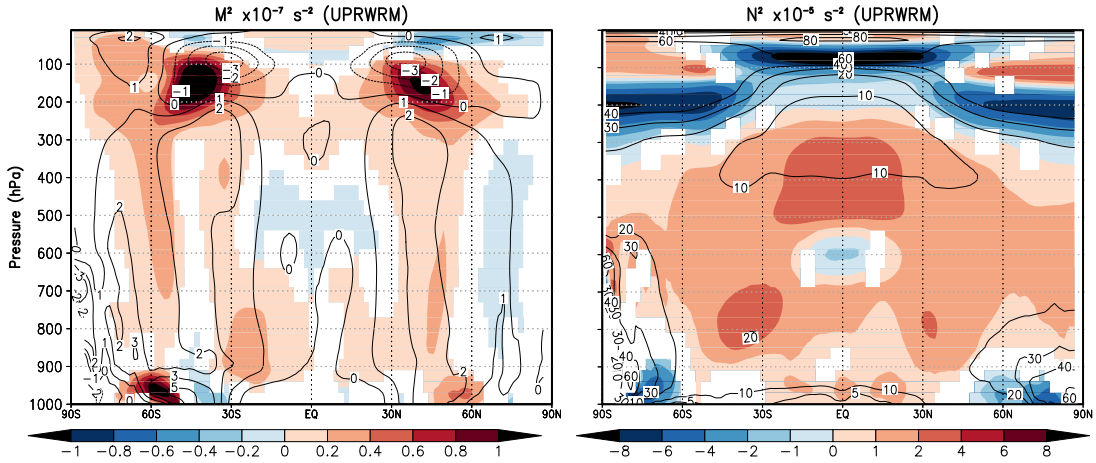

Figure 3.19: Zonal mean plots of M^2 (left panel) and N^2 (right panel) in CTRL (contours), and their change in UP (color shaded). Only differences with 95% significance level are shown, based on a standard t-test. Units are 10^{-7} s^{-2} for M^2, and 10^{-5} s^{-2} for N^2.

panel), as Lim and Simmonds (2007, 2009) noted. Both plots show roughly the same patterns, and in general, the increase response dominates. The maximum increases in σ_{eady} (and therefore in M^2 as well) are located between 30-60°N-S between 100-200 hPa, and at the surface near 60°N and S. The increases in the upper region match with the increases in this same region in the conversion terms $C(P_m, P_e)$ and $C(P_e, K_e)$ (see Fig. 3.11). On the contrary, the strong increases in σ_{eady} and BP (Fig. 3.18, right panel) near the surface around 60°N and 60°S are not visible in these conversion terms. These suggest an intensification and poleward displacement of the regions of stronger baroclinicity near the surface, especially in the SH, but are not visible in the LEC. On the other hand, the weakening of the conversion rates $C(P_m, P_e)$ and $C(P_e, K_e)$ below 300-400 hPa, which is their dominant response in this experiment, cannot be associated to a similar response in σ_{eady}. Nevertheless, there is a slight decrease in σ_{eady} around 400-500 hPa in the low latitudes, and in the high northern latitudes. However, based on this slight weakening in the σ_{eady}-plot, one would not expect such a strong decrease in baroclinic activity in this region, as the conversion terms suggest.

Looking further at the changes in BP (Fig. 3.18, right panel), we see that this parameter retains the two increase regions in the upper region and near the surface which are visible in σ_{eady}, but now reveals a clear decrease response throughout most of the troposphere both in mid-latitudes and even stronger in high latitudes, in particular in the Northern Hemisphere (NH). Hence, the pattern of change of BP is much more consistent with the pattern of change of $C(P_m, P_e)$ and $C(P_e, K_e)$. The plot of the changes in N^2 (Fig. 3.19, right panel) indicates that there is a clear and generalized increase in N^2 throughout the whole troposphere, except for two small regions near the surface at high latitudes. This implies an increase in static stability that we can now clearly relate to a general weakening in baroclinicity, as measured by BP (note from expression (3.5) that BP is inversely proportional to N^2). In other words, the measure of baroclinicity given by BP is more consistent with the changes we find in the conversion terms $C(P_m, P_e)$ and $C(P_e, K_e)$ than σ_{eady} is, because BP takes into account a stronger effect of static stability. This supports our hypothesis that the increase in mean static stability due to the strong upper tropospheric warming is the main cause for the weakening of the LEC, and in particular for the weakening response of $C(P_m, P_e)$ and $C(P_e, K_e)$. Furthermore, it indicates that the global effect of the tropical upper-tropospheric warming in terms of baroclinicity is a decrease, mainly due to the overall increase in mean static stability. This is consistent with the (more local) results obtained by Lim and Simmonds (2007, 2009).

3. Change in $C(K_e,K_m)$ – barotropic response

The conversion rate $C(K_e, K_m)$ experiences a clear increase in the UP experiment, as well as in the FULL experiment. In order to understand the cause of this increase, it is worth going back to the complete expression for this term (Eq. (A.4), Appendix A). The contribution of each term on the right hand side of equation (A.4) to the total value of $C(K_e, K_m)$ in CTRL, as well as the corresponding changes in each of the temperature-nudged experiments, are presented in

Table 3.1: Contribution of individual terms of $C(K_e, K_m)$ in CTRL, and their changes in the temperature-nudged experiments compared to CTRL. Units are W m^2. Only the general form of each term is given. See equation (A.4) in Appendix A for the complete expressions of each term.

Term	General form	CTRL	Δ UP	Δ SFC	Δ FULL
1:	$u'v'\left(\partial[u]/\partial y\right)$	0.572	+ 0.039	+ 0.005	+ 0.034
2:	$v'^2\left(\partial[v]/\partial y\right)$	-0.043	+ 0.010	- 0.006	+ 0.002
3:	$\omega'u'\left(\partial[u]/\partial p\right)$	0.234	+ 0.026	+ 0.013	+ 0.038
4:	$\omega'v'\left(\partial[v]/\partial p\right)$	-0.012	- 0.002	+ 0.001	- 0.002
5:	$-u'^2\left(1/a\right)\tan\phi$	0.006	+ 0.000	+ 0.000	+ 0.001
SUM:	$C(K_e, K_m)$	0.757	+ 0.073	+ 0.013	+ 0.073

Table 3.1. Clearly, the first and the third terms are the dominating ones, while the others are one and two orders of magnitude smaller.

Most authors (e.g., Peixoto and Oort, 1992; Boer and Lambert, 2008) consider this conversion rate between K_e and K_m as related to barotropic processes. Barotropic instability is associated to horizontal shear in the mean flow, being the kinetic energy of the mean flow its energy source (Holton, 2004). Therefore, it does not need horizontal temperature gradients as baroclinic instability does. Looking at the general form of the terms of $C(K_e, K_m)$ in table 3.1, it is clear that they are indeed related to the shear of the mean flow. However, the fact that they also include momentum eddy fluxes of the form $u'v'$ indicates that they may be related to eddy-mean flow interaction as well. Nevertheless, the eddy-mean flow interaction is not well represented with the conventional Eulerian mean decompositions which we use here (Plumb, 1983; Holton, 2004). For a better representation of this process, one should use a formulation based on the Transformed Eulerian Mean (TEM), which gives rise to the Elliassen-Palm (E-P) flux (Holton, 2004). This E-P flux describes the forcing of the zonal mean flow by the eddies in terms of the divergence of the products $\langle u'v' \rangle$ and $\langle v'T' \rangle$. In our LEC formulation these terms (and not their divergences) appear distributed in $C(K_e, K_m)$ and $C(P_e, P_m)$, so that although this process of eddy-mean flow interaction is somehow implicitly included, it is not possible to obtain here a good description of it. Therefore, changes in the eddy-mean flow interaction would produce changes in $C(K_e, K_m)$ and in $C(P_e, P_m)$, but it would be difficult to obtain a clear picture of their response using this LEC formulation.

The changes we see in $C(K_e, K_m)$ appear to be more related to changes in the wind shear than to changes in the eddy-mean flow interaction, because they are accompanied by the intensification of the jets (seen here as a 17%-increase in K_m), and their location also matches with this intensification. If this is the case, we can conclude that the $C(K_e, K_m)$ response is driven by changes in barotropic instability and not by changes in eddy-mean flow interaction. We can verify this by plotting the zonal mean change in the latitudinal shear of $[u]$ in UP relative

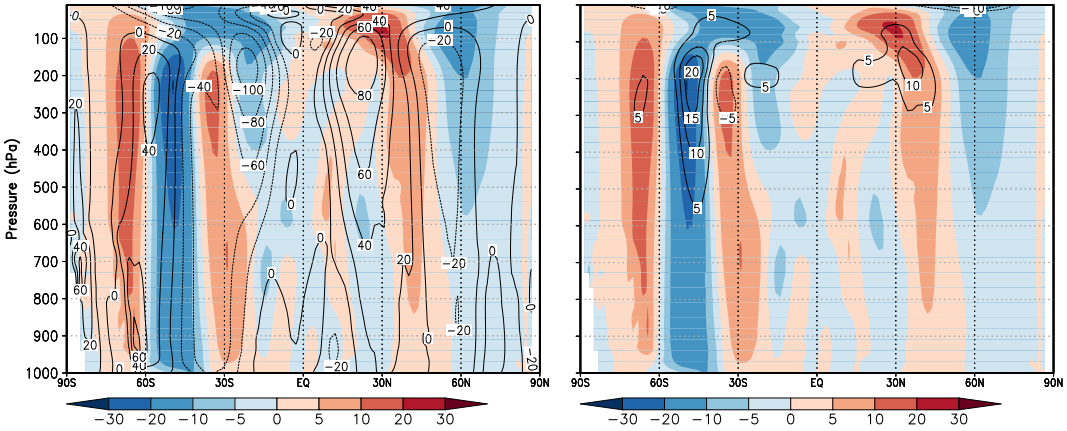

Figure 3.20: Vertical cross-section of the latitudinal shear in u, i.e., $\cos\phi \frac{\partial([\langle u \rangle]/\cos\phi)}{\partial\phi}$, in CTRL (contours,left panel), and its change in UP (color shaded, both panels), in m s^{-1}. Vertical cross-section of the changes in $C(K_e, K_m)$ in UP with respect to CTRL (contours, right panel), in 10^{-5} W m^{-2}.

to CTRL, and comparing this with the changes in $C(K_e, K_m)$ (Fig. 3.20). We compute the latitudinal shear of $[u]$ as $\cos\phi^{(\partial([\langle u \rangle]/\cos\phi))}/_{\partial\phi}$, but we refer to it simply as $d[u]/d\phi$. Note that $d[u]/d\phi$ in CTRL (contours in left panel of Fig. 3.20) is always positive in the southward flank of the jets, zero where the jet is strongest, and negative on the northward flank of the jets, as expected. This makes this plot antisymmetric with respect to the equator, and therefore its changes (color shaded), are also antisymmetric. The strongest changes in each hemisphere are therefore of opposite sign: a decrease in the Southern Hemisphere around 50°S, and an increase in the Northern Hemisphere around 50°N that extends upward and southward. In both cases they imply a poleward displacement of the jets. The changes in $C(K_e, K_m)$ match very well with these two regions of maximum change in $d[u]/d\phi$ (Fig. 3.20, right panel). In other words, we can be very confident that the response of $C(K_e, K_m)$ in UP and in FULL (in SFC there is almost no change in this term) is due to changes in the horizontal shear of the mean flow, hence to changes in barotropic instability.

The fact that $C(K_e, K_m)$ is related to barotropic processes, whereas $C(P_m, P_e)$ and $C(P_e, K_e)$ are related to baroclinic processes, explains why $C(K_e, K_m)$ responds in a different way. Regarding baroclinicity, the tropical upper-tropospheric warming has two opposite effects: first, it increases the meridional temperature gradient (which favors baroclinicity), and second, it increases static stability (which suppresses baroclinicity). We have shown in the previous subsection that this static stability effect is responsible for the global decrease in baroclinicity. Regarding barotropic instability, thermal wind balance implies that the tropical upper-tropospheric warming must be accompanied by stronger subtropical jets (seen as a strong increase in K_m in UP and FULL). This strengthening of the jets implies stronger wind shear, which increase barotropic instability in the jet regions. As opposed to baroclinicity, barotropic instability does not depend on static stability (Williams, 2006), and therefore $C(K_e, K_m)$ in-

creases in the UP experiment—and also in the FULL experiment—regardless of a more stable atmosphere.

The first two terms of $C(K_e, K_m)$ are clearly describing such barotropic processes, where horizontal momentum eddy fluxes take place along regions of horizontal shear of the mean flow (see Eq. (A.4) and table 3.1). In fact, the above analysis regards mainly the first term, which is proportional to $d[u]/d\phi$, and whose response is the largest of all. Combining the changes of the first two terms accounts for two thirds of the total response of $C(K_e, K_m)$. The third and fourth terms are related to a vertical shear of the mean flow. Although this does not imply that they are not related to barotropic processes, we cannot exclude the possibility that they are also affected by baroclinic processes. In principle, they could reflect a mixture of baroclinic and barotropic processes. We can focus on the third term, because the fourth one is very small, and shows practically no change in any of the experiments. Note that the third term increases by 0.026 W m^{-2} in UP and by 0.013 W m^{-2} in SFC. As we will see later, SFC is characterized by an increase in baroclinic activity, whereas UP is characterized by a decrease in baroclinic activity. This suggests that the increase in this term in the UP experiment is not due to changes in baroclinicity. Otherwise, we would find a stronger change in the SFC experiment and not a weaker change, as we find. Therefore, although we cannot exclude the possibility that baroclinic processes affect this third term related to vertical wind shear, we can infer from our results that it is barotropic processes that dominate its response in the UP experiment. The fifth term, which is the smallest of all, arises from the *curvature effect* term of the momentum equation (Holton, 2004), and is clearly negligible.

We can conclude that the increase in $C(K_e, K_m)$ is a direct consequence of the stronger wind shear along the intensified subtropical jets. Because barotropic instability does not depend on static stability, this increase of wind shear along the jets is sufficient to explain this response.

4. Change in $C(P_m,K_m)$ – changes in meridional overturning circulations

The importance of the eddies in the atmosphere's "heat engine" has been stressed since the formulation of the LEC by Lorenz (1955), and is confirmed by observations (e.g., Peixoto and Oort, 1974; Oort and Peixoto, 1974) and model data (Boer, 1995; Boer and Lambert, 2008; Hernández-Deckers and von Storch, 2010). That is, the main path for the conversion of P into K in the LEC is along $P_m \rightarrow P_e \rightarrow K_e \rightarrow K_m$, where most of the energy conversions take place. Globally, the direct conversion rate from P_m to K_m is very small, and most estimates indicate that it is slightly negative, indicating a small net conversion of K_m into P_m. This term describes the conversion between P_m and K_m. It is positive in the case of rising of relatively warm air and sinking of relatively cold air in zonal mean circulations, i.e., in meridional overturning circulations. Therefore, P_m is converted into K_m in the Hadley and polar cells, while K_m is converted into P_m in the indirect Ferrel cells. Despite its small global value, we do observe changes in this term in our different experiments that are comparable to the changes in other conversion terms (a decrease of 0.07 W m^{-2} in FULL and of 0.08 W m^{-2} in UP rel-

ative to CTRL). However, the global value of $C(P_m, K_m)$ cannot give us much information about the cause or causes for this change. The only way to visualize this is through the vertical cross-sections. To facilitate this analysis to the reader, we show here once more the vertical cross-section of $C(P_m, K_m)$ (Fig. 3.21).

The contours in Figure 3.21 reveal that positive contributions of $C(P_m, K_m)$ are located at low latitudes—in the upward branch of the Hadley Cell—with slightly higher values in the NH, and in very high latitudes—corresponding to the polar cells—with higher values in the SH. Negative contributions are seen in the Ferrel cells (around 60°N and 60°S), and are much stronger in the SH than in the NH. There are also two symmetric regions with slightly negative contributions just equatorward of 30°N and 30°S, which would correspond to the descending branches of the Hadley Cell. The net conversion corresponding to the Hadley Cell—between 30°N-30°S—is mostly positive. The net negative value of $C(P_m, K_m)$ is due to the strong negative contribution of the SH Ferrel cell.

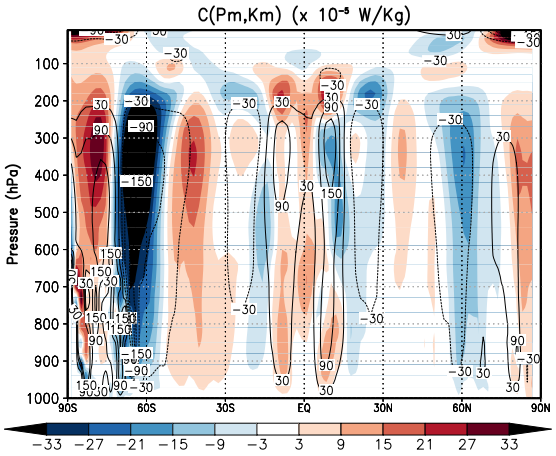

Figure 3.21: Vertical cross-section of $C(P_m, K_m)$ in CTRL (contours) and its change in the UP experiment (color shaded). Units are 10^{-5} W m^{-2}.

Regarding the changes in the UP experiment, Figure 3.21 suggests that there is in general a strengthening in every feature, i.e., the positive contributions tend to increase, while the negative contributions tend to decrease. The dominant response in the UP experiment, which is responsible for the decrease in the global value of $C(P_m, K_m)$ from -0.09 W m^{-2} to -0.17 W m^{-2}, is the strong decrease in the conversion in the SH Ferrel cell, around 60°S. That is, more conversion from K_m to P_m. This suggests a stronger Ferrel Cell, which is generally associated with stronger baroclinicity (Williams, 2006). This may seem contradictory, considering the global decrease in baroclinicity in the UP experiment. Nevertheless, this strengthening of the Ferrel cell may correspond to a more local baroclinic response. We noted that even though the global baroclinicity decreases, there is an increase in baroclinicity above 200 hPa and also near the surface around 60°S and 60°N. The vertical cross-section of $C(P_e, K_e)$ (Fig. 3.11) shows that the increase response around 200 hPa extends downward along a narrow band slightly poleward of 60°S. This same feature is more pronounced in the plots of σ_{eady} and BP (Fig. 3.18), and would therefore suggest that although there is a global decrease in baroclinicity, around 60°S there is a more localized increase that may manifest in terms of a stronger Ferrel cell.

Furthermore, this local increase in baroclinicity could be linked to the coupled feedback process over the Southern Ocean that tends to maintain the latitudinal gradient over this region (Fyfe and Saenko, 2006; von Storch, 2008). We had pointed out this process in Chapter 2

in the context of the transient experiments. This process explains the slower warming rate of the SH compared to the NH that causes a stronger north-south asymmetry in the transient energetics response compared to the equilibrium 2xCO_2 response. Although we are dealing here with equilibrium and not transient experiments, this process could still be causing a stronger meridional temperature gradient in this region, but now more locally than in the transient experiments. This possible connection motivates further research regarding this coupled ocean-atmosphere feedback, but is out of the scope of this work.

We can conclude that the dominating response of $C(P_m, K_m)$ is an increase of the K_m-to-P_m conversion in the SH around 60°S, which suggests a strengthening of the SH Ferrel cell. This strengthening could be related to a local increase in baroclinicity around 60°S. Surprisingly, this would imply that an increase in baroclinicity, which means stronger P_e-to-K_e conversion and therefore a strengthening of the LEC, would at the same time cause a weakening of the LEC by strengthening the K_m-to-P_m conversion in the Ferrel cells. In our case, however, both effects contribute to the weakening of the LEC because there is a *local* increase in baroclinicity around the SH Ferrel cell embedded in a global decrease in baroclinicity. Thus, both features work in the same direction in terms of the global LEC strength. However, without a detailed knowledge about the exact relationship between the conversion rate $C(P_m, K_m)$ and the meridional overturning circulations, it is not possible to fully verify and understand this feature.

5. Changes in energy reservoirs, in particular K_e – extratropical storm activity.

Although the energy reservoirs do not provide a measure for energetic activity as the conversion rates do, they can provide information about the state of the atmosphere. In particular, the eddy kinetic energy reservoir (K_e) is an indicator of extratropical storm activity because it quantifies the average amount of energy in the perturbations of the wind field. Several studies quantify the extratropical storm activity in different situations (e.g., Geng and Sugi, 2003; O'Gorman and Schneider, 2008; Bengtsson et al., 2009; Lim and Simmonds, 2007, 2009). Their general approach consists of using specific measures that identify and characterise storms (like their strength in terms of wind speed, pressure difference, their radius, etc.), and then use them to track specific events and carry out a statistical analysis. Of course, high resolution data—in either observations or model output—is important in order to obtain reliable conclusions. Our methodology, as well as our model runs, were not designed with such an objective. Nevertheless, we provide a global view of the large scale changes in K_e due to different warming patterns, without performing a detailed analysis of storm activity. This should serve as a fundamental background for other more detailed studies.

Looking back at our results with the FULL experiment (also valid for the 2xCO_2 experiment), we can see that there is not a clear global response in K_e. There is an overall weakening of the LEC, but K_e remains almost unchanged. By separating the warming pattern into UP and SFC, we now find a more consistent response in K_e. Figure D.1 in Appendix D shows

the values of all the LEC terms in CTRL and UP. K_e decreases from 8.05 $\times 10^{-5}$ J m^{-2} in CTRL to 7.56 $\times 10^{-5}$ J m^{-2} in UP. Once we isolate the tropical upper-tropospheric warming, we indeed observe that the weakening of the LEC is accompanied by a reduction in the K_e reservoir. The vertical cross-section of K_e (bottom right panel in Fig. 3.11) shows that this decrease is happening throughout the whole troposphere. There is only a strengthening above 200 hPa, which would suggest an upward shifting in combination with the overall weakening.

In conclusion, due to the UP warming pattern, K_e decreases globally, suggesting a global decrease in extratropical storm activity. However, we cannot derive from this any detailed characteristics, like changes in frequency, intensity, extreme values, etc. Furthermore, this result does not necessarily imply that tropical storms would decrease *everywhere* due to this idealized warming pattern, but only on average. For example, in point 4 above, we found that there is a region of increased baroclinic activity in the high southern latitudes, in agreement with the results obtained by Lim and Simmonds (2009) with a similar warming pattern. Nevertheless, such a local response does not show up here in terms of K_e.

Regarding the reservoir of zonal-mean kinetic energy (K_m), it also provides information about the mean state of the atmosphere, which has specific consequences. For example, we have described above how the strengthening of the jets, which reflects as a strong increase in K_m, implies stronger barotropic instability, increasing the K_e-to-K_m conversion. It is also closely related to the intensity of the tropical upper-tropospheric warming due to thermal wind balance. In the context of our study, the importance of the changes in K_m has been already highlighted in terms of the barotropic response of $C(K_e, K_m)$.

3.3.4 The high-latitude, surface warming (SFC)

In this subsection we will analyse the response of the SFC experiment, where the warming pattern consists of a strong warming in the high-latitudes near the surface, with a stronger warming in the NH (see lower right panel of Figure 3.1). In subsection 3.3.2 we have already mentioned the principal features of the energetics response of this experiment. We will now analyse them in 4 steps, which correspond to the following responses of the LEC in this case:

1. Change in strength in the 2-box LEC ($C(P, K)$).
2. Changes in the conversion terms $C(P_m, P_e)$ and $C(P_e, K_e)$ (baroclinic response)
3. Changes in $C(P_m, K_m)$ (response of merdional overturning circulations)
4. Changes in the energy reservoirs, in particular K_e, an indicator of extratropical storm activity.

1. Change in strength in 2-box LEC

The global response in SFC in terms of the LEC-strength is a clear increase, as opposed to the response in FULL and UP. Figure 3.9 shows that $C(P, K)$ increases by 0.09 W m^{-2}, i.e.,

3.8% relative to CTRL. The strengthening in this case is restricted to the upper region (above 340 hPa), where $C(P, K)$ increases by 0.14 W m^{-2} (see Fig. 3.13). In the lower region we find a slight decrease in strength, of 0.05 W m^{-2}. This dual response reminds us about the FULL (or 2xCO_2) response, but now the strengthening response in the upper region is stronger than the weakening response in the lower region, and dominates in the global LEC. Knowing now that the effect of the UP warming pattern is only a weakening of the LEC, we can conclude that the strengthening of the LEC in the upper region due to the combined, 2xCO_2-like warming pattern is a consequence of the high-latitude surface warming.

2. Changes in C(P_m,P_e) and C(P_e,K_e) – baroclinic response

From the 4-box LEC (Fig. 3.9 lower right panel) we can see that the global strengthening of the LEC in SFC is exclusively due to the increase in $C(P_e, K_e)$, while $C(P_m, K_m)$ does not change. The increase in $C(P_e, K_e)$ is clearly connected to the increase in $C(P_m, P_e)$, and can be tracked back again to the change in G_m. These changes clearly reflect that this strengthening response is driven by the changes in G_m, which then extend to $C(P_m, P_e)$ and $C(P_e, K_e)$. As opposed to the case of UP, this indicates an increase in baroclinic activity. We will first understand this response in terms of the LEC, before looking at it in terms of changes in baroclinicity.

The relative change in the vertical profile of γ (Fig. 3.17, left panel) reveals that except for the region between the surface and 900 hPa, where γ slightly decreases, there is an increase throughout the whole troposphere. This is a completely different profile of change compared to FULL and UP, where γ decreases throughout the troposphere. However, the profile of change of P_m (Fig. 3.17, right panel) in SFC is closer to the one in FULL than the one in UP is. In SFC, P_m decreases with a similar magnitude as in FULL from the surface up to about 500 hPa. This, in contrast with the increase in γ throughout the whole troposphere, implies that the changes in P_m obey more to the changes in the horizontal temperature variance than to the changes in γ. The profile of relative change in γ seems to modulate slightly the P_m-relative change profile—note how the curvature of both profiles match from the surface up to around 300 hPa—but having a different sign, the main response of P_m must be determined by the changes in horizontal variance of temperature. On the other hand, G_m, which we know is the driving term for the changes in strength in the LEC, must be more sensitive to changes in γ than to the changes in $[\langle T\rangle]''[\langle Q\rangle]''$ because it increases in both the upper and the lower region, instead of decreasing, as P_m does. Just as in UP, we can conclude from this that the changes in γ are the main drivers for the changes in strength of the LEC. In this case, the surface warming causes γ to increase throughout most of the troposphere, i.e., the atmosphere becomes less stable. This drives then a strengthening of the energetics that manifests itself mostly in the upper region, above 340 hPa.

In the same way as with UP, we can intuitively understand why the changes in mean static stability determine the change in strength of the LEC. Due to the surface warming in SFC, the

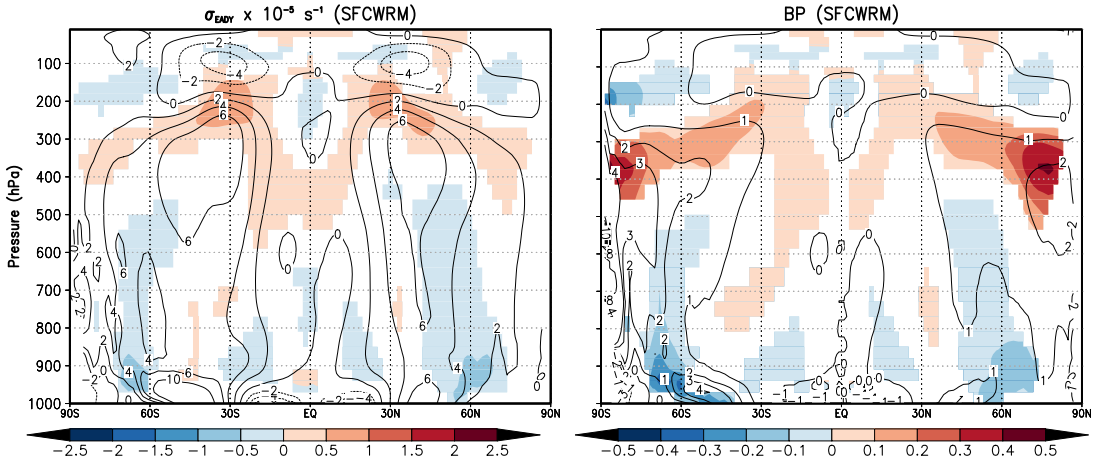

Figure 3.22: Zonal mean plots of σ_{eady} (left panel) and BP (right panel) in CTRL (contours), and their change in SFC (color shaded). Only differences with 95% significance level are shown, based on a standard t-test. Units are 10^{-5} s^{-1} for σ_{eady}, BP is dimensionless.

atmosphere becomes less stable, favoring vertical motions. These vertical motions are essential for the conversion of available potential energy into kinetic energy—rising of relatively warm air and sinking of relatively cold air.

Coming now to baroclinic activity, we can argue that the strengthening of $C(P_m, P_e)$ and $C(P_e, K_e)$ imply an increase in baroclinicity. Just as before, we can evaluate changes in σ_{eady} and in BP (Fig. 3.22) in order to verify this hypothesis. Just as in the vertical cross-sections of the conversion terms (Fig. 3.12), we find an increase response in the upper troposphere an a

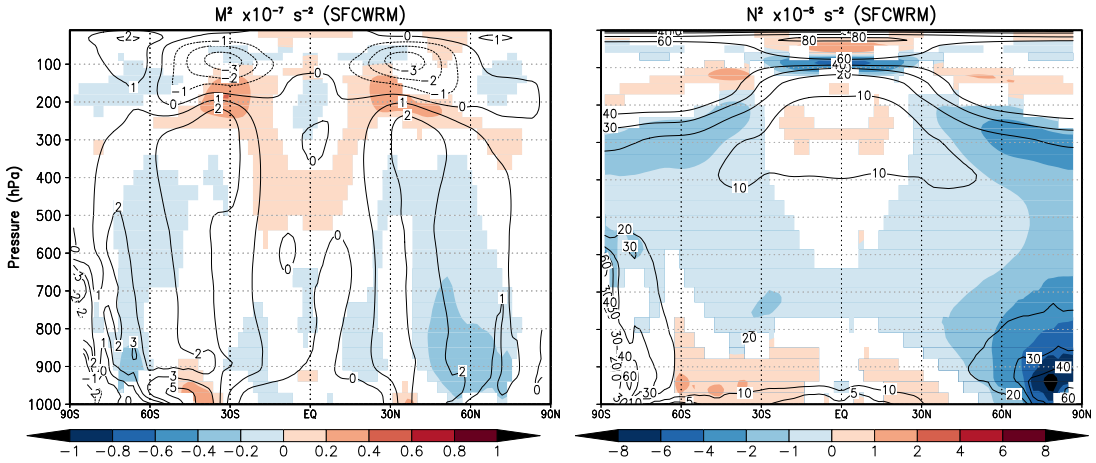

Figure 3.23: Zonal mean plots of M^2 (left panel) and N^2 (right panel) in CTRL (contours), and their change in SFC (color shaded). Only differences with 95% significance level are shown, based on a standard t-test. Units are 10^{-7} s^{-2} for M^2, and 10^{-5} s^{-2} for N^2.

weakening below in both σ_{eady} and BP. Once again, the pattern of σ_{eady} is clearly determined by the pattern of M^2 (Fig. 3.23, left panel). This means that changes in baroclinicity, as estimated with σ_{eady}, are mainly related to changes in the meridional temperature gradient.

On the other hand, BP has a pattern similar to σ_{eady}, but with a stronger increase response in the upper troposphere that stands out very clearly from the rest of the pattern. In σ_{eady} both responses (increase above and decrease below) have similar magnitudes, and neither of them seems to dominate the overall response. Therefore, the BP-response shows more consistency than the σ_{eady}-response with the responses of $C(P_m, P_e)$ and $C(P_e, K_e)$, where the strengthening in the upper troposphere dominates. It is the stronger dependence of BP on N^2 what causes the difference between BP and σ_{eady}. In this case, N^2 decreases throughout most of the troposphere, especially in the northern hemisphere (Fig. 3.23, right panel). Due to the surface warming, static stability decreases. In particular, there is a relative maximum in the decrease response of N^2 around 300 hPa along the mid and high-latitudes of both hemispheres that enhances the increase in baroclinicity due to changes in M^2 in this region. On the contrary, the strong maximum in decrease of N^2 in the high northern latitudes near the surface has little effect locally, probably due to the opposite effect of M^2 in this region (note that BP is proportional to M^2, but inversely proportional to N^2). In the upper troposphere, both M^2 and N^2 change in such a way as to favor baroclinicity. Hence, it is the inclusion of the mean static stability effect on baroclinicity what makes the BP-response consistent with the changes in $C(P_m, P_e)$ and $C(P_e, K_e)$ in the SFC experiment. We can conclude from this that due to the overall decrease in mean static stability in the SFC experiment, baroclinicity is enhanced in the upper troposphere, and the strong decrease that would result from the reduction in M^2 in the lower troposphere is partly counteracted. Hence, changes in mean static stability are necessary to explain the strengthening of the conversion terms $C(P_m, P_e)$ and $C(P_e, K_e)$, also in terms of baroclinicity.

3. Changes in $C(P_m, K_m)$ – response of merdional overturning circulations

The global response of $C(P_m, K_m)$ in the SFC experiment is very small. It changes from -0.09 W m^{-2} in CTRL to -0.10 W m^{-2} in SFC. However, like in UP, the vertical cross-section of this conversion term (Fig. 3.24) reveals more features. Clearly, the magnitude of the changes in SFC is smaller than in UP (Fig. 3.21), and the strongest change is not in the SH Ferrel cell but in the Hadley cell region. Even though the net change is close to zero, there is a strong increase in the upward branch of the Hadley cell, near the maximum positive values of $C(P_m, K_m)$, and a decrease in the poleward side of the cell, which covers partly the regions of negative values and partly the regions of positive values. In other words, the region of positive contribution near the equator becomes stronger but narrower, while the regions of negative contributions become slightly stronger and maybe broader. The fact that this feature also appears in the FULL experiment (see Fig. 3.6) indicates that changes in static stability are not responsible for this, but most likely changes in the horizontal temperature distribution.

In principle, one would expect that these changes in $C(P_m, K_m)$ should also imply changes in the Hadley cell dynamics. Unfortunately, we do not know exactly how these two quantities are related. Most climate models predict a weakening and broadening of the Hadley cell with global warming (e.g., Vecchi and Soden, 2007; Lu et al., 2007). However, it is not clear how this could relate to changes in the P_m-to-K_m conversion rate, and such a relationship does not emerge from our analysis either. On the other hand, according to our model results, the net effect in the changes in this conversion rate at low latitudes is negligible, so that even if we could establish a connection with Hadley cell dynamics, although interesting on its own, this would be out of the scope of this work. In any case, further research regarding the connection between $C(P_m, K_m)$ and the zonal-mean meridional overturning circulations could help decipher the mechanisms behind this feature, which although does not affect the global energetics, could be important in terms of Hadley cell dynamics.

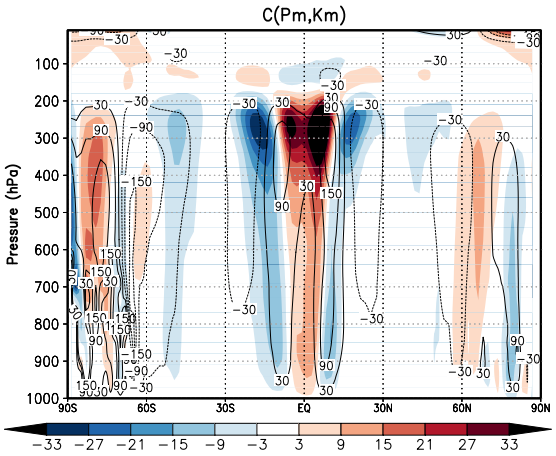

Figure 3.24: Vertical cross-section of $C(P_m, K_m)$ in CTRL (contours) and its change in the SFC experiment (color shaded). Units are 10^{-5} W m^{-2}.

4. Changes in energy reservoirs, in particular K_e – extratropical storm activity.

In terms of the energy reservoirs, the largest relative change we find in the SFC experiment is in K_e. It increases from 8.05×10^5 J m^{-2} in CTRL to 8.43×10^5 J m^{-2} in SFC, i.e., a 5% increase. This is consistent with the overall increase in energetic activity we find in this experiment, as well as with the corresponding increase in baroclinicity. It suggests an increase in the extratropical storm activity, although, as we pointed out earlier, we cannot derive from this any details about specific or local characteristics of this response. We can only tell that globally averaged, extratropical storm activity increases when the warming is concentrated near the surface and at high-latitudes.

It is worth noting here that the response of K_e in UP and SFC is completely opposite. This explains why in FULL (or in the 2xCO$_2$ experiment) there is no clear change in K_e. The combination of the two features of the warming pattern produces a very small net change on K_e, and the sign of this change is very sensitive to the relative magnitude of the tropical upper-tropospheric and the high-latitude surface warmings. This highlights the importance of understanding the processes that contribute to each feature of the warming pattern, because small differences could imply opposite responses in terms of extratropical storm activity.

In terms of the K_m, there is no clear change, as opposed to what happens in the UP and

the FULL experiment. This explains why in this experiment there is no important increase in $C(K_e, K_m)$. Because the jets are not strengthened, there is no change in the wind shear in the jet regions, i.e., no changes in barotropic instability.

3.4 Conclusions and discussion

The aim of this chapter is to understand how the 2xCO_2 warming pattern alters the energetics of the atmosphere. We have done this with the coupled atmosphere-ocean ECHAM5/MPI-OM model by calculating the energetics responses that separately result either from the tropical upper-tropospheric warming or from the high-latitude surface warming. Here we summarize and discuss the main results obtained with these simulations.

In this section, we will often refer to the tropical upper-tropospheric warming simply as the *upper warming*, and to the high-latitude surface warming as the *surface warming* in order to make the text less intricate. Nevertheless, the latitudinal characteristics of these warming patterns must always be kept in mind.

First of all, we were able to reproduce the 2xCO_2 energetics response of the atmosphere by forcing the model—through temperature-nudging—with the total zonal-mean 2xCO_2 warming pattern, obtaining a "2xCO_2-like" experiment (FULL). This takes us to the first conclusion:

1. The 2xCO_2 energetics response is a consequence of the corresponding zonal-mean warming pattern that consists of two main features: the tropical upper-tropospheric warming, and the high-latitude surface warming.

In the previous chapter we were able to make a qualitative connection between the warming pattern and the energetics response. However, the "2xCO_2-like" temperature-nudged experiment, which reproduces almost exactly the 2xCO_2 energetics response, confirms that the warming pattern drives the energetics response.

By carrying out additional temperature-nudged experiments in which the two main features of the warming pattern are simulated separately—UP, with only *upper warming* and SFC, with only *surface warming*—we were able to identify specific energetics responses for each warming pattern. Furthermore, we verified that these separate responses combine approximately linearly to produce the total, 2xCO_2-like response. This assures that the following conclusions, even though obtained from separate warming pattern simulations, extend to the combined, 2xCO_2 warming pattern response. The main findings are:

2. The global energetics response to the *upper warming* is a 10% weakening of the Lorenz Energy Cycle (LEC). The response to the *surface warming* is opposite: the LEC strengthens by 4%. The net effect of the combined response (2xCO_2-like) is a 5% weakening of the LEC. This reflects the high linearity in the combination of the effects of the two warming patterns.

This means that globally, due to the *upper warming* there is less conversion of available potential energy into kinetic energy per unit of time, whereas due to the *surface warming* the opposite is true. Held (1993) noted the competing effects that these two features of the warming pattern would have in terms of their changes in meridional temperature gradient, and hence in baroclinicity and eddy activity. He argues that the tropical upper-tropospheric warming would imply stronger energetic activity because it increases the meridional temperature gradient above, whereas the high-latitude surface warming would do the opposite, because it decreases the meridional temperature gradient below. Our results indicate that these competing effects actually work the other way around, suggesting that it is not their effect on the horizontal temperature gradients, but rather their effect on the vertical temperature distribution that dominates in terms of the global energetic activity.

3. Changes in static stability—and not in the horizontal temperature distribution—due to each warming pattern are the main drivers for altering the baroclinic part of the LEC. That is, the conversion rates between zonal mean available potential energy (P_m), eddy available potential energy (P_e), and eddy kinetic energy (K_e). Furthermore, the changes in these conversion rates are accompanied by corresponding changes in the K_e reservoir, an indicator of extratropical storm activity.

Due to the *upper warming*, static stability increases globally, consistent with a general weakening in baroclinicity. Due to the *surface warming*, static stability decreases globally, consistent with an increase in baroclinicity. The static stability effect of the *upper warming* is stronger than that of the *surface warming*, which explains why in 2xCO_2 case the net effect is still a weakening of the baroclinicity-related terms of the LEC. Furthermore, the two responses in terms ofK_e almost cancel each other in the combined 2xCO_2-like experiment, such that little change is seen in K_e. This suggests that the change in storm activity is very sensitive to the specific features of the warming pattern, making it difficult to determine with certainty.

The warming-induced changes in these baroclinicity-related terms, in particular in the conversion rate between P_e and K_e, dominate for setting the total strength of the LEC. According to our results, it is the changes in mean static stability that determine if the global LEC becomes stronger or weaker. In terms of the LEC, the response in each case (weakening due to the *upper warming* and strengthening due to the *surface warming* is strongest in G_m, the generation rate of P_m, suggesting that G_m is the driving term for the LEC-changes. Even though we cannot calculate G_m directly here, our results suggest that its changes are more sensitive to changes in mean static stability than to changes in horizontal temperature distribution. This hypothesis is further supported by a baroclinic analysis, which indicates that each response has a corresponding change in baroclinicity, which in turn is mainly due to changes in static stability.

Previous studies (e.g., Boer, 1995; Marquet, 2005) have attributed the net decrease in energetic activity in the lower troposphere when doubling CO_2 mostly to the reduction in meridional temperature gradient and in land-sea contrasts during the winter season. Although this

reasoning may be valid at specific regions near the surface and for specific seasons, we show here that when globally averaged, it is the changes in static stability which drive this weakening. Otherwise, we should find a strengthening in baroclinicity due to the *upper warming*, and a weakening due to the *surface warming*. The fact that the maximum Eady growth rate (σ_{eady})—a widely used measure of baroclinicity—is highly dependent on the meridional temperature gradient and does not depend so strongly on static stability, may have contributed to this generalized way of thinking. σ_{eady} is based on strong approximations, which may be most appropriate in simple cases. Based on our results, we agree with Lim and Simmonds (2009) (but in our case in a more global sense) that a better measure of baroclinicity is the *baroclinic parameter* (BP) (Section 3.3.3), mainly because of its stronger dependence on static stability. This dependence makes BP more consistent than σ_{eady} with the changes in the baroclinicity-related LEC-terms. Recent studies also stress the importance of static stability effects in terms of baroclinicity and energetic activity (e.g., O'Gorman and Schneider, 2008; Lim and Simmonds, 2007, 2009). We now find that static stability is the driving mechanism for changes in the global energetics of the atmosphere.

4. Due to the *upper warming*, the K_e-to-K_m conversion rate increases by 9%. This increase response is linked to an increase in barotropic instability caused by stronger horizontal wind shear. This stronger wind shear is a consequence of stronger jets that result from the *upper warming* and thermal wind balance.

The fact that this conversion rate between K_e and K_m ($C(K_e, K_m)$) is related to barotropic instability and not to baroclinic instability, explains why it is the only conversion term that increases due to the 2xCO_2 and the *upper warming* patterns, a feature that at first sight seems puzzling. The terms related to baroclinic instability decrease because the mean static stability weakens them. On the other hand, barotropic instability depends not on mean static stability but only on the horizontal wind shear, so that $C(K_e, K_m)$ is increased by the stronger jets. Even though this response does not impact conversion rates between P and K, it indicates an important change in the state of the system, by increasing the reservoir of K_m. Furthermore, the strengthening of the subtropical jets is not an ECHAM5-only feature. It is a well established prediction of current climate models due to global warming (Lorenz and DeWeaver, 2007; Fyfe and Saenko, 2006), and a clear consequence of the increase in meridional temperature gradient due to the *upper warming*.

5. The *upper warming* leads to a strengthening of the K_m-to-P_m conversion rate in the region of the Southern Hemisphere Ferrel cell, suggesting a strengthening of this cell. A stronger Ferrel cell would imply stronger baroclinic activity along the cell, despite the global decrease in baroclinicity due to the *upper warming*. Further research about the exact relationship between zonal-mean meridional overturning circulations and this conversion rate between P_m and K_m would help to verify and fully understand this feature.

If this strengthening of the K_m-to-P_m conversion rate is indeed related to a local increase in baroclinicity along the Southern Hemisphere Ferrel cell as our results suggest, it would imply a rather surprising feature: stronger baroclinic activity would not only increase the total P-to-K conversion rate (through the P_e-to-K_e conversion rate), but it would also decrease it by means of a higher K_m-to-P_m conversion rate along a stronger Ferrel cell. However, in our results this feature operates in such a way that it decreases the total P-to-K conversion rate through both sides of the LEC, because it brings together a global decrease in baroclinicity—that decreases the P_e-to-K_e conversion rate—and a local increase in baroclinicity along the Southern Hemisphere Ferrel cell—that increases the K_m-to-P_m conversion rate, hence a decrease in the P_m-to-K_m conversion rate. This could in turn also be related to the coupled atmosphere-ocean feedback that tends to maintain the meridional temperature gradient along the Southern Ocean (Fyfe and Saenko, 2006; von Storch, 2008), and is responsible for the slower warming of the Southern Hemisphere compared to the Northern Hemisphere in transient experiments (see Section 2.1, and Hernández-Deckers and von Storch (2010)). Although these are not transient experiments, this effect could still be affecting the energetics in a more localized way. Nevertheless, further research would be needed to confirm this.

On the other hand, the *surface warming* causes this same conversion term ($C(P_m, K_m)$) to respond with a particular pattern along the Hadley cell. The net effect of this pattern in terms of the energetics is negligible, but we believe that it may as well indicate changes in the Hadley cell characteristics. Our present analysis does not offer any hypothesis regarding this response in the Hadley cell. Just as with the response related to the Ferrel cell, further research is needed in order to elucidate the mechanisms behind this feature, which although may not be relevant from the point of view of the global energetics of the atmosphere, could be important in terms of global circulation dynamics.

Chapter 4

Conclusions and outlook

We have studied the atmospheric energetics response to higher CO_2 concentrations using the coupled atmosphere-ocean ECHAM5/MPI-OM model. By studying this response, we believe that we not only acquire a better understanding of the consequences of global warming, but we also contribute to a better understanding of the mechanisms that drive the atmosphere's heat engine. The conclusions below summarize this understanding of the Earth System from this fundamental point of view.

Chapter 2 describes how the energetics of the atmosphere, in terms of the Lorenz Energy Cycle, respond to higher CO_2 concentrations in the coupled atmosphere-ocean ECHAM5/MPI-OM model. Therefore, the results of this chapter answer our first research question (conclusions 1 to 3 below):

- *What is the response of the atmospheric energetics to higher CO_2 concentrations?*

These results from Chapter 2 also provide important indications about our second research question, which regards the mechanisms behind the energetics responses. However, it is with our results from Chapter 3 that we obtain a clear answer for our second research question (conclusions 4 to 7 below):

- *What are the mechanisms that cause the atmospheric energetics response to higher CO_2 concentrations?*

4.1 Conclusions

Using the coupled atmosphere-ocean ECHAM5/MPI-OM model, we analysed the energetics response of the atmosphere in transient simulations with increasing CO_2 concentrations, and with stabilized 2xCO_2 concentrations, compared to pre-industrial values. We found that:

1. *Doubling CO_2 concentrations causes a global weakening of 4% to 7% in the Lorenz Energy Cycle. That is, there is less conversion of available potential energy (P) into kinetic energy (K) in the global atmosphere per unit of time.*

In the coarse resolution experiment, this weakening is of approximately 7%, and in the higher resolution experiment, of 4%. The difference between the two resolutions is attributable to the difference in the magnitude of the warming, which is slightly stronger in the coarse resolution experiment. This general weakening is the result of two opposite responses: a strengthening of the Lorenz Energy Cycle in the upper troposphere, and a weakening in the lower and middle troposphere, which dominates when considering the globally-integrated Lorenz Energy Cycle. Our results with the $2xCO_2$ experiments suggest that this dual response is closely related to the $2xCO_2$ warming pattern, which is characterized by two features: the tropical upper-tropospheric warming and the high-latitude surface warming.

2. *The transient response, when CO_2 concentrations increase by 3% per year during 10 years, is consistent with the $2xCO_2$ response, but is less north-south symmetric than the equilibrium response due to the stronger north-south asymmetry in the warming pattern.*

This stronger north-south asymmetry results from the fact that the Southern Hemisphere warms slower than the Northern Hemisphere, likely due to a coupled feedback process that tends to maintain the latitudinal temperature gradient over the Southern Ocean (e.g., Fyfe and Saenko, 2006; von Storch, 2008). This makes the weakening response of the Lorenz Energy Cycle in the Southern Hemisphere less pronounced than in the Northern Hemisphere in the transient experiments.

The $2xCO_2$ response is consistent in two different model resolutions (T31L19 and T63L31). Furthermore, we performed an additional stationary and transient eddy decomposition with the higher resolution version of the model. From this analysis we can conclude:

3. *The largest contribution to the energetic activity and to its $2xCO_2$-response in the Lorenz Energy Cycle is supplied by the transient eddy components. The $2xCO_2$-response of the stationary eddy components reveal a pattern of stronger warming over the subtropical desert regions relative to their corresponding zonal belts, but has no global effects in terms of the energetic activity.*

By carrying out additional experiments in which instead of increasing CO_2 concentrations we apply artificial diabatic heating patterns through temperature-nudging, we reproduce the $2xCO_2$-response, and we simulate the effects of the two main features of the $2xCO_2$ warming pattern separately. That is, one in which only the tropical upper-tropospheric warming is present, and another one in which only the high-latitude surface warming is present. We find that:

4. *The $2xCO_2$ energetics response is a consequence of the corresponding zonal-mean warming pattern that consists of two main features: the tropical upper-tropospheric warming, and the high-latitude surface warming.*

By comparing the experiments with the separate features of the 2xCO_2 warming pattern to a control run, we identify the energetics responses of each of these warming patterns, which combine approximately linearly to produce the 2xCO_2 response. Therefore, although they are obtained for the separate warming patterns, they also apply to the combined, 2xCO_2 response.

5. *The weakening response of the Lorenz Energy Cycle in the lower and middle troposphere is a consequence of the tropical upper-tropospheric warming, whereas the strengthening response in the upper troposphere is due to the high-latitude surface warming. These two responses are driven by changes in static stability. The dominating static stability effect of the tropical upper-tropospheric warming explains the net weakening effect in the 2xCO_2 case. In contrast to previous authors' suggestions (e.g., Held, 1993; Boer, 1995), changes in horizontal temperature differences, such as land-sea contrasts and the pole-to-equator difference, are not as effective in producing global changes in energetics, as changes in mean static stability are.*

The tropical upper-tropospheric warming causes a weakening of about 10% in the LEC, whereas the high-latitude surface warming causes a strengthening of about 4%. These two responses, as well as the combined 2xCO_2 response are strongest in G_m, the generation rate of zonal-mean available potential energy (P_m), suggesting that this term drives the whole energetics response. Our results suggest that although G_m depicts the zonally-differential heating of the atmosphere, it is strongly modulated by mean static stability, and it is this dependence that drives these changes in G_m, hence in the overall energetic activity.

This is further confirmed in terms of changes in baroclinicity, which is the most important process involved in the total conversion rate of available potential energy into kinetic energy in the Lorenz Energy Cycle. Both responses—the weakening of the Lorenz Energy Cycle due to the upper warming and its strengthening due to the surface warming—appear together with a corresponding change in baroclinicity. These changes in baroclinicity can only be explained through changes in static stability, and are consistent with the baroclinicity measure given by the *baroclinic parameter* (see Subsection 3.3.3), which we find to be more realistic than the maximum Eady growth rate because of its stronger dependence on static stability. This response in baroclinicity, directly connected to the energetics response in terms of the Lorenz Energy Cycle, is accompanied by a corresponding change in the reservoir of eddy kinetic energy, an indicator of extratropical storm activity. This means that:

6. *On average, extratropical storm activity—as measured by the reservoir of eddy kinetic energy—decreases by 6% due to the tropical upper-tropospheric warming, but increases by 5% due to the high-latitude surface warming. Therefore, these two opposite responses approximately cancel each other in the 2xCO_2 case, showing almost no change there.*

It is important to note that these changes in eddy kinetic energy apply globally, but not necessarily locally. For example, we also find a region of increase in baroclinicity due to the tropical upper-tropospheric warming around the Southern Hemisphere Ferrel cell ($\approx 60°$S), embedded in the global decrease in baroclinicity. We detect this local change in the baroclinic parameter and in the maximum Eady growth rate, but not in eddy kinetic energy. However, we do find in this region an increase in the conversion rate of zonal mean kinetic energy into zonal mean available potential energy, which coincides with the Southern Hemisphere Ferrel cell. This would suggest a stronger Ferrel cell, consistent with the increase in baroclinicity in this region.

Finally, there is one more response of the Lorenz Energy Cycle to the tropical upper-tropospheric warming, which although does not affect the total conversion rate of available potential energy into kinetic energy, it does give information about the state of the atmosphere:

7. *Due to thermal wind balance, the tropical upper-tropospheric warming implies stronger jets, reflecting in a strong increase of 17% in the reservoir of zonal-mean kinetic energy (K_m). This in turn creates stronger horizontal shear in the mean flow, resulting in stronger barotropic instability. Hence, an increase of 9% in the K_e to K_m conversion rate.*

4.2 Outlook

We have obtained here a complete view of the atmospheric energetics response to higher CO_2 concentrations based on the coupled atmosphere-ocean ECHAM5/MPI-OM model. A similar analysis with other climate models would help in terms of further verification of our results. Additionally, different experiments with other climate forcings, for example very cold conditions, could also be helpful in order to verify if our results can be generalized even further.

Following Boer and Lambert (2008), the Lorenz Energy Cycle could be implemented as a common diagnostic for climate models, and used for model inter-comparison purposes. The fact that it involves first *and* second moment statistics of the prognostic variables implies that it reveals fundamental information about model performance, which cannot be captured by the first moment statistics only.

The process of eddy-mean flow interaction is not well represented in the Lorenz Energy Cycle. Although this process may not be as important for the atmosphere as a heat engine from a thermodynamical point of view, it is important in terms of the dynamics of the atmosphere. As far as we can tell with the Lorenz Energy Cycle, there does not seem to be an important global response of eddy-mean flow interaction to higher CO_2 concentrations. However, a more rigorous verification within the framework of the Transformed Eulerian Mean decomposition would be more conclusive.

We noted that the direct conversion rate between zonal mean available potential energy (P_m) and zonal mean kinetic energy (K_m) has in general a small contribution to the global energet-

ics, also in terms of the response to higher CO_2 concentrations. However, we know that this conversion rate is related to meridional overturning circulations in the atmosphere, but we do not know how these two processes are connected in detail. Based on this conversion rate, we found an indication of a stronger Ferrel cell in the Southern Hemisphere due to the tropical upper-tropospheric warming, which could also be related to a coupled ocean-atmosphere feedback over the Southern Ocean (e.g., Fyfe and Saenko, 2006; von Storch, 2008). We cannot fully understand this response without a more precise knowledge about the relationship between this conversion rate and the meridional overturning circulations. The same applies in terms of the Hadley cell response. We found a pattern of change in this conversion rate between P_m and K_m due to the high-latitude surface warming that would indicate changes in the Hadley cell, but without a detailed relationship between these two quantities, we cannot make a definitive statement regarding this. Although these responses are small in terms of the global energetics, studying these relationships in detail could be useful for understanding the dynamics of meridional overturning circulations from an energetic point of view.

We have contributed with a simple but fundamental explanation for the difficulty in detecting significant changes in extratropical storm activity. In a similar way as O'Gorman and Schneider (2008) point out, our results show that studying the changes in temperature distribution can give important clues about changes in extratropical storm activity. This highlights the importance of trying to reduce the uncertainties in predictions of the global warming pattern. Our results indicate that the strongest response, both in terms of the global energetics and storm activity, is due to the static stability changes in the tropical upper-tropospheric warming, whose magnigtude has a relatively large uncertainty due to its strong dependence on the moist convection parameterization schemes in climate models (Held, 1993; Schneider et al., 2010; Sherwood et al., 2010).

This brings out the importance of moisture in the energetics of the atmosphere, not only because it is the main cause for the tropical upper-tropospheric warming, but also in terms of the whole atmospheric energetics. Moisture is only included in an implicit way in the Lorenz Energy Cycle—through the diabatic heating effect of latent heat release. However, considering the importance of moisture in the dynamics of atmospheric eddy circulations (O'Gorman, 2010), it would be helpful to include it explicitly in the atmospheric energetics.

Appendix A

Lorenz Energy Cycle terms

The Lorenz Energy Cycle (LEC) terms are given as integrals over the atmosphere. Values for points below the surface, obtained when using pressure levels as a vertical coordinate, should be avoided. To do so, we use the β function proposed by Boer (1982) and defined as

$$\beta = \begin{cases} 0 & \text{if } p > p_s, \\ 1 & \text{if } p \leq p_s, \end{cases} \tag{A.1}$$

where p is pressure and p_s is surface pressure. The β function is not only a weighting factor in the final expressions, but is also used to weight each zonal and time (or ensemble) mean, as described in detail by Boer (1982). The final expressions are equivalent to those used by Boer and Lambert (2008). A list of all the symbols used in the following expressions is shown in Table A.1. The reservoirs of the LEC are given by:

$$P_m = \frac{c_p}{2} \int \gamma [\langle\beta\rangle][\langle T\rangle]''^2 \rho dV$$

$$P_e = \frac{c_p}{2} \int \gamma [\langle\beta\rangle \langle T\rangle^{*2}] \rho dV + \frac{c_p}{2} \int \gamma [\langle\beta\rangle \langle T'^2\rangle] \rho dV$$

$$K_m = \frac{1}{2} \int [\langle\beta\rangle] \left([\langle u\rangle]^2 + [\langle v\rangle]^2 \right) \rho dV$$

$$K_e = \frac{1}{2} \int \left[\langle\beta\rangle \left(\langle u\rangle^{*2} + \langle v\rangle^{*2} \right) \right] \rho dV + \frac{1}{2} \int \left[\langle\beta\rangle \left(\langle u'^2\rangle + \langle v'^2\rangle \right) \right] \rho dV,$$

where $[X]$ denotes the zonal-mean of X, $\langle X\rangle$ the ensemble (or time) mean of X, $\widetilde{X}$ the global mean over a constant pressure level, and X^*, X' and X'' are the corresponding deviations from these means. $\gamma = -(\theta/T)(R/c_p p)(\partial\widetilde{\theta}/\partial p)^{-1}$, is the inverse mean static stability. Conversion,

generation and dissipation terms are given by:

$$\begin{aligned} C(P_m, P_e) = &- c_p \int \gamma \left[\langle\beta\rangle \left(\langle v'T'\rangle + \langle v\rangle^*\langle T\rangle^*\right)\right] \frac{\partial[\langle T\rangle]}{a\partial\phi}\rho dV \\ &- c_p \int p^{-k} \left[\langle\beta\rangle \left(\langle\omega'T'\rangle + \langle\omega\rangle^*\langle T\rangle^*\right)\right] \frac{\partial\left(\gamma p^k[\langle T\rangle]''\right)}{\partial p}\rho dV \end{aligned} \tag{A.2}$$

$$C(P_e, K_e) = - \int [\langle\beta\rangle \left(\langle\omega'\alpha'\rangle + \langle\omega\rangle^*\langle\alpha\rangle^*\right)]\rho dV \tag{A.3}$$

$$\begin{aligned} C(K_e, K_m) = &\int \left[\langle\beta\rangle \left(\langle v'u'\rangle + \langle v\rangle^*\langle u\rangle^*\right)\right] \cos\phi \frac{\partial\left([\langle u\rangle]/\cos\phi\right)}{a\partial\phi}\rho dV \\ &+ \int \left[\langle\beta\rangle \left(\langle v'^2\rangle + \langle v\rangle^{*2}\right)\right] \frac{\partial[\langle v\rangle]}{a\partial\phi}\rho dV \\ &+ \int \left[\langle\beta\rangle \left(\langle\omega'u'\rangle + \langle\omega\rangle^*\langle u\rangle^*\right)\right] \frac{\partial[\langle u\rangle]}{\partial p}\rho dV \\ &+ \int \left[\langle\beta\rangle \left(\langle\omega'v'\rangle + \langle\omega\rangle^*\langle v\rangle^*\right)\right] \frac{\partial[\langle v\rangle]}{\partial p}\rho dV \\ &- \int [\langle v\rangle] \left(\left[\langle\beta\rangle \left(\langle u'^2\rangle + \langle u\rangle^{*2}\right)\right]\right) \frac{\tan\phi}{a}\rho dV \end{aligned} \tag{A.4}$$

$$C(P_m, K_m) = - \int [\langle\beta\rangle] [\langle\omega\rangle]'' [\langle\alpha\rangle]''\rho dV \tag{A.5}$$

$$G_m = \int \gamma [\langle\beta\rangle] [\langle T\rangle]'' [\langle Q\rangle]''\rho dV \tag{A.6}$$

$$G_e = \int \gamma \left[\langle\beta\rangle \left(\langle T'Q'\rangle + \langle T\rangle^*\langle Q\rangle^*\right)\right]\rho dV \tag{A.7}$$

$$D_e = \int \left[\langle\beta\rangle \left(\langle u'F'_x\rangle + \langle v'F'_y\rangle + \langle u\rangle^*\langle F_x\rangle^* + \langle v\rangle^*\langle F_y\rangle^*\right)\right]\rho dV \tag{A.8}$$

$$D_m = \int [\langle\beta\rangle] \left([\langle u\rangle][\langle F_x\rangle] + [\langle v\rangle][\langle F_y\rangle]\right)\rho dV \tag{A.9}$$

The generation and dissipation terms are not calculated directly here, but are obtained as residuals in the equilibrium runs.

When dividing the atmosphere at an isobaric surface, boundary fluxes for each reservoir must be computed, including the pressure-work terms that contribute to the kinetic energy reservoir

(last term in equations A.12 and A.13). This is consistent with our $\omega\alpha$ formulation of the P to K conversions (for details see Peixoto and Oort (1974)). These are surface integrals evaluated at the boundary (fixed pressure level):

$$B(P_m) = c_p \int \gamma \left[\langle\omega' T'\rangle + \langle\omega\rangle^* \langle T\rangle^*\right] [\langle T\rangle]'' dA/g + \frac{c_p}{2} \int \gamma [\langle\omega\rangle][\langle T\rangle]''^2 dA/g \tag{A.10}$$

$$B(P_e) = \frac{c_p}{2} \int \gamma \left[\left\langle \omega \left(T'^2 + \langle T\rangle^{*2}\right)\right\rangle\right] dA/g + c_p \int \gamma \left[\langle w' T'\rangle^* \langle T\rangle^*\right] dA/g \tag{A.11}$$

$$\begin{aligned} B(K_e) = {} & \frac{1}{2} \int \left[\left\langle \omega \left(u'^2 + v'^2 + \langle u\rangle^{*2} + \langle v\rangle^{*2}\right)\right\rangle\right] dA/g \\ & + \int \left[\langle\omega' u'\rangle^* \langle u\rangle^* + \langle\omega' v'\rangle^* \langle v\rangle^*\right] dA/g + \int g \left[\langle\omega' z'\rangle + \langle\omega\rangle^* \langle z\rangle^*\right] dA/g \end{aligned} \tag{A.12}$$

$$\begin{aligned} B(K_m) = {} & \frac{1}{2} \int [\langle\omega\rangle] \left([\langle u\rangle]^2 + [\langle v\rangle]^2\right) dA/g + \int \left[\left\langle \omega' u' \right\rangle + \langle\omega\rangle^* \langle u\rangle^*\right] [\langle u\rangle] dA/g \\ & + \int \left[\left\langle \omega' v' \right\rangle + \langle\omega\rangle^* \langle v\rangle^*\right] [\langle v\rangle] dA/g + \int g [\langle\omega\rangle][\langle z\rangle]'' dA/g \end{aligned} \tag{A.13}$$

Table A.1: List of symbols.

Symbol	Description
a	Earth's average radius
c_p	specific heat at constant pressure
dA	surface element
dV	volume element
g	acceleration due to gravity
k	R/c_p
p	pressure
p_s	surface pressure
t	time
u	zonal wind component
v	meridional wind component
$B(X)$	boundary flux of X
$C(X, Y)$	conversion rate from X to Y
$D(Y)$	dissipation rate of Y
F_x, F_y	frictional force in x and y
K_e	eddy kinetic energy
K_m	zonal mean kinetic energy
P_e	eddy available potential energy
P_m	zonal mean available potential energy
Q	diabatic heating rate
R	gas constant for dry air
T	temperature
α	specific volume
β	equals 0 for underground points, 1 otherwise
γ	stability factor, $\gamma = -(\theta/T)(R/c_p p)(\partial\widetilde{\theta}/\partial p)^{-1}$
λ	longitude
ϕ	latitude
ρ	density
θ	potential temperature
ω	vertical velocity

Appendix B

Transient and stationary eddy decomposition

Following the same notation and symbols as in the previous Appendix (see Table A.1), we present here the expressions for the additional terms that appear when decomposing the eddy reservoirs into stationary and transient eddy components.

The new reservoirs are obtained by separating the two contributions for P_e and for K_e in expression A.2:

$$P_{se} = \frac{c_p}{2} \int \gamma[\langle\beta\rangle\langle T\rangle^{*2}]\rho dV$$

$$P_{te} = \frac{c_p}{2} \int \gamma[\langle\beta\rangle\langle T'^2\rangle]\rho dV$$

$$K_{se} = \frac{1}{2} \int \left[\langle\beta\rangle \left(\langle u\rangle^{*2} + \langle v\rangle^{*2}\right)\right]\rho dV$$

$$K_{te} = \frac{1}{2} \int \left[\langle\beta\rangle \left\langle u'^2\right\rangle + \left\langle v'^2\right\rangle)\right]\rho dV.$$

The reservoirs P_m and K_m, as well as the conversion term between them, remain unchanged:

$$P_m = \frac{c_p}{2} \int \gamma[\langle\beta\rangle][\langle T\rangle]''^2\rho dV$$

$$K_m = \frac{1}{2} \int [\langle\beta\rangle] \left([\langle u\rangle]^2 + [\langle v\rangle]^2\right)\rho dV$$

$$C(P_m, K_m) = -\int [\langle\beta\rangle] [\langle\omega\rangle]'' [\langle\alpha\rangle]''\rho dV.$$

The expressions for the conversion terms $C(P_m, P_e)$, $C(P_e, K_e)$ and $C(K_e, K_m)$ (A.2 through

A.4) can be separated in order to obtain the contributions corresponding to stationary and transient eddies:

$$C(P_m, P_{se}) = -c_p \int \gamma \left[\langle\beta\rangle\langle v\rangle^*\langle T\rangle^*\right] \frac{\partial[\langle T\rangle]}{a\partial\phi}\rho dV - c_p \int p^{-k} \left[\langle\beta\rangle\langle\omega\rangle^*\langle T\rangle^*\right] \frac{\partial\left(\gamma p^k[\langle T\rangle]''\right)}{\partial p}\rho dV \tag{B.1}$$

$$C(P_m, P_{te}) = -c_p \int \gamma \left[\langle\beta\rangle\langle v'T'\rangle\right] \frac{\partial[\langle T\rangle]}{a\partial\phi}\rho dV - c_p \int p^{-k} \left[\langle\beta\rangle\langle\omega'T'\rangle\right] \frac{\partial\left(\gamma p^k[\langle T\rangle]''\right)}{\partial p}\rho dV \tag{B.2}$$

$$C(P_{se}, K_{se}) = -\int \left[\langle\beta\rangle\langle\omega\rangle^*\langle\alpha\rangle^*\right]\rho dV \tag{B.3}$$

$$C(P_{te}, K_{te}) = -\int \left[\langle\beta\rangle\langle\omega'\alpha'\rangle\right]\rho dV \tag{B.4}$$

$$C(K_{se}, K_m) = \int \left[\langle\beta\rangle\langle v\rangle^*\langle u\rangle^*\right]\cos\phi \frac{\partial\left([\langle u\rangle]/\cos\phi\right)}{a\partial\phi}\rho dV + \int \left[\langle\beta\rangle\langle v\rangle^{*2}\right] \frac{\partial[\langle v\rangle]}{a\partial\phi}\rho dV + \int \left[\langle\beta\rangle\langle w\rangle^*\langle u\rangle^*\right] \frac{\partial[\langle u\rangle]}{\partial p}\rho dV + \int \left[\langle\beta\rangle\langle w\rangle^*\langle v\rangle^*\right] \frac{\partial[\langle v\rangle]}{\partial p}\rho dV - \int \left[\langle v\rangle\right]\left(\left[\langle\beta\rangle\langle u\rangle^{*2}\right]\right) \frac{\tan\phi}{a}\rho dV \tag{B.5}$$

$$C(K_{te}, K_m) = \int \left[\langle\beta\rangle\langle v'u'\rangle\right]\cos\phi \frac{\partial\left([\langle u\rangle]/\cos\phi\right)}{a\partial\phi}\rho dV + \int \left[\langle\beta\rangle\langle v'^2\rangle\right] \frac{\partial[\langle v\rangle]}{a\partial\phi}\rho dV + \int \left[\langle\beta\rangle\langle w'u'\rangle\right] \frac{\partial[\langle u\rangle]}{\partial p}\rho dV + \int \left[\langle\beta\rangle\langle w'v'\rangle\right] \frac{\partial[\langle v\rangle]}{\partial p}\rho dV - \int \left[\langle v\rangle\right]\left(\left[\langle\beta\rangle\langle u'^2\rangle\right]\right) \frac{\tan\phi}{a}\rho dV. \tag{B.6}$$

Additionally, we must consider additional conversion terms that appear due to the separation

of the eddy reservoirs. These are $C(P_{te}, P_{se})$ and $C(K_{se}, K_{te})$:

$$C(P_{te}, P_{se}) = -c_p \int \gamma \left[\langle\beta\rangle \langle T'v' \rangle^* \frac{\partial \langle T \rangle^*}{a \partial \phi} \right] \rho dV - c_p \int p^{-k} \left[\langle\beta\rangle \langle T'\omega' \rangle^* \frac{\gamma p^k \langle T \rangle^*}{p} \right] \rho dV \tag{B.7}$$

$$C(K_{se}, K_{te}) = \int \frac{\tan\phi}{a} \left[\langle\beta\rangle \left(\langle u'^2 \rangle \langle v \rangle^* - \langle v'u' \rangle \langle u \rangle^* \right) \right] \rho dV \tag{B.8}$$

$$- \frac{1}{a} \int \left[\langle\beta\rangle \left(\langle u'v' \rangle \frac{\langle u \rangle^*}{\partial \phi} + \langle v'^2 \rangle \frac{\langle v \rangle^*}{\partial \phi} \right) \right] \rho dV \tag{B.9}$$

$$- \int \left[\langle\beta\rangle \left(\langle u'\omega' \rangle \frac{\langle u \rangle^*}{\partial p} + \langle v'\omega' \rangle \frac{\langle v \rangle^*}{\partial p} \right) \right] \rho dV \tag{B.10}$$

The generation and dissipation rates for the zonal-mean components remain unchanged,

$$G_m = \int \gamma \left[\langle\beta\rangle \right] \left[\langle T \rangle \right]'' \left[\langle Q \rangle \right]'' \rho dV \tag{B.11}$$

$$D_m = \int \left[\langle\beta\rangle \right] \left([\langle u \rangle][\langle F_x \rangle] + [\langle v \rangle][\langle F_y \rangle] \right) \rho dV, \tag{B.12}$$

while the generation and dissipation rates for the eddy components must be separated,

$$G_{se} = \int \gamma \left[\langle\beta\rangle \langle T \rangle^* \langle Q \rangle^* \right] \rho dV \tag{B.13}$$

$$G_{te} = \int \gamma \left[\langle\beta\rangle \langle T'Q' \rangle \right] \rho dV \tag{B.14}$$

$$D_{se} = \int \left[\langle\beta\rangle \left(\langle u \rangle^* \langle F_x \rangle^* + \langle v \rangle^* \langle F_y \rangle^* \right) \right] \rho dV \tag{B.15}$$

$$D_{te} = \int \left[\langle\beta\rangle \left(\langle u'F'_x \rangle + \langle v'F'_y \rangle \right) \right] \rho dV. \tag{B.16}$$

As previously mentioned, we do not compute the generation and dissipation terms explicitely. Instead, we estimate them as residuals in the equilibrium runs. However, we present these expressions here for completeness.

When splitting the atmosphere at an isobaric level, we must compute the boundary fluxes of the stationary and transient eddy reservoirs separately. For consistency with our $\omega\alpha$ formulation (see Appendix A), the pressure-work terms contribute to the kinetic energy fluxes (last

terms in B.19 and B.20). The corresponding expressions are:

$$B(P_{se}) = \frac{c_p}{2} \int \gamma \left[\left\langle \omega \langle T \rangle^{*2} \right\rangle\right] dA/g + c_p \int \gamma \left[\langle w'T' \rangle^* \langle T \rangle^*\right] dA/g \tag{B.17}$$

$$B(P_{te}) = \frac{c_p}{2} \int \gamma \left[\left\langle \omega T'^2 \right\rangle\right] dA/g \tag{B.18}$$

$$\begin{aligned} B(K_{se}) = \frac{1}{2} \int \left[\left\langle \omega \left(\langle u \rangle^{*2} + \langle v \rangle^{*2} \right) \right\rangle\right] dA/g \\ + \int \left[\langle \omega' u' \rangle^* \langle u \rangle^* + \langle \omega' v' \rangle^* \langle v \rangle^*\right] dA/g + \int g \left[\langle \omega \rangle^* \langle z \rangle^*\right] dA/g \end{aligned} \tag{B.19}$$

$$B(K_{te}) = \frac{1}{2} \int \left[\left\langle \omega \left(u'^2 + v'^2 \right) \right\rangle\right] dA/g + \int g \left[\left\langle \omega' z' \right\rangle\right] dA/g \tag{B.20}$$

Appendix C

Equilibrium conditions in the T63L31 2xCO_2 run

For further reference about the model version and technical aspects of the integrations, please refer to Roeckner et al. (2006) and to Roeckner (2004). Analysis of integrations carried out with the same model version have been done, for example, by Jungclaus et al. (2006) and by Meehl et al. (2007). However, we consider important to show here some aspects about the equilibrium conditions in the 2xCO_2 run, given that it has been integrated for only 150 years with constant 2xCO_2 concentrations. We know that the deep ocean is not yet fully equilibriated, but the remaining trends in the atmosphere may or may not be important.

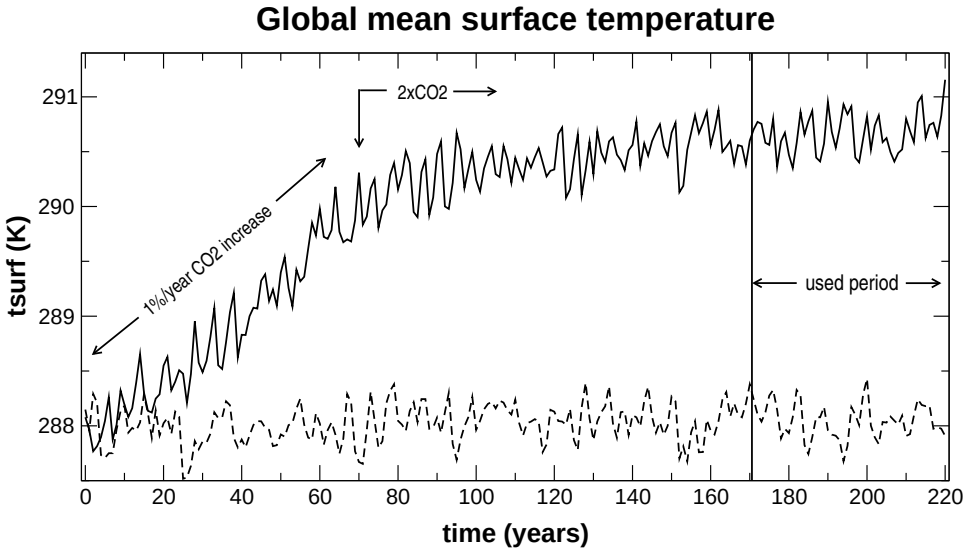

Figure C.1: Annual timeseries of global mean surface temperature of the complete 1%/year CO_2 increase to 2xCO_2 run (solid line) and of the 1xCO_2 pre-industrial control run (dashed line). We use the last 50 years of these integrations (years 2030-2080).

Figures C.1 and C.2 show the annual timeseries of global mean surface temperature and global mean temperature at 250 hPa of the 1xCO_2 and 2xCO_2 integrations. We have plotted not only the 50 year period we use here, but also the previous period which shows the complete

evolution towards the 2xCO$_2$ concentration. Visual inspection of these plots suggests that although there is a slight positive trend in both surface temperature and temperature at 250 hPa in the last 50 years of the 2xCO$_2$ run, it is very small compared to the overal warming. The warming is almost completely achieved during the first part of the integration where CO$_2$ concentrations were increased by 1%/year.

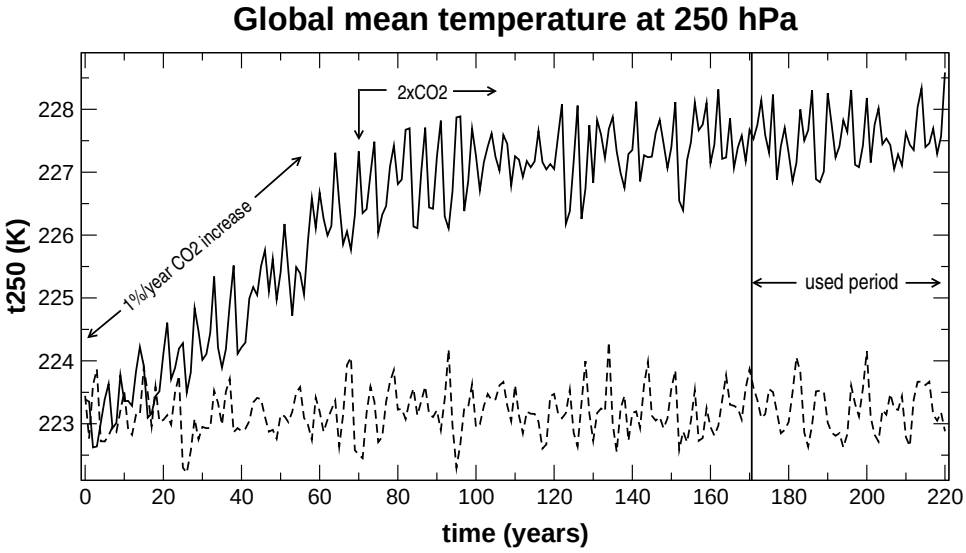

Figure C.2: Annual timeseries of global mean temperature at 250 hPa of the complete 1%/year CO$_2$ increase to 2xCO$_2$ run (solid line) and of the 1xCO$_2$ pre-industrial control run (dashed line). We use the last 50 years of these integrations (years 2030-2080).

Linear regresion of the last 50 years of the timeseries of the 2xCO$_2$ global mean surface temperature reveals a trend of 0.0028 K/year. This trend would produce 0.14 K warming in 50 years, while the total warming compared to the 1xCO$_2$ run is of 2.6 K. In other words, the *transient* component of the warming during these 50 years is about 5% of the total warming. In the case of mean temperature at 250 hPa, the trend of the last 50 years of the 2xCO$_2$ run is slightly weaker: 0.0024 K/year. This means a warming of 0.12 K in 50 years, compared to a total warming of about 4.3 K relative to the 1xCO$_2$ pre-industrial run. In this case, the *t*ransient warming is less than 3% of the total warming. Having achieved at least 95% of the warming in about 170 years, we do not expect the main energetics response to be affected by the additional 5% warming during 50 years. It is a very slow and small warming, that clearly has no strong transient component in the atmosphere. If we would be interested in analyzing an equilibrium condition in the deep ocean, this run would not be long enough. But the remaining trends in the atmosphere are certainly small enough so that very little change is seen during the 50 years we use, compared to the overal change relative to the 1xCO$_2$ conditions. On the other hand, this type of run is a standard setup used for the IPCC-AR4, so that an energetics analysis of these integrations could be of special interest in terms of model intercomparison.

Appendix D

Supplementary material for Section 3.3

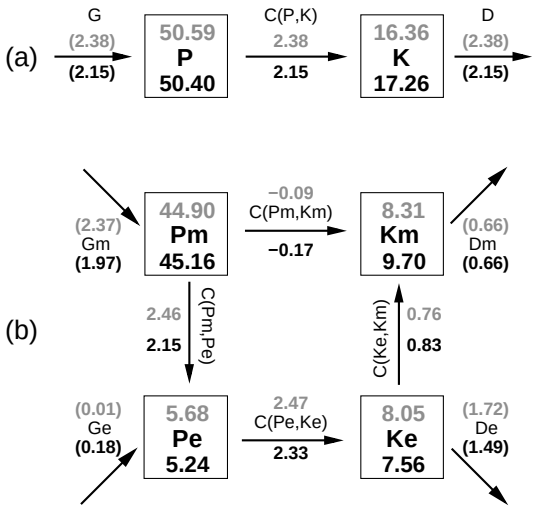

Figure D.1: (a) 2-box and (b) 4-box diagram of the LEC-terms for CTRL (above, gray) and UP (below, black). Generation and dissipation terms (in parenthesis) are obtained as residuals. Units are 10^5 J m^{-2} for reservoirs and W m^{-2} for conversion, generation and dissipation terms. Arrows indicate the direction corresponding to positive values; negative values imply opposite direction.

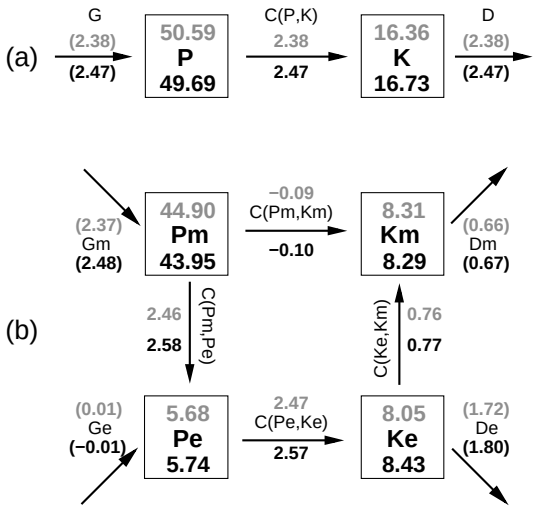

Figure D.2: (a) 2-box and (b) 4-box diagram of the LEC-terms for CTRL (above, gray) and SFC (below, black). Generation and dissipation terms (in parenthesis) are obtained as residuals. Units are 10^5 J m^{-2} for reservoirs and W m^{-2} for conversion, generation and dissipation terms. Arrows indicate the direction corresponding to positive values; negative values imply opposite direction.

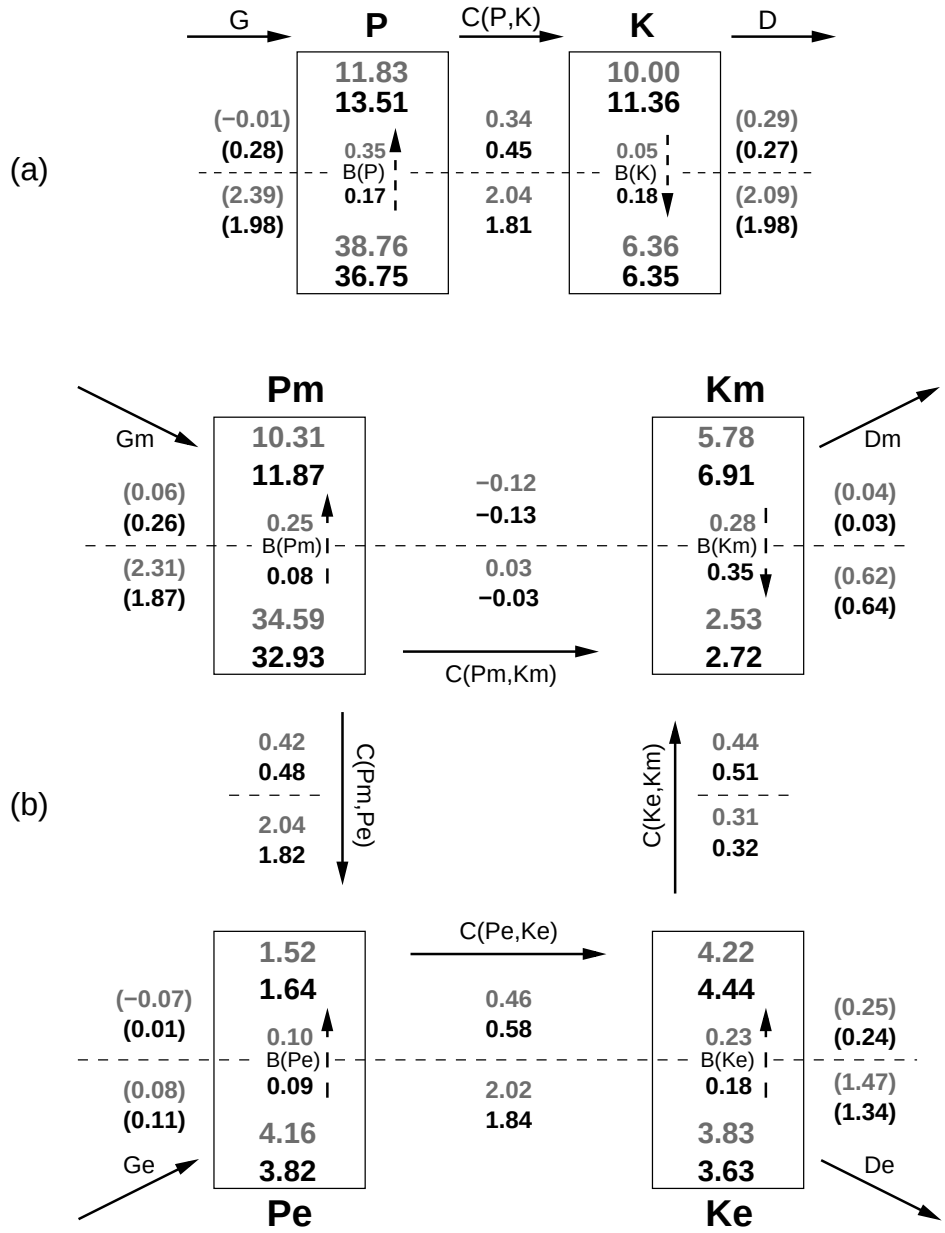

Figure D.3: (a) 2-box and (b) 4-box diagram of the LEC-terms for the CTRL integration (above, gray) and for FULL (below, black), split at 340 hPa (dotted line). Generation and dissipation terms (in parenthesis) are obtained as residuals. Units are 10^5 J m^{-2} for reservoirs and W m^{-2} for conversion, generation and dissipation terms. Arrows indicate the direction corresponding to positive values; negative values imply opposite direction.

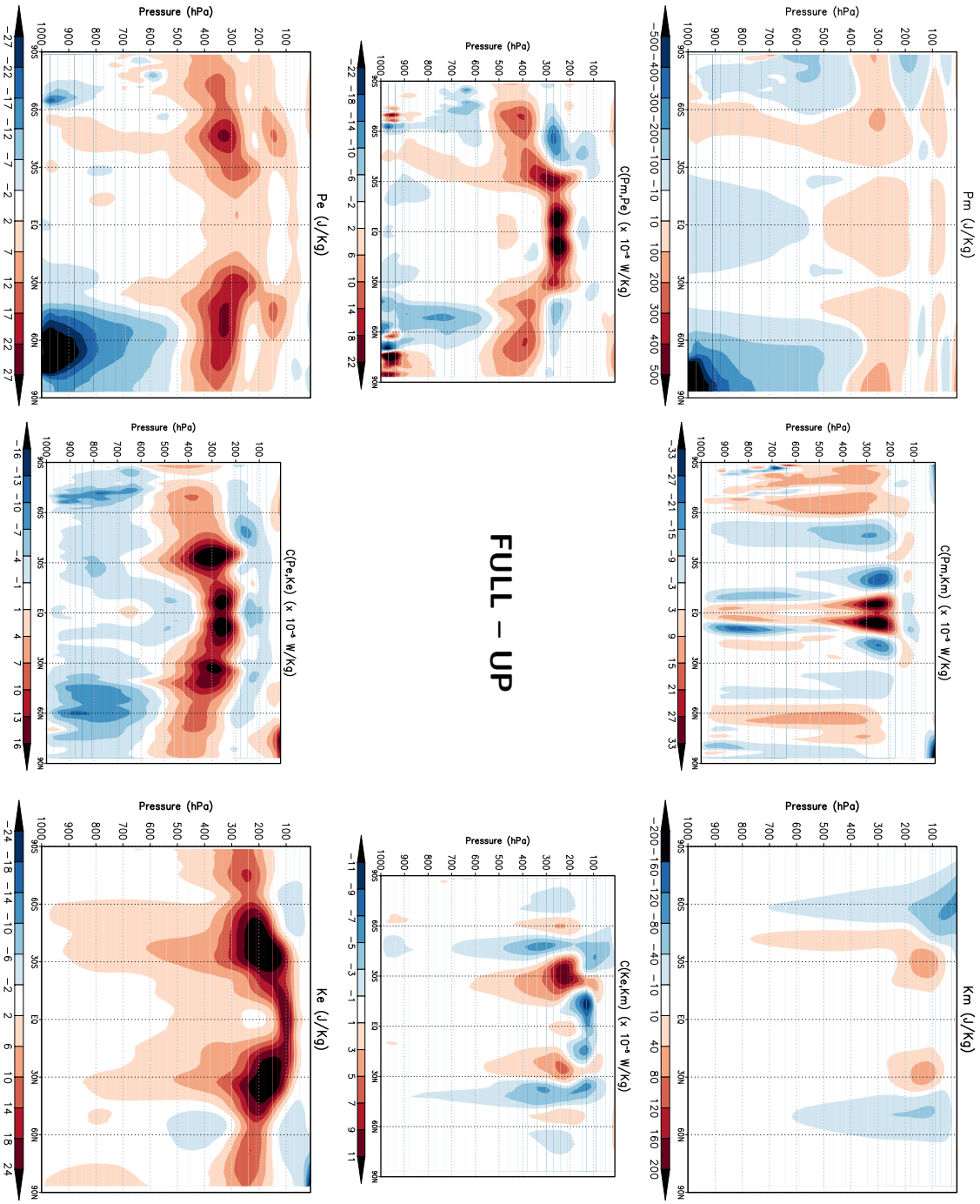

Figure D.4: Difference in the changes in the vertical cross sections of the 4-box LEC terms for the FULL integration and the UP integration (i.e., Figure 3.6 minus Figure 3.11). Counterclockwise, starting from the upper left: P_m, $C(P_m, P_e)$, P_e, $C(P_e, K_e)$, K_e, $C(K_e, K_m)$, K_m, and $C(P_m, K_m)$. Units are J Kg^{-1} for reservoirs, and $\times 10^{-5}$ W m^{-2} for conversion terms.

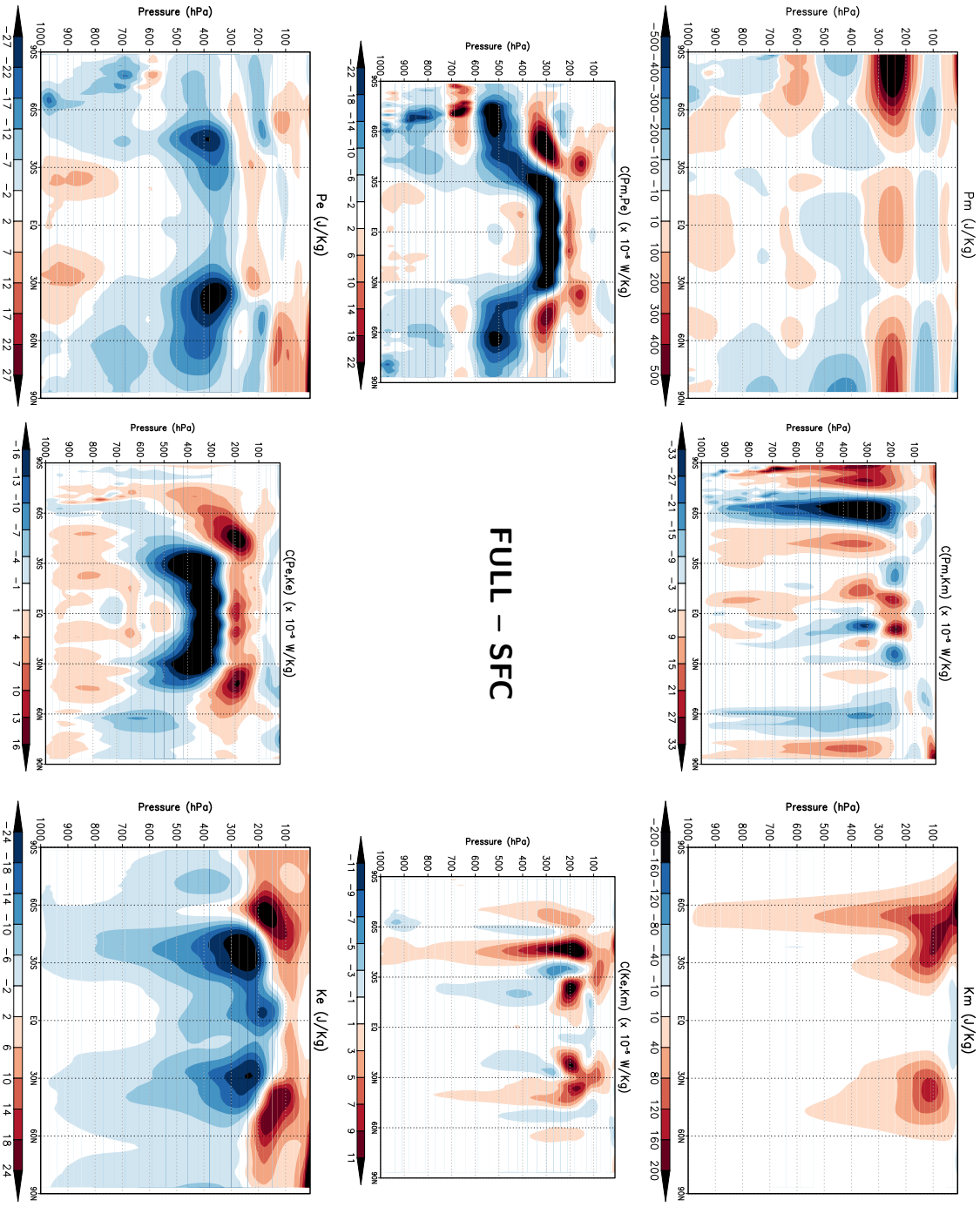

Figure D.5: Difference in the changes in the vertical cross sections of the 4-box LEC terms for the FULL integration and the SFC integration (i.e. Figure 3.6 minus Figure 3.12). Counterclockwise, starting from the upper left: P_m, $C(P_m, P_e)$, P_e, $C(P_e, K_e)$, K_e, $C(K_e, K_m)$, K_m, and $C(P_m, K_m)$. Units are J Kg^{-1} for reservoirs, and $\times 10^{-5}$ W m^{-2} for conversion terms.

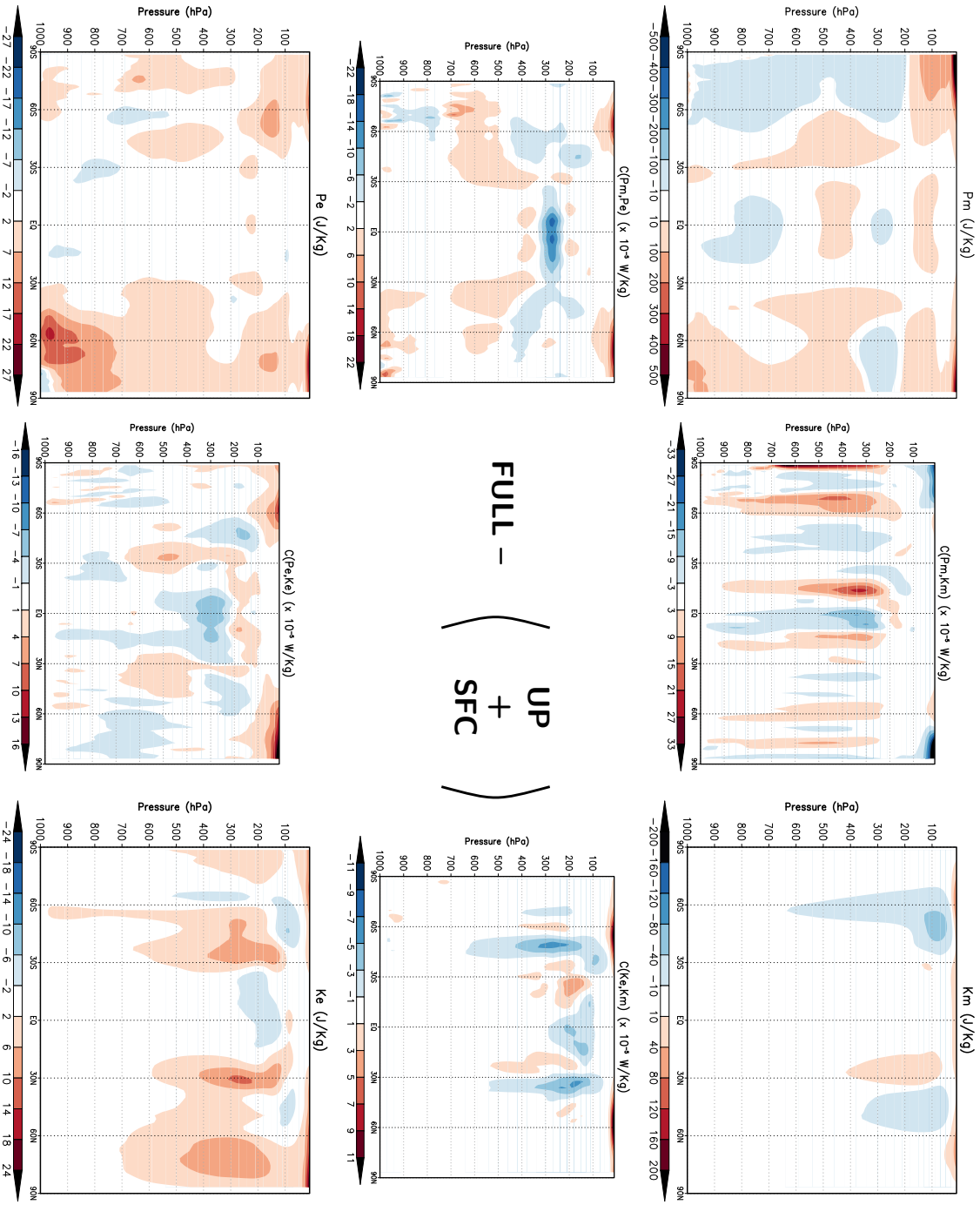

Figure D.6: Difference in the changes in the vertical cross sections of the 4-box LEC terms for the FULL integration and the sum of the UP and SFC integrations. Counterclockwise, starting from the upper left: P_m, $C(P_m, P_e)$, P_e, $C(P_e, K_e)$, K_e, $C(K_e, K_m)$, K_m, and $C(P_m, K_m)$. Units are J Kg^{-1} for reservoirs, and $\times 10^{-5}$ W m^{-2} for conversion terms.

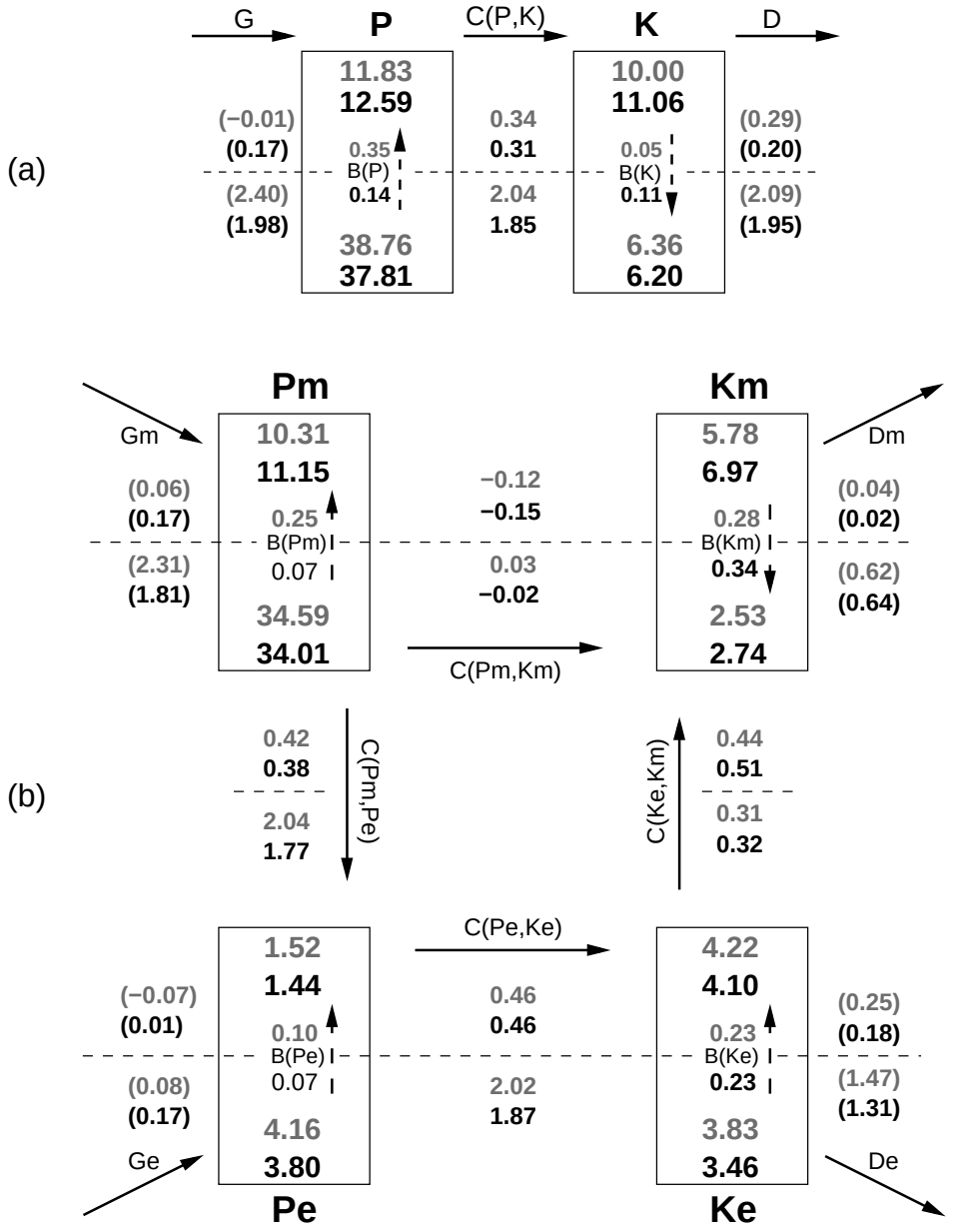

Figure D.7: (a) 2-box and (b) 4-box diagram of the LEC-terms for the CTRL integration (above, gray) and for UP (below, black), split at 340 hPa (dotted line). Generation and dissipation terms (in parenthesis) are obtained as residuals. Units are 10^5 J m^{-2} for reservoirs and W m^{-2} for conversion, generation and dissipation terms. Arrows indicate the direction corresponding to positive values; negative values imply opposite direction.

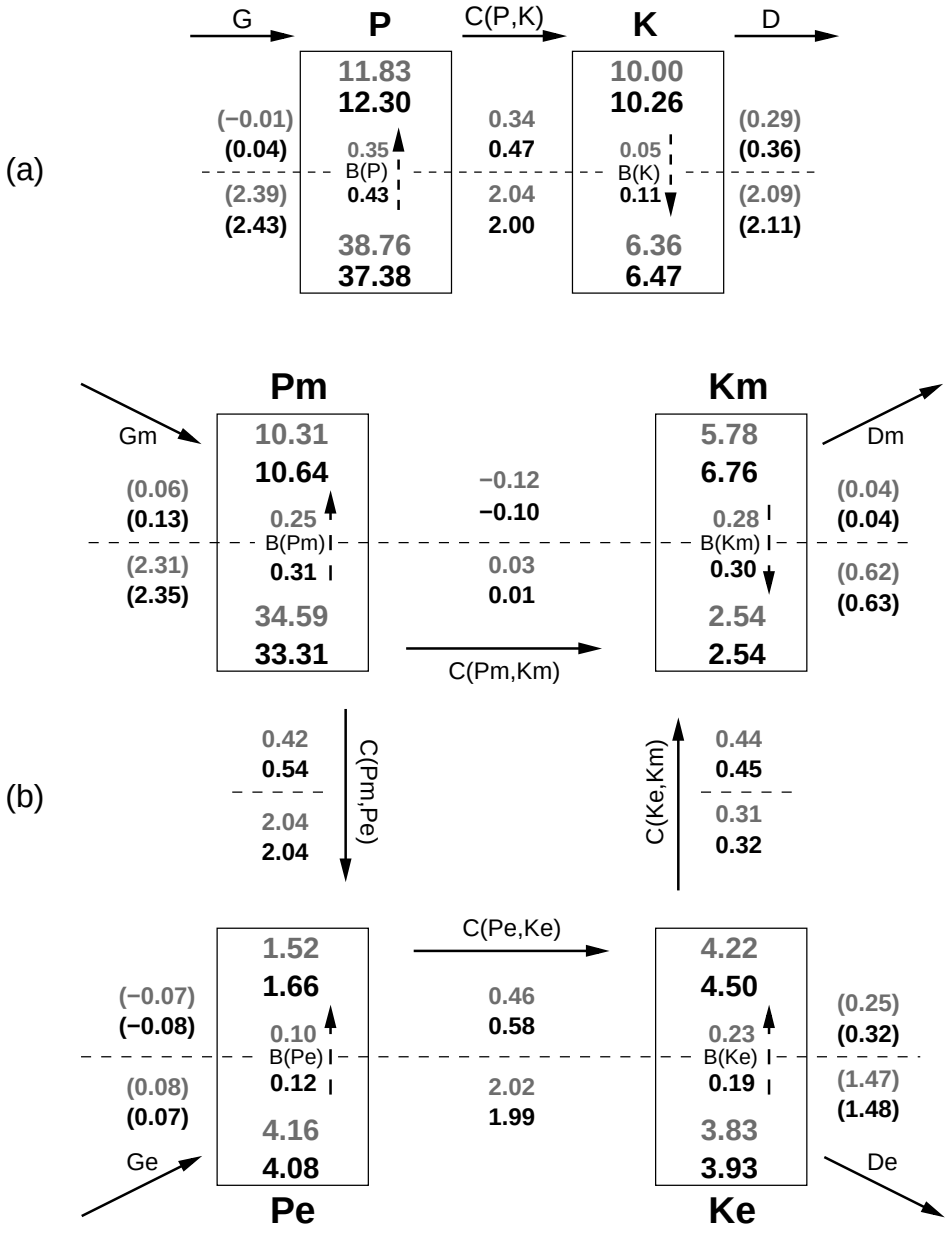

Figure D.8: (a) 2-box and (b) 4-box diagram of the LEC-terms for the CTRL integration (above, gray) and for SFC (below, black), split at 340 hPa (dotted line). Generation and dissipation terms (in parenthesis) are obtained as residuals. Units are 10^5 J m^{-2} for reservoirs and W m^{-2} for conversion, generation and dissipation terms. Arrows indicate the direction corresponding to positive values; negative values imply opposite direction.

Bibliography

Bengtsson, L. and K. I. Hodges, 2009: On the evaluation of temperature trends in the tropical troposphere. *Clim. Dynam.*, 1–12, doi:10.1007/s00382-009-0680-y.

Bengtsson, L., K. I. Hodges, and N. Keenlyside, 2009: Will Extratropical Storms Intensify in a Warmer Climate? *J. Climate*, **22**, 2276–2301, doi:10.1175/2008JCLI2678.1.

Boer, G. J., 1982: Diagnostic Equations in Isobaric Coordinates. *Mon. Wea. Rev.*, **110**, 1801–1820.

Boer, G. J., 1995: Some Dynamical Consequences of Greenhouse Gas Warming. *Atmos.-Ocean*, **33 (4)**, 731–751.

Boer, G. J. and S. Lambert, 2008: The energy cycle in atmospheric models. *Clim. Dynam.*, **30**, 371–390.

Charney, J. G., 1947: The dynamics of long waves in a baroclinic westerly current. *J. Meteor.*, **4**, 135–162.

Eady, E. T., 1949: Long Waves and Cyclone Waves. *Tellus*, **1**, 33–52.

Fyfe, J. C. and O. A. Saenko, 2006: Simulated changes in the extratropical Southern Hemisphere winds and currents. *Geophys. Res. Lett.*, **33**, L06701, doi:10.1029/2005GL025332.

Geng, Q. and M. Sugi, 2003: Possible Change of Extratropical Cyclone Activity due to Enhanced Greenhouse Gases and Sulfate Aerosols—Study with a High-Resolution AGCM. *J. Climate*, **16**, 2262–2274.

Green, J. S. A., 1960: A problem in baroclinic stability. *Quart. J. Roy. Meteor. Soc.*, **86**, 237–251.

Held, I. M., 1978: The vertical scale of an unstable baroclinic wave and its importance for eddy heat flux parameterizations. *J. Atmos. Sci.*, **35**, 572–576.

Held, I. M., 1993: Large-Scale Dynamics and Global Warming. *Bull. Amer. Meteor. Soc.*, **74 (2)**, 228–240.

Held, I. M. and B. J. Soden, 2000: Water vapor feedback and global warming. *Annual Review of Energy and the Environment*, **25 (1)**, 441–475, doi:10.1146/annurev.energy.25.1.441.

Hernández-Deckers, D. and J.-S. von Storch, 2010: Energetics Responses to Increases in Greenhouse Gas Concentration. *J. Climate*, **23 (14)**, 3874–3887, doi: 10.1175/2010JCLI3176.1.

Holton, J. R., 2004: *An Introduction to Dynamical Meteorology*. Elsevier Inc., 535 pp.

Jungclaus, J., et al., 2006: Ocean Circulation and Tropical Variability in the Coupled Model ECHAM5/MPI-OM. *J. Climate*, **19**, 3952–3972.

Krishnamurti, T., J. Xue, H. Bedi, K. Ingles, and D. Oosterhof, 1991: Physical initialization for numerical weather prediction over the tropics. *Tellus*, **43AB**, 53–81.

Li, L., A. P. Ingersoll, X. Jiang, D. Feldman, and Y. L. Yung, 2007: Lorenz energy cycle of the global atmosphere based on reanalysis datasets. *Geophys. Res. Lett.*, **34**, L16813, doi: 10.1029/2007GL029985.

Lim, E.-P. and I. Simmonds, 2007: Southern Hemisphere Winter Extratropical Cyclone Characteristics and Vertical Organization Observed with the ERA-40 Data in 1979-2001. *J. Climate*, **20**, 2675–2690, doi:10.1175/JCLI4135.1.

Lim, E.-P. and I. Simmonds, 2009: Effect of tropospheric temperature change on the zonal mean circulation and SH winter extratropical cyclones. *Clim. Dynam.*, **33**, 19–32, doi: 10.1007/s00382-008-0444-0.

Lindzen, R. S. and B. Farrell, 1980: A Simple Approximate Result for the Maximum Growth Rate of Baroclinic Instabilities. *J. Atmos. Sci.*, **37**, 1648–1654.

Lorenz, D. J. and E. T. DeWeaver, 2007: Tropopause height and zonal wind response to global warming in the IPCC scenario integrations. *J. Geophys. Res.*, **112**, D10119, doi: 10.1029/2006JD008087.

Lorenz, E. N., 1955: Available potential Energy and the Maintenance of the General Circulation. *Tellus*, **7 (2)**, 157–167.

Lorenz, E. N., 1967: *The nature and theory of the general circulation of the atmosphere*. World Meteorological Organization, 161 pp.

Lu, J., G. A. Vecchi, and T. Reichler, 2007: Expansion of the Hadley cell under global warming. *Geophys. Res. Lett.*, **34**, L06805, doi:10.1029/2006GL028443.

Lucarini, V., 2009: Thermodynamic efficiency and entropy production in the climate system. *Phys. Rev. E*, **80 (2)**, 021 118, doi:10.1103/PhysRevE.80.021118.

Marquet, P., 1991: On the concept of exergy and available enthalpy: Application to atmospheric energetics. *Quart. J. Roy. Meteor. Soc.*, **117**, 449–475.

Marquet, P., 2005: Analyse des impacts d'un 2xCO2 sur l'energétique de l'atmosphère (Analysis of the 2xCO2 impacts on the atmospheric energetics). Workshop on Atmospheric Modelling, Toulouse (personal communication).

Marquet, P., 2006: Diagnostic of change in energetics for a 2xCO2. E.G.U., Vienna (personal communication).

Marsland, S., H. Haak, J. Jungclaus, M. Latif, and F. Roske, 2003: The Max-Planck-Institute global ocean/sea ice model with orthogonal curvilinear coordinates. *Ocean Modelling*, **5 (2)**, 91–127.

Meehl, G., et al., 2007: Global Climate Projections. *Climate Change 2007: The Physical Science Basis. Contribution of Working Group I to the Fourth Assesment Report of the Intergovernmental Panel on Climate Change*, S. Solomon, D. Qin, M. Manning, Z. Chen, M. Marquis, K. Averyt, M. Tignor, and H. Miller, Eds., Cambridge University Press, Cambridge, United Kingdom and New York, NY, USA, 747–845.

O'Gorman, P. A., 2010: The effective static stability experienced by eddies in a moist atmosphere. *J. Atmos. Sci.*, (in press), doi:10.1175/2010JAS3537.1.

O'Gorman, P. A. and T. Schneider, 2008: Energy of Midlatitude Transient Eddies in Idealized Simulations of Changed Climates. *J. Climate*, **21**, 5797–5806, doi: 10.1175/2008JCLI2099.1.

Oort, A. H. and J. P. Peixoto, 1974: The Annual Cycle of the Energetics of the Atmosphere on a Planetary Scale. *J. Geophys. Res.*, **79 (18)**, 2705–2719.

Pedlosky, J., 1987: *Geophysical fluid dynamics*. Springer-Verlag, 710 pp.

Peixoto, J. P. and A. H. Oort, 1974: The Annual Distribution of Atmospheric Energy on a Planetary Scale. *J. Geophys. Res.*, **79 (15)**, 2149–2159.

Peixoto, J. P. and A. H. Oort, 1992: *Physics of Climate*. American Institute of Physics, 520 pp.

Plumb, R. A., 1983: A New Look at the Energy Cycle. *J. Atmos. Sci.*, **40**, 1669–1688.

Roeckner, E., 2004: IPCC-AR4 MPI-ECHAM5_T63L31 MPI-OM_GR1.5L40 1%/year CO2 increase experiment to doubling run no.1: atmosphere 6 HOUR values MPImet/MaD Germany. World Data Center for Climate. CERA-DB "EH5-T63L31_OM_1CO2_1_6H", http://cera-www.dkrz.de/WDCC/ui/Compact.jsp?acronym=EH5-T63L31_OM_1CO2_1_6H.

Roeckner, E., M. Lautenschlager, and M. Esch, 2006: IPCC-AR4 MPI-ECHAM5_T63L31 MPI-OM_GR1.5L40 PIcntrl (pre-industrial control experiment): atmosphere 6 HOUR values MPImet/MaD Germany. World Data Center for Climate, doi:10.1594/WDCC/EH5-T63L31_OM-GR1.5L40_CTL_6H.

Roeckner, E., et al., 2003: The atmospheric general circulation model ECHAM5, Part I: Model description. Tech. Rep. 349, Max-Planck-Institute for Meteorology, 127 pp.

Romanski, J., 2009: Investigating the Role of Individual Diabatic Heating Components in Global Atmospheric Circulation and Climate Sensitivity: An Energetics Approach. Ph.D. thesis, Columbia University, (personal communication).

Schneider, T., P. A. O'Gorman, and X. Levine, 2010: Water vapor and the dynamics of climate changes. *Rev. Geophys.*, **48**, RG3001, doi:10.1029/2009RG000302.

Seiffert, R. and J.-S. von Storch, 2008: Impact of atmospheric small-scale fluctuations on climate sensitivity. *Geophys. Res. Lett.*, **35**, L10704, doi:10.1029/2008GL033483.

Sherwood, S. C., R. Roca, T. M. Weckwerth, and N. G. Andronova, 2010: Tropospheric water vapor, convection and climate. *Rev. Geophys.*, **48**, RG2001, doi:10.1029/2009RG000301.

Sienz, F., A. Schneidereit, R. Blender, and K. Fraedrich, 2010: Extreme value statistics for North Atlantic cyclones. *Tellus*, **A**, doi:10.1111/j.1600-0870.2010.00449.x.

Valcke, S., A. Caubel, R. Vogelsang, and D. Declat, 2004: OASIS3 User Guide (prism_2-4). Tech. rep., PRISM Report Series, No. 2, 5th Ed. URL `http://www.prism.enes.org/Publications/Reports/all_editions/index.php#report02`.

Vecchi, G. A. and B. J. Soden, 2007: Global Warming and the Weakening of the Tropical Circulation. *J. Climate*, **20**, 4316–4340.

von Storch, H. and F. W. Zwiers, 1999: *Statistical Analysis in Climate Research*. Cambridge University Press, 484 pp.

von Storch, J.-S., 2008: Towards climate prediction: Interannual potential predictability due to an increase in CO2 concentration as diagnosed from an ensemble of AO-GCM integrations. *J. Climate*, **21 (18)**, 4607–4628.

Williams, G. P., 2006: Equatorial Superrotation and Barotropic Instability: Static Stability Variants. *J. Atmos. Sci.*, **63**, 1548–1557.

Wu, Y., M. Ting, R. Seager, H.-P. Huang, and M. A. Cane, 2010: Changes in storm tracks and energy transports in a warmer climate simulated by the GFDL CM2.1 model. *Clim. Dynam.*, 1–20, doi:10.1007/s00382-010-0776-4.

Yin, J. H., 2005: A consistent poleward shift of the storm tracks in simulations of 21st century climate. *Geophys. Res. Lett.*, **32**, L18701, doi:10.1029/2005GL023684.

Acknowledgement

This thesis would not have been possible without the helpful advise and support provided by Jin-Song von Storch, my principal advisor. Thanks for your patience and unconditional help. Special thanks also to Jochem Marotzke, who chaired my Advisory Panel and read this thesis as the first referee. I also wish to thank Axel Kleidon, the third member of my Advisory Panel, for his support.

I received very useful comments from Zoltan Szuts, Aiko Voigt and Nils Fischer, who kindly proofread parts of this thesis. Thanks to them, the final text has been enriched and certainly made more comprehensible.

The temperature-nudged experiments were possible thanks to a lot of help from Sebastian Rast concerning ECHAM's nudging module. On the other hand, running the coupled model was much easier with Helmuth Haak's help. Finally, the Climate Data Operators (CDO) did a great deal of the computations for me. Thanks to Uwe Schulzweida for the CDO-support. Special thanks to Dirk Notz for his help with the presentation of my defense. I also thank CIS for the technical support, as well as the ZMAW library and the administrative staff for their kind support.

I am very grateful to the members of the Ocean Department of the Max Planck Institute for Meteorology, from whom I have learned much at the group meetings, even though my research was focused on the atmosphere. Special thanks to my officemate, María Paz. I really enjoyed sharing the office with you, and I even learned something about EB1 and EBH! And of course, many others also made life nicer at the institute. Among them are Aiko, Malte, Rita, Zoli, Werner, Fanny, Rosi, Steffen, Nils, Mario, Max, Jaison, Davide, Florian, Peter, Chao, Laura, Ronny, Iris, Alberto, Claas, Eleftheria, Oliver, Julia, Freja, Alfredo, Daniela, Francesca, Marco, and probably others whom I forget now.

Thanks to Verónica for being always with me, and to my family, both in Colombia and Belgium, for their support in everything I've done and their openheartedness.

Furthermore, the support of the International Max Planck Research School on Earth System Modelling (IMPRS-ESM), and in particular of Antje and Conni, made my work and life much easier during my PhD studies.

Die gesamten Veröffentlichungen in der Publikationsreihe des MPI-M
„Berichte zur Erdsystemforschung“,
„Reports on Earth System Science“,
ISSN 1614-1199

sind über die Internetseiten des Max-Planck-Instituts für Meteorologie erhältlich:

http://www.mpimet.mpg.de/wissenschaft/publikationen.html



ISSN 1614-1199